



Monte Carlo microdosimetry of charged-particle microbeam irradiations

Eva Torfeh

► To cite this version:

Eva Torfeh. Monte Carlo microdosimetry of charged-particle microbeam irradiations. Astrophysics [astro-ph]. Université de Bordeaux, 2019. English. NNT : 2019BORD0159 . tel-02408981

HAL Id: tel-02408981

<https://theses.hal.science/tel-02408981>

Submitted on 13 Dec 2019

HAL is a multi-disciplinary open access archive for the deposit and dissemination of scientific research documents, whether they are published or not. The documents may come from teaching and research institutions in France or abroad, or from public or private research centers.

L'archive ouverte pluridisciplinaire **HAL**, est destinée au dépôt et à la diffusion de documents scientifiques de niveau recherche, publiés ou non, émanant des établissements d'enseignement et de recherche français ou étrangers, des laboratoires publics ou privés.

THÈSE PRÉSENTÉE
POUR OBTENIR LE GRADE DE
DOCTEUR DE
L'UNIVERSITÉ DE BORDEAUX

ÉCOLE DOCTORALE DES SCIENCES PHYSIQUES ET DE L'INGÉNIEUR

SPÉCIALITÉ : Astrophysique, plasmas, nucléaires

Par Eva TORFEH

**Monte Carlo microdosimetry of charged-
particle microbeam irradiations**

Sous la direction de : M. Philippe BARBERET

Soutenue le 01 octobre 2019

Membres du jury :

Mme GSCHWIND Régine, professeur, Université de Franche-Comté
Mme BORDAGE Marie-Claude, chargé de recherche, CNRS
M. FRANCIS Ziad, maître de conférences, Université Saint-Joseph de Beyrouth
M. INCERTI Sébastien, directeur de recherches, CNRS
M. KANTOR Guy, professeur, Université de Bordeaux

Présidente
Rapporteuse
Rapporteur
Examineur
Examineur

Acknowledgements

En premier lieu, je voudrai remercier Monsieur Philippe MORETTO et Monsieur Fabrice PIQUEMAL, directeurs du Centre d'Etudes Nucléaires de Bordeaux-Gradignan, pour m'avoir si bien accueillie au sein du laboratoire.

Je tiens à remercier Madame Marie-Claude BORDAGE et Monsieur Ziad FRANCIS pour m'avoir fait l'honneur d'être les rapporteurs de mon travail de thèse. Je voudrais remercier aussi les membres du jury, Madame Régine GSCHWIND, Monsieur Sébastien INCERTI et Monsieur Guy KANTOR pour avoir accepté d'examiner ce travail.

Mes sincères remerciements s'adressent à Philippe BARERET, mon directeur de thèse qui m'a encadré pendant ces 3 années. Je le remercie pour sa gentillesse, sa disponibilité, sa patience pendant des intenses et rationnelles discussions qui m'ont permises de réaliser ce travail dans de bonnes conditions. Pour tout cela et aussi pour son aide, sa confiance et son soutien moral, je la remercie vivement. Je tiens également à remercier beaucoup Hervé SEZNEC pour ses conseils, son soutien, pour son aide, autant au niveau scientifique qu'au niveau personnel et de supporter mon côté « fraileuse ». Je voudrais aussi remercier Guillaume DEVES pour ses conseils en statistique et tout son aide en microscopie, et je n'oublierai jamais tous les midis où on a recherché des sandwiches à Gradignan. Merci aussi à Laurent PLAWINSKI pour ses conseils, sa gentillesse et sa bonne humeur.

Merci aux autres membres du groupe iRIBio que j'ai eu la chance de rencontrer : Sébastien INCERTI, Claire MICHELET, Franck GOBET, Douatsu, Nathanael et Florent pour l'accueil et la gentillesse.

Je n'oublie pas de remercier mes collègues de bureau Giovanna et Marina pour les moments qu'on a passé ensemble accompagnées de fous rires et de blagues.

Je voudrais aussi remercier tous les doctorants et les post-doctorants du CENBG, et l'ensemble du personnel du laboratoire particulièrement Tina pour tous les bons moments passés en sa compagnie et surtout Nathalie pour ses explications concernant la bureaucratie française et celle du labo, sans toi je n'aurai pas échangé mon permis de conduit.

À mes amis internationaux préférés : Ana, Flo, Franky, Ricky, Juan, Hervé, Pilar, José, et Esther, je n'ai pas de mots pour exprimer à quel point vous m'avez fait passer des très bons moments. Je vous dis merci pour toutes les choses que nous avons partagées ensemble au labo et en dehors du labo, à Bordeaux et en dehors de Bordeaux.

Merci à Majida, Hala, Sanaa, Iman, Iza, Shames, Noor, Jany et à tous mes amis.

Un énorme merci à mon père Ibrahim, ma mère Fadia, mes frères Tarraf et Fadi et à ma tante Marie pour le soutien inconditionnel et pour l'amour.

Enfin, le plus grand merci est à Edy pour son soutien et pour supporter mes changements d'états tous les jours. Ce travail n'aurait jamais pu être mené à bien sans ton encouragement, ton écoute et ta compréhension.

Monte Carlo microdosimetry of charged-particle microbeam irradiations

Abstract

The interaction of charged-particles with matter leads to a localized energy deposits in sub-micrometric tracks. This unique property makes this type of ionizing radiation particularly interesting for deciphering the radiation-induced molecular mechanisms at the cell scale. Charged-particle microbeams (CPMs) provide the ability to target a given cell compartment at the micrometer scale with a controlled dose down to single particle. My work focused on irradiations carried out with the CPM at the AIFIRA facility in the CENBG (*Applications Interdisciplinaires des Faisceaux d'Ions en Région Aquitaine*). This microbeam delivers protons and α -particles and is dedicated to targeted irradiation *in vitro* (human cells) and *in vivo* (*C. elegans*).

In addition to their interest for experimental studies, the energy deposits and the interactions of charged-particles with matter can be modeled precisely along their trajectory using track structure codes based on Monte Carlo methods. These simulation tools allow a precise characterization of the micro-dosimetry of the irradiations from the detailed description of the physical interactions at the nanoscale to the prediction of the number of DNA damage, their complexity and their distribution in space.

During my thesis, I developed micro-dosimetric models based on the Geant4-DNA modeling toolkit in two cases. The first concerns the simulation of the energy distribution deposited in a cell nucleus and the calculation of the number of different types of DNA damage (single and double strand breaks) at the nanometric and micrometric scales, for different types and numbers of delivered particles. These simulations are compared with experimental measurements of the kinetics of GFP-labeled (Green Fluorescent Protein) DNA repair proteins in human cells. The second is the dosimetry of irradiation of a multicellular organism to study the genetic instability in a living organism during development (*C. elegans*). I simulated the distribution of the energy deposited in different compartments of a realistic 3D model of a *C. elegans* embryo following proton irradiations. Finally, and in parallel with these two studies, I developed a protocol to characterize the AIFIRA microbeam using fluorescent nuclear track detector (FNTD) for proton and α -particle irradiations. This type of detector makes it possible to visualize in 3D the incident particle tracks with a resolution of about 200 nm and to examine the quality of the cellular irradiations carried out by the CPM.

Keywords: Charged-particle microbeam, targeted irradiation, Monte Carlo, Geant4-DNA, microdosimetry, radiobiology.

Micro-dosimétrie d'irradiations par microfaisceau d'ions par méthodes Monte-Carlo

Résumé

L'interaction des particules chargées avec la matière conduit à un dépôt d'énergie très localisé dans des traces de dimensions sub-micrométriques. Cette propriété unique rend ce type de rayonnement ionisant particulièrement intéressant pour disséquer les mécanismes moléculaires radio-induits à l'échelle de la cellule. L'utilisation de microfaisceaux de particules chargées offre en outre la capacité d'irradier sélectivement à l'échelle du micromètre avec une dose contrôlée jusqu'à la particule unique. Mon travail a porté sur des irradiations réalisées avec le microfaisceau de particules chargées de la plateforme AIFIRA (Applications Interdisciplinaires des Faisceaux d'Ions en Région Aquitaine) du CENBG. Ce microfaisceau délivre des protons et particules α et est dédié aux irradiations ciblées *in vitro* (cellules humaines) et *in vivo* (*C. elegans*).

En complément de l'intérêt qu'elles présentent pour des études expérimentales, les dépôts d'énergie et les interactions des particules chargées avec la matière peuvent être modélisés précisément tout au long de leur trajectoire en utilisant des codes de structures de traces basés sur des méthodes Monte-Carlo. Ces outils de simulation permettent une caractérisation précise de la micro-dosimétrie des irradiations allant de la description détaillée des interactions physiques à l'échelle nanométrique jusqu'à la prédiction du nombre de dommages à l'ADN et leurs distributions dans l'espace.

Au cours de ma thèse, j'ai développée des modèles micro-dosimétriques basés sur l'outil de modélisation Geant4-DNA dans deux cas. Le premier concerne la simulation de la distribution d'énergie déposée dans un noyau cellulaire et le calcul du nombre des différents types de dommages ADN (simple et double brin) aux échelles nanométrique et micrométrique, pour différents types et nombres de particules délivrées. Ces résultats sont confrontés à la mesure expérimentale de la cinétique de protéines de réparation de l'ADN marquées par GFP (Green Fluorescent Protein) dans des cellules humaines. Le second concerne la dosimétrie de l'irradiation d'un organisme multicellulaire dans le cadre d'études de l'instabilité génétique dans un organisme vivant au cours du développement (*C. elegans*). J'ai simulé la distribution de l'énergie déposée dans différents compartiments d'un modèle réaliste en 3D d'un embryon de *C. elegans* suite à des irradiations par protons. Enfin, et en parallèle de ces deux études, j'ai développé un protocole pour caractériser le microfaisceau d'AIFIRA à l'aide de détecteurs de traces fluorescent (FNTD) pour des irradiations par protons et par particules α . Ce type de détecteur permet en effet de visualiser les trajectoires des particules incidentes avec une résolution de l'ordre de 200 nm et d'examiner la qualité des irradiations cellulaires réalisées par le microfaisceau.

Mots-clés : Microfaisceau d'ions, micro-irradiation ciblée, Monte-Carlo, Geant4-DNA, microdosimetrie, radiobiologie.

Table of contents

Résumé substantial	13
Acronyms/Abbreviations	19
Introduction	21
I. A few definitions to characterize IR interactions with matter.....	23
Energy deposit (ED)	
Linear Energy Transfer (LET)	
Absorbed dose	
Specific energy	
II. Charged-particles for Radiobiological study.....	25
III. Charged-particle microbeams.....	26
Micro-irradiation at the cellular scale	
From cellular to Multicellular	
IV. Charged-particle Microbeam at the AIFIRA facility.....	29
The microbeam characteristics	
Microscopy end-station	
Studies used the microbeam at the AIFIRA facility	
Experimental characterization of the AIFIRA CPM using a track detector	
Cellular micro-irradiation: Kinetic study of DNA repair proteins	
Multicellular micro-irradiation: Radio-induced effect <i>in vivo</i>	
V. Microdosimetry.....	33
Track detectors	
Monte Carlo simulation codes : Geant4/Geant4-DNA	
Introduction references.....	39
 Part I: Experimental characterization of the charged-particles microbeam using FNTDs	49
Introduction.....	51
Methods.....	53
I. Fluorescent Nuclear Track Detectors (FNTDs).....	53
II. CPM irradiation of FNTDs.....	54
III. FNTDs read-out using confocal laser scanning microscopy.....	55
IV. Confocal Images processing using ImageJ.....	55
V. SRIM simulations.....	56
Results.....	57
I. Single proton and α -particle tracks.....	57

I.1. Single particle 3D visualization.....	57
I.2. Single particle track length measurements.....	58
I.3. Single track spot sizes as function of particle LETs.....	61
II. FNTD intensity response as function of delivered dose.....	61
III. Beam size measurement.....	64
Discussion.....	65
References.....	67

Part II: Kinetic study of detection and repair of DNA damage proteins after irradiations at cellular scale.....71

Introduction.....	73
Methods.....	76
I. Experimental cellular micro-irradiation using CPM.....	76
I.1. Cell lines expressing GFP-XRCC1 and GFP-RNF8 proteins.....	76
I.2. Cells micro-irradiation and time lapse imaging.....	77
I.3. Fluorescent images treatment and data fitting models.....	78
II. Microdosimetry of the cellular ion microbeam irradiations.....	79
II.1. Simulation of track structures and energy distributions.....	79
II.2. Clustering of DNA damage.....	80
II.2.1. Calculation of the induction of Strand breaks.....	80
II.2.2. Clustering of DNA damage.....	81
II.3. DSBs clustering at the micron scale.....	82
Results.....	84
I. Experimental results.....	84
I.1. Recruitment kinetics of GFP-XRCC1 protein to DNA damage sites after α -particle and proton irradiations.....	84
I.2. Recruitment kinetics of GFP-RNF8 protein at DNA damage sites after CPM irradiations...	87
II. Modelling results using Geant4-DNA.....	89
II.1. Track structure and energy distributions of α -particles and protons after CPM irradiations.....	89
II.2. DNA damages prediction and distribution based on clustering calculation at the nanometric scale.....	91
II.3. DSBs clustering at the micron scale	92
Discussion.....	94
References.....	98

Part III: Multicellular micro-irradiation: Biological radio-induced effects by ionizing radiations *in vivo*..... 103

Introduction.....	105
Methods.....	110
I. Micro-irradiation of a multicellular living organism: <i>C. elegans</i>	110
I.1. <i>C. elegans</i> transgenic strains.....	110
I.2. Preparation of culture wells for irradiation	111
I.3. Irradiation and video microscopy	112
II. Micro-dosimetry of <i>C.elegans</i> embryo ion microbeam irradiations.....	113
II.1. Modeling of the <i>C. elegans</i> embryo with a realistic phantom.....	114
II.1.1. Preparation of embryo samples for confocal microscopy.....	115
II.1.2. Confocal fluorescence microscopy.....	116
II.1.3. Creation of the three-dimensional phantom using ImageJ.....	117
II.1.4. Implantation of the phantom in Geant4-DNA.....	118
II.2. Modeling 40 embryo cells with different chromatin stages.....	120
III. Micro-dosimetry of <i>C.elegans</i> L1 larvae	121
III.1. Modeling <i>C. elegans</i> L1 larva with simple geometric shapes.....	121
Results.....	123
I. Experimental results.....	123
I.1. Visualization of the consequences of CPM irradiations.....	123
II. Modelling results.....	125
II.1. <i>C. elegans</i> embryo modeling with voxelized realistic phantom.....	125
II.2. Effect of chromatin condensation on energy deposits in 40 embryo cells.....	126
II.3. <i>C. elegans</i> L1 larva modeling and irradiation.....	129
Discussion.....	132
References.....	134
Publication	139
Conclusions and perspectives.....	153

Résumé substantiel

Les études des interactions entre les rayonnements ionisants (RI) et les tissus vivants jouent un rôle important dans de nombreux domaines, tels que les risques de santé associés à l'exposition aux RIs de sources naturelles (rayons cosmiques, radioactivité naturelle...), dans les environnements de travail (production d'énergie, usages industriels...) ou des applications médicales (médecine nucléaire et radiothérapie). L'interaction des RIs avec la matière est caractérisée par un transfert d'énergie du rayonnement incident aux atomes/molécules et à un ou plusieurs électrons présents dans le milieu exposé. Ce transfert d'énergie résulte d'une suite d'événements physiques dépendant du type de rayonnement.

Comparées à d'autres types de RIs, les particules chargées sont caractérisées comme des RIs directs qui transfèrent leur énergie directement à la matière contrairement aux particules neutres (rayonnements électromagnétiques et neutrons) qui transfèrent leur énergie indirectement. Les particules chargées ont un transfert d'énergie linéique (TEL) plus élevé, induisant des dépôts d'énergie localisés le long des traces de particules. Ils interagissent principalement avec les électrons et provoquent l'ionisation et/ou l'excitation du nuage électronique des atomes. Ces particules chargées peuvent être produites naturellement à partir de la radioactivité (particules α) et du rayonnement cosmique (principalement des protons et des noyaux d'hélium) et artificiellement à l'aide des accélérateurs. Les particules chargées produites par les accélérateurs sont utilisées pour des applications biomédicales (protonthérapie et hadronthérapie) et pour la recherche (études radiobiologiques, physique des particules et nucléaire, cosmologie et astrophysique...).

Les travaux présentés ici sont focalisés sur les micro-irradiations d'échantillons biologiques avec le microfaisceau de particules chargées sur la plateforme AIFIRA (Applications Interdisciplinaires de Faisceaux d'Ions en Région Aquitaine) au CENBG (Centre d'Études Nucléaires de Bordeaux-Gradignan) et plus spécifiquement sur les questions de microdosimétrie liées à cette approche expérimentale. Les particules chargées présentes sur AIFIRA sont des protons ($\text{TEL} = 12 \text{ keV} \cdot \mu\text{m}^{-1}$) et des particules α ($\text{TEL} = 148 \text{ keV} \cdot \mu\text{m}^{-1}$) ayant une énergie de l'ordre du MeV et ont des TELs élevés induisant des lésions moléculaires très complexes lors du dépôt de leur énergie dans la matière vivante. Du point de vue expérimental, les particules chargées présentent des caractéristiques uniques pour générer des lésions moléculaires localisées dans les cellules vivantes et pour étudier les conséquences moléculaires et biologiques des lésions clustérisées. Lorsqu'elles se propagent dans la matière,

elles déposent leur énergie le long des traces presque linéaires qui peuvent être modélisées en détails par des codes de structure de trace basés sur les calculs Monte-Carlo. Ceci constitue l'un des principaux atouts de leur utilisation par rapport aux techniques de micro-irradiation plus courantes basées sur les lasers ou les microspots UV.

Avant ma thèse, le groupe iRiBio du CENBG avait développé des techniques et des méthodologies expérimentales en utilisant le microfaisceau sur AIFIRA pour micro-irradier des cellules biologiques, d'une façon reproductible, avec un nombre précis de particules, focalisées à l'échelle micrométriques et dans des compartiments cellulaires spécifiques. Ces développements ont commencé à être appliqués ces dernières années à la mesure expérimentale des effets biologiques d'organismes de l'échelle cellulaire jusqu'à l'échelle multicellulaire.

En effectuant des irradiations ciblées avec le microfaisceau, l'énergie déposée est localisée dans une structure cellulaire/sub-cellulaire et les réponses aux RIs dépendent de sa distribution stochastique, qui à son tour dépend du type et de l'énergie des particules et de la taille de la cible (différents compartiments de l'échantillon irradié). Pour les échantillons biologiques, la cible principale est l'ADN et sa taille est inférieure à l'extension latérale du nuage d'ionisation entourant la majorité des particules chargées utilisées dans les expériences radiobiologies. En conséquence, la structure de trace, basée sur le concept de la microdosimétrie, est considérée très essentielle pour comprendre et expliquer des résultats qui, apparemment, n'ont pas d'explication appropriée, en considérant uniquement les grandeurs moyennes comme la dose absorbée.

Dans nos études par microfaisceau de particules chargées, les grandeurs dosimétriques d'intérêt ne sont pas mesurables directement lors de la micro-irradiation. Néanmoins, les caractéristiques physiques de la structure de trace des ions peuvent être mesurées avant ou après l'irradiation à l'aide de détecteurs de traces et les grandeurs physiques peuvent être simulées à l'aide de codes de Monte-Carlo.

Mon travail de thèse visait à développer des modèles microdosimétriques permettant de mesurer ou de simuler des grandeurs physiques qui ne peuvent pas être mesurées directement lors des micro-irradiations effectuées sur AIFIRA. L'idée était de corréler ces grandeurs, principalement l'énergie déposée, l'énergie spécifique et le nombre des dommages de l'ADN aux effets observés lorsque les cellules étaient irradiées avec le microfaisceau de particules chargées. Ceci a été réalisé en mesurant les caractéristiques physiques du microfaisceau de particules chargées en utilisant de nouveaux détecteurs de trace à haute résolution et en simulant les interactions des protons et des particules α focalisés à l'échelle micrométriques

allant des premières énergies déposées jusqu'à la prédiction des dommages à l'ADN en utilisant le code de structure de trace Geant4 -DNA.

La première partie de ce travail consistait à développer une méthodologie permettant d'utiliser le détecteur de trace FNTD (*Fluorescent Nuclear Track Detectors*) pour le contrôle qualité du microfaisceau sur la plateforme AIFIRA, notamment pour visualiser expérimentalement ses différentes caractéristiques. Les FNTDs ont été micro-irradiés avec des protons et des particules α suivant des motifs de particules uniques et d'un nombre croissant de particules. Les traces uniques de protons et de particules α de l'ordre du MeV ont été détectées sans ambiguïté et la taille de la tache fluorescente correspondante aux impacts des particules est inférieure à 1 micromètre. Lors de l'irradiation avec plusieurs traces de particules dans un point de faisceau micrométrique, l'intensité de la fluorescence augmente linéairement avec la dose avant de saturer au-dessus d'environ 20 particules/point. Grâce à cette intensité de fluorescence, la taille du microfaisceau a été mesurée donnant des valeurs comparables avec des valeurs estimées en utilisant les simulation Monte-Carlo. Par rapport au détecteur de trace nucléaire CR39 utilisé jusqu'à présent, les FNTDs ne nécessitent aucun traitement chimique pour la lecture, cette lecture se fait en utilisant simplement la microscopie confocale. Ces FNTDs offrent des fonctionnalités intéressantes telles qu'une résolution spatiale élevée, une plage dynamique étendue de mesures d'énergie déposée et des informations de trace tridimensionnelles. Pour cela, les FNTD seront utilisées en routine dans l'avenir pour assurer le contrôle qualité du microfaisceau pour les expériences d'irradiation cellulaire avec des particules uniques.

Ensuite, le microfaisceau AIFIRA a été utilisé pour étudier les mécanismes de réparation de l'ADN dans des cellules micro-irradiées avec un nombre croissant de protons ou de particules α . La cinétique in vitro de la réponse de deux protéines marquées en GFP (*Green Fluorescent Protein*) impliquée dans la reconnaissance, la signalisation et la réparation de dommages à l'ADN induit par un rayonnement a été étudiée. Les deux protéines sont GFP-XRCC1 (cassures simple brin et voies BER / NER) et GFP-RNF8 (cassures doubles brins). La cinétique d'accumulation de ces protéines sur les sites endommagés a été mesurée au cours d'un travail précédant ma thèse grâce à la vidéo microscopie. La réponse précoce de ces protéines (secondes à quelques minutes) fournit des informations intéressantes sur la relation entre les lésions physiques initiales et les voies de réparation de l'ADN.

J'ai contribué aux calculs microdosimétriques des énergies déposées et des dommages directs induits à l'ADN. La structure de trace d'un proton et d'une particule α ont été reconstruites à partir de données simulées en utilisant Geant4-DNA afin de comparer la distribution de

l'énergie déposée par les 2 types de particules. Pour comparer les réponses temporelles de recrutement des protéines après irradiation avec les 2 types de particules des noyaux cellulaires, j'ai simulé la distribution de l'énergie dans un cube d'eau liquide homogène de 6 μm d'épaisseur correspondant à l'épaisseur moyenne d'une cellule humaine. Ensuite pour prédire le nombre de dommages à l'ADN (cassures simple brin (SSB), cassures double brins (DSB) et cassures de brin complexe (CSB)), j'ai clustérisé ces dépôts d'énergie en se basant sur l'exemple « *Clustering* » de Geant4-DNA. La clusterisation des dommages a également été effectuée à l'échelle de la sous-structure de la chromatine (échelle du micromètre) afin d'étudier leur distribution spatiale et de déterminer leur complexité.

Le nombre de particules délivrées, l'énergie déposée et le nombre prédit de dommages à l'ADN ont ensuite été corrélés aux profils cinétiques de ces protéines. Les résultats indiquent une cohérence entre la fonction de la protéine, la distribution de l'énergie déposée et sa clusterisation en différents types de dommages à l'ADN. Cependant, l'interprétation complète des résultats biologiques nécessitera de surmonter quelques limitations liées aux calculs microdosimétriques. C'est notamment le cas de la clusterisation des lésions de l'ADN. La clusterisation à l'échelle nanométrique n'a été calculé que pour les effets directs dans un cube d'eau homogène. Cela pourrait être amélioré en prenant en compte les géométries réalistes de l'ADN dans les cellules humaines afin de permettre le calcul des dommages à l'ADN dus à des effets directs et indirects. Un exemple de Geant4-DNA permettant ces calculs devrait être disponible prochainement. Du point de vue expérimental, le lien entre la cinétique des protéines et le nombre de lésions induites par l'ADN pourrait également être décrit par une modélisation théorique du comportement des protéines après des micro-irradiations à particules chargées et par leur diffusion vers les sites des dommages. Ces sites endommagés peuvent être modélisés comme des sites de piégeage de protéines avec une probabilité de fixation en fonction du nombre de lésions à l'ADN évaluées par des simulations de Monte-Carlo.

Enfin, une méthodologie permettant de micro-irradier de manière reproductible un organisme vivant, *C. elegans*, à un stade spécifique et d'observer en temps réel les effets radio-induits sur AIFIRA a été validée avant le début du présent travail. Ce simple stade du cycle de vie de *C. elegans* avec 2 cellules permettait de suivre plus facilement la cellule irradiée pendant les premières divisions cellulaires après l'irradiation. Cette approche ouvre des perspectives d'irradiation sélective et ciblée de cellules dans un organisme en développement avec des doses spécifique (jusqu'à une particule/cellule). Néanmoins, l'étude de la relation dose-effet avec une telle irradiation pose la question de la dose réellement délivrée aux différents

compartiments de cet organisme. En effet, ce type d'échantillon a une géométrie sensiblement différente de celle des cellules adhérentes et son développement rapide implique une variation de la géométrie des cellules et de la condensation de la chromatine à des échelles de temps comparables au temps requis pour l'irradiation. Pour cela, il était nécessaire de calculer l'énergie déposée dans des volumes 3D réalistes de l'embryon de *C. elegans* au stade 2 cellules. Les simulations microdosimétriques développées lors de ma thèse ont été effectuées dans des fantômes 3D réalistes des embryons stade 2 cellules en se basant sur l'imagerie confocale. Ces simulations ont permis de calculer l'énergie déposée dans 3 compartiments de l'embryon (la chromatine, le volumes nucléaire et la totalité de l'embryon) et de quantifier la fraction d'énergie transmise à la chromatine compte tenu de sa condensation suivant les différentes phases de la division cellulaire (prophase et métaphase). Ces résultats ont été publiés récemment dans "Torfeh, E. *et al.* 2019". Dans l'avenir, cette méthodologie pourra être appliquée à d'autres stades de développement et à des faibles doses, ouvrant ainsi un cadre complet de radiobiologie comprenant un ciblage précis et reproductible du rayonnement, des méthodes de microdosimétrie avancées à base de Monte-Carlo en open source, ainsi qu'un modèle approprié pour étudier la réponse biologique précoces jusqu'aux effets transgénérationnels.

Acronyms/Abbreviations

BNCD	Boron-doped Nano-Crystalline Diamond
cDSBS	clustered DSB
<i>C. elegans</i>	<i>Caenorhabditis elegans</i>
CLSM	Confocal Laser Scanning Microscopy
CPM	Charged-Particle Microbeam
CSB	Complex Strand Breaks
DBSCAN	Density Base Spatial Clustering of Applications with Noise
DSB	Double Strand Break
ED	Energy deposit
FNTD	Fluorescent Nuclear Track Detector
GFP	Green Fluorescent Protein
HR	Homologous Recombination
HyD	Hybrid Detector
iDSB	isolated DSB
IR	Ionizing Radiations
IRIF	Ionizing Radiation-Induced Foci
LET	Linear Energy Transfer
LMI	micro-irradiation
NHEJ	Non-Homologous End Joining
PNTD	Plastic Nuclear Track Detector
PMT	PhotoMultiplier Tube
RBE	Relative biological effectiveness
scCVD	single-crystal Chemical-Vapor-Deposited
SRIM	Stopping and Range of Ions in Matter
SSB	Single Strand Break

Introduction

The knowledge of the interactions between ionizing radiations (IR) and living tissues has an important role in many fields, such as health risks associated to the exposure to IR from natural sources (cosmic rays, natural radioactivity ...), working environment (energy production, industrial uses...) or medical applications (nuclear medicine and radiation therapies). IR can be defined as a radiation having enough energy (above 13.6 eV) to snatch an electron (named secondary electron) from an atom or a molecule, thereby ionizing it. The interaction of IRs with matter is characterized by a transfer of energy from the incident radiation to the atoms/molecules and to one or several electrons present in the exposed medium. This energy transfer is the result of a sequence of physical events depending on the type of radiation¹.

Compared with other types of IR, charged-particles are characterized as direct IRs which transfer their energy directly to matter contrary to neutral particles (electromagnetic radiations and neutrons) that cause indirect ionizations. Charged-particles have the higher Linear Energy Transfer (LET), inducing localized energy deposits along the particle tracks. Charged-particles interact mainly with electrons, via Coulomb diffusion and cause the ionization and/or the excitation of the electronic cloud of atoms. Charged-particles can be produced naturally from radioactivity (α -particles) and cosmic radiation (mainly protons and helium nuclei), and artificially using accelerators. Charged-particles produced by accelerators are used for biomedical applications (proton therapy and hadrons therapy) and research applications (radiobiological study, particle and nuclear physics, cosmology and astrophysics...). The work presented here will focus on charged-particle irradiations.

I. A few definitions to characterize IR interactions with matter

In the following and before detailing charged-particle tools used for radiobiology studies, it is necessary to define useful physical quantities to characterize IR interactions that will be used throughout this manuscript.

Energy deposit (ED)

IRs interact with matter at points in space where a discrete amount of energy is transferred to the medium. This will be referred to as energy deposit (ED) and it is typically measured in electron volt (eV).

Linear Energy Transfer (LET)

The energy loss of charged-particles or photons in matter is characterized by the Linear Energy Transfer (LET), defined by the International Commission on Radiological Protection (ICRP) ² as the ratio of the mean energy transferred locally in the medium, dE , (by charged-particle or photons), per unit length dl . Generally given in $\text{keV} \cdot \mu\text{m}^{-1}$, the LET depends on the target material, the particle type and the incident energy. Based on the LET values, IRs can be separated into sparsely IRs with low LET (X-Rays, γ -Rays and electrons) and densely IRs with high LET (ions and neutrons radiations). A LET value of $10 \text{ keV} \cdot \mu\text{m}^{-1}$ is defined as a threshold between low and high LET radiations²⁻⁴.

A good knowledge of this LET allows to estimate the energy loss along the track of an ionizing particle. Charged-particles with lower energy have higher LET values that fluctuate along the particle track (Part I, Fig.10). For example, the energy lost by protons and heavier charged-particles during the interaction with matter rapidly increases after a short distance, generating the so-called Bragg peak, and particles are then stopped. This is not the case for photons ²⁻⁵.

Absorbed dose

Biological effects are related to the amount of energy that is deposited by the radiation per unit of mass of tissue. The amount or the quantity of energy transferred to the material during exposure to IRs is characterized by the absorbed dose. The absorbed dose at a point is the ratio of the averaged energy absorbed (in joules) in an elementary volume centered at that point to the mass of that elementary volume (in kilograms). It is expressed in Gray (Gy), and 1 Gy corresponds to an ED of 1 joule per kilogram of irradiated matter ($1 \text{ Gy} = 1 \text{ J} \cdot \text{kg}^{-1}$)⁶.

Specific energy

Absorbed dose, especially used when macroscopic volumes (such as organs or tumors) are irradiated in a homogeneous manner, cannot represent the stochastic discrete nature of energy transfers at the micro or nanometer scale⁷. This becomes a problem particularly when the size of the target volumes is of the order of cell nuclei or DNA molecule. This has prompted the introduction of microdosimetric formalism. When single cells are irradiated, it is more appropriate to use the microdosimetric quantity “specific energy” instead of the macroscopic “absorbed dose”⁸. The specific energy is defined as the direct ratio of ε divided by m . ε called imparted energy being the sum of the energy transferred to the medium via all the interactions with atoms of the medium of the primary particle and its secondaries. m being the mass of the

microscopic volume of interest^{9, 10}. ICRU has reported the concept of specific energy as the ratio of the energy imparted to the mass of the volume of interest³.

II. Charged-particles for Radiobiological study

Apart from the studies aiming at understanding their biological effects related to radio activity or medical applications (protons, α -particles or carbon ions), charged-particles have unique features for micro-irradiation experiments. They deposit their energy along tiny tracks and their interaction with matter can be simulated in detail.

Localized DNA lesions in a given cell compartment can be triggered using various micro-irradiation techniques. UV micro-irradiation has been used to target sub-nuclear areas and to visualize the recruitment of proteins involved in DNA repair, DNA damage response, chromatin remodeling and histone modifications without any specialized equipment^{11,12}. Laser based micro-irradiation is the most commonly used method as it presents the great advantage of being based on the same microscope to perform irradiation and observation of the cellular response^{13–17}. It does not require the use of complex instrumentation and can be relatively easily installed in a biology lab. One of the limitation of this approach is the wide variety of different lesions (such as DNA single strand breaks and double strand breaks) that can be induced depending on the wavelength, energy and exposure time¹⁸. Moreover, the observed effect cannot be easily related to a radiation dose. Charged-particles are more representative of the IRs than laser beams and with direct access to charged particle beams it provide more well-behaved energy deposition equally distributed over all molecular species^{19,20}.

When absorbed by living cells, IR can interact directly with the DNA structure and produce physical and molecular changes known as “direct effects”. It can also interact indirectly through water radiolysis and generate reactive chemical species (free radicals) that may damage the DNA structure by chemical reactions. These phenomena are called “indirect effects”².

The study of charged-particles effects on living organisms requires tools, methods and models passing from physics to biology, to perform the exposures of biological samples to IRs and to visualize and follow in real time the consequences.

There are various irradiation modes to expose biological cells to charged-particles. The simplest way, in terms of instrumentation and implementation, is the use of radioactive

sources allowing a homogeneous irradiation of a large number of cells. However, this irradiation mode is limited to α -particles.

Ion beam accelerators allow to deliver parallel beams with various types of ions of different LETs. Ion beams present the advantage to irradiate thousands of cells almost instantly. This irradiation mode was used in a large number of studies to measure the effects of global irradiation on the cellular survival of a cell population to determine the relative biological effectiveness of irradiations^{21–27}.

Using these two classical irradiation modes (broad beam or radioactive sources), the number of delivered particles cannot be controlled at the single cell scale. For a cell population irradiated with low dose, the number of impacts per cell follows a statistical distribution (normal distribution at high doses and Poisson distribution at low doses)²⁸. These two irradiation modes reach their limits for radiobiological studies at the cellular and subcellular scale. To overcome these limits and to observe the charged-particle effects at the micrometric scale, Charged-Particle Microbeams (CPMs) were created for the targeted irradiation of single cells with a controlled dose.

III. Charged-particle microbeams

Micro-irradiation at the cellular scale

At the end of 1990s, CPMs were developed specifically to investigate the effects of low doses of IRs on living samples^{29, 30}. Thanks to the technological innovations and developments in particle delivery, focusing and detection, image processing and recognition, computer control, and on the basis of the experience acquired along the years, the features of microbeam facilities have been changing over the years with respect to the first facilities born in the nineties^{31, 32}.

CPM systems are designed to deliver a controlled number of charged-particles (one or many) with a positioning accuracy of a few micrometers in targeted biological cells. This allows the study of biological responses to charged-particles at both single cell and subcellular levels (nucleus or cytoplasm). In brief, CPMs stand out for 3 main characteristics: (i) the micrometer spatial resolution (ii) the time resolution, i.e. the precise knowledge of the irradiation time and (iii) the dose resolution controlled by active detectors allowing to deliver a precise number of particles at the cellular scale.

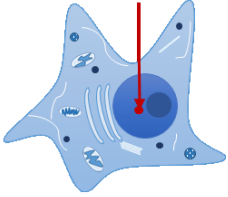
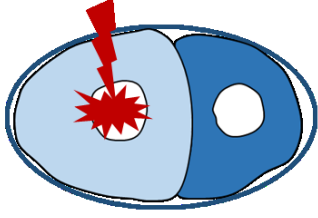
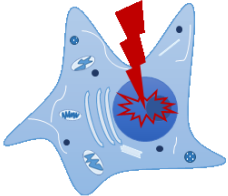
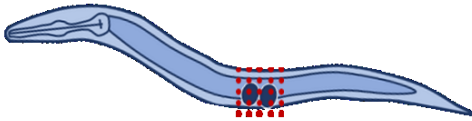
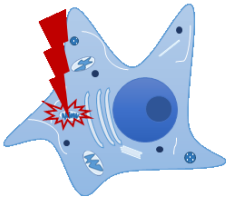
Cellular Irradiations (<i>in vitro</i>)		Multicellular Irradiations (<i>in vivo</i>)	
Single particle		Selective	
Nuclear			
Sub-cellular		Regular pattern	

Fig. 1. Characteristics of microbeam features for the irradiation of biological samples. Microbeam allows an absolute control of the number of delivered particles in a cell. In addition, thanks to the focalization and scanning system, microbeam allows to irradiate selectively a given sub-cellular compartment or a specific cell or area within a cellular organism with one spot or regular pattern.

To date, a few microbeams are routinely used for targeted cellular irradiation. Reviews of the various applications of microbeams for radiobiological applications (Fig. 1) are summarized in^{18,33}.

The main CPM characteristic is the ability to deliver single ions to individual cell. This unique feature has been used to measure the effect of a single particle track on oncogenic transformation³⁴, cellular toxicity, nuclear DNA mutagenesis³⁵, micro- nuclei formation and genomic instability³⁶. In addition, CPM micrometer targeting accuracy and exact control of the irradiation timing provide the opportunity to study the radiation sensitivity of sub-cellular compartments such as cytoplasm³⁷, mitochondria³⁸, nucleus and even various parts of the nuclear chromatin³⁹.

In the 2010's, several CPMs have been coupled to immunostaining, GFP-tagging (Green Fluorescent Protein), high resolution fluorescence microscopy and time-lapse imaging to study the DNA signaling and repair mechanisms^{19,40}. As an example, Hable *et al.* used the microbeam facility SNAKE⁴¹ to shown that the recruitment of the MDC1 and RAD52 proteins depend on the complexity of the damage generated, i.e. the LET, which is not the

case for 53BP1⁴². At the IMP heavy ion microbeam facility, the repair dynamic of XRCC1 protein in the early stage of DNA damage after irradiation with single high energy nickel ion have been studied using online live cell imaging system⁴³. The PTB microbeam also investigated 53BP1 and MDC1 dynamics after irradiations at low and high LETs⁴⁴.

CPM are also used to deliver the particles on geometrical patterns, providing a way to investigate i.e. the diffusion behavior of DNA double strand breaks. Irradiation according to geometric patterns have been used to analyze the effects of sequential micro-irradiations and to highlight a competition effect for the recruitment of the 53BP1 protein⁴⁵. Girst *et al.* have taken advantage of the ability of ion microbeams to perform micro-irradiations in a regular pattern to follow MDC1 foci movement. Mobility following a phenomenon of sub-diffusion has been highlighted by this work⁴⁶.

From cellular to Multicellular

Data from *in cellulo* experiments on monolayers are very useful to understand fundamental radiation-induced biological mechanisms but are difficult to extrapolate and understand the *in vivo* response. Three-dimensional tissue models can be used in combination with microbeam irradiation to overcome these limitations. Several microbeam studies have been performed with reconstructed human epidermis^{47–50}. Organotypic slice culture methods have been also recently used as an *ex vivo* model for radiation biology applications as they mimic the tissues' natural three-dimensional cyto-architecture and they can be used to study the radiation effect on several kinds of human tissues⁵¹. As part of the study of new modes of cancer treatment by proton therapy, Schmid *et al.* sought to compare the EBR, on a model of reconstructed human skin, with two modes of microbeam irradiation of 20 MeV protons: a continuous mode and a pulsed mode (1 ns per pulse). The irradiation took place at SNAKE in Munich. EBR was evaluated from the formation of radio-induced micronuclei. No significant difference could be demonstrated between the two irradiation modes⁵².

CPM have been extended to irradiate small multicellular models compatible with charged-particle irradiations. Fukamoto *et al.* have developed a method to target Silkworm larvae (*Bombyx mori*) by a heavy ion microbeam for microsurgical studies. In particular, they studied the suppression of an abnormal cell multiplication phenotype after irradiation with 220 MeV carbon ions⁵³. Zebrafish *Danio rerio* embryos have been used to investigate the effects of low doses of IR^{54, 55}. There are several studies that use the combination of CPMs and the *Caenorhabditis elegans* (*C. elegans*) which made it the most widely used multicellular organism for ion microbeam irradiation^{56–58}. Buonanno *et al.* have demonstrated

the formation of the Rad51 foci in *C. elegans* worms, a protein involved in the repair of double-stranded DNA cases by homologous recombination, after 4.5 MeV proton microbeam irradiation⁵⁹. More recently, Suzuki *et al.* demonstrate that the responsible mechanisms for reducing the nematode mobility after whole-body irradiation is the body wall muscle cells rather than the central nervous system by irradiating independently 3 regions of adult nematodes (head region, mid region around the intestine and uterus, and tail region) with 18.3 MeV/u carbon ions at TIARA microbeam facility in Japan⁶⁰.

IV. Charged-particle Microbeam at the AIFIRA facility

Since the early 2000s, a microbeam system for the targeted micro-irradiation of living biological samples have been developed at CENBG (*Centre d'Études Nucléaires de Bordeaux-Gradignan*). This tool was initially developed by Barberet *et al.*⁶¹. A new version has been commissioned in 2012 on a dedicated beamline at the AIFIRA facility.

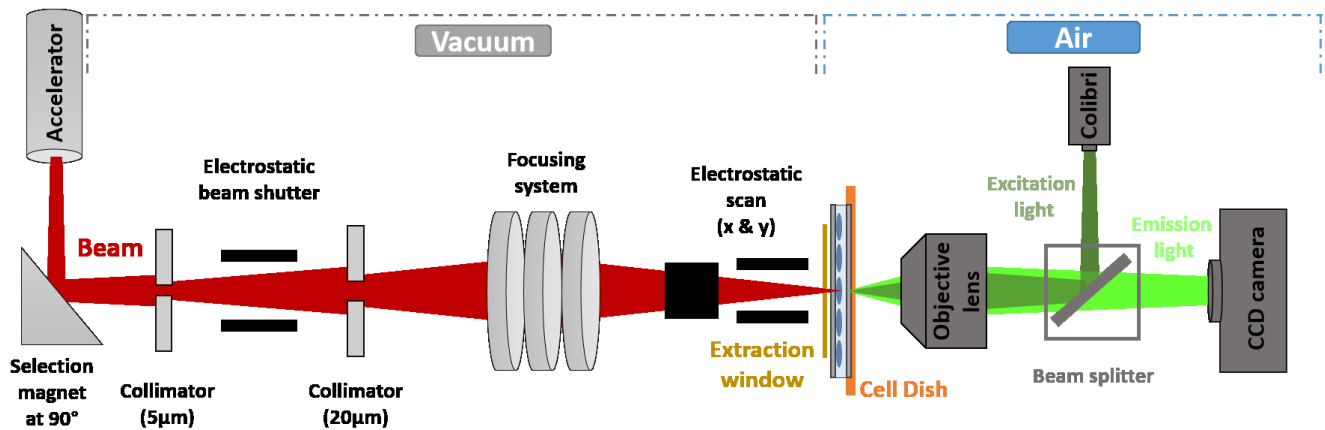


Fig. 2. Scheme of the micro-irradiation line set-up and microscopic system at AIFIRA. Charged-particles beam (in red) is collimated in two stages and then focused in a micrometric spot using triplet of magnetic lenses under vacuum. The beam is extracted to air through a 150 nm thick Si_3N_4 window (in yellow). The cells are kept in their culture medium and placed vertically in front of the extraction window. Electrostatic scanning plates, placed just before the extraction window, allow to position the beam on the target. A fluorescence microscope (*Zeiss AxioObserver Z1*) equipped with a CCD camera is placed at the end of the beam line to visualize the sample, to locate and target the region of interest, and perform online time-lapse imaging.

The microbeam characteristics

The microbeam line (Fig. 2), described in Bourret *et al.*, has been designed to study the biological responses to MeV protons and α -particles at cellular and subcellular scales (nucleus

and cytoplasm) for single and multiple cells irradiations⁴⁰. The beam is focused to a 1.5 μm beam spot (full width at half maximum FWHM). The beam is positioned by electrostatic means allowing very fast beam motions from one target to the other (μs time scale). This microbeam setup allows the exposure of cells to LET values of 12 keV/ μm (protons) and 148 keV/ μm (α -particles), leading to a maximum range in liquid water of 148 μm and 18 μm , respectively. The delivered specific energy can be either controlled by counting the particles with a detector that replaces the Si_3N_4 window or by adjusting the beam opening time. In the latter case, the mean number of particles (N) hitting cells is linearly related to the opening time and the relative statistical fluctuation in the number of traversals delivered decreases as N increases ($\frac{\Delta N}{N} = \frac{1}{\sqrt{N}}$).

For the precise counting of α -particles, each particle is detected upstream the sample with a BNCD (Boron-doped Nano-Crystalline Diamond) from which secondary electrons are collected using a channeltron electron multiplier⁶². In the case of protons, the secondary electrons production yield is too low and Barberet *et al.* designed a self-supported thin single-crystal chemical-vapor-deposited (scCVD) diamond membrane detector⁶³. This detector is approximately 2-3 μm in thickness and is usable as a vacuum window. It has a counting efficiency close to 100% for 3 MeV protons⁶³.

Microscopy end-station

The irradiation end-station is constituted of a fluorescence microscopy system based on dedicated sample holder and an inverted fluorescence microscope (Zeiss AxioObserver™ Z1), positioned horizontally at the end of the beam line. A fully motorized microscope was chosen to automate the irradiation and time-lapse imaging processes. In a typical experiment, several fields of view (containing about 10 to 20 cells) can be positioned in front of the beam, irradiated and imaged at regular time intervals during several minutes.

The imaging capabilities have been completed recently with a commercially available laser diode (Roper Scientific, iLas2™) coupled to a galvo-scanned mirror have been installed on the microscope. This set-up allows performing fluorescence recovery after photobleaching (FRAP) measurements in combination with charged-particle irradiations (Fig. 2).

Studies achieved using the microbeam at the AIFIRA facility

To validate the cellular micro-irradiation and the online monitoring system at the AIFIRA microbeam, Bourret *et al.*, showed the first measurements of the re-localization of the GFP-

XRCC1 protein at the damage sites in transfected Hela cells using online time-lapse imaging in the first minutes after irradiation⁴⁰. More recently, to investigate the spatio-temporal properties of the DNA damage response to single charged-particle of GFP-RNF8 transfected cells, the BNCD thin membrane was developed to allow reliable single α -particle detection and single cell irradiation with negligible beam scattering. Post-irradiation analyses showed that GFP-RNF8 accumulates continuously at single α -particle track during the first 30 minutes after irradiation⁶².

Another recent study that used the AIFIRA microbeam aimed to study the effects of charged-particles on mitochondrial membrane. Single and clusters of mitochondria were irradiated with 3 MeV protons at the AIFIRA microbeam facility and with 55 MeV carbon ions at the SNAKE facility in Munich. They showed for the first time that highly localized targeted mitochondrial irradiation using charged-particles induces mitochondrial membrane potential loss³⁸.

In 2017, Barberet *et al.* developed and validated an ultra-thin diamond proton detector at the AIFIRA microbeam facility compatible with micro-irradiation and online fluorescence time-lapse imaging. The detector is made of a thin scCVD diamond membrane⁶³.

In addition to the studies already mentioned, others coupling the AIFIRA microbeam cellular irradiations to physical and biological samples have been carried out and will be detailed in this thesis report.

Experimental characterization of the AIFIRA CPM using a track detector

Fluorescent Nuclear Track Detectors (FNTDs)⁶⁴ were used to characterize the microbeam quality (size and intensity) and targeting accuracy at cellular scale for single and several particle tracks. FNTD detectors were irradiated with focalized protons and α -particle. Single proton and α -particle track have been investigated in 3D after confocal laser scanning microscopy acquisitions (CLSM), which allows us to access to LET value, to track length and particle spot lateral size (detector response). Pattern with more than a particle per spot allow us to establish a relationship between the intensity variation and the ED.

Cellular micro-irradiation: Kinetic study of DNA repair proteins

The kinetic dynamics of two stable cell lines expressing GFP-tagged protein (Green Fluorescent Protein) involved in the recognition, signaling and repair of radiation-induced DNA damage, were investigated. The two proteins are GFP-XRCC1 (Single Strand Breaks and BER/NER pathways) and GFP-RNF8 (Double Strand Breaks ligase protein), details were

published previously in ⁶⁵. The two cell lines nuclei were micro-irradiated with an increasing number of 3 MeV α -particles and protons using the AIFIRA microbeam. These proteins accumulate at DNA damage sites and form large nuclear aggregates that appear as Ionizing Radiation-Induced Foci (IRIF)⁶⁶. These IRIF are highly dynamic structures and subject to precise spatio-temporal regulation. The kinetics of how these lesions are processed and resolved after irradiations can be provided by the precise order and timing of protein recruitments⁶⁷. The kinetics profiles of these proteins were then correlated to the number of delivered particles, the ED, the particle LET, and the predicted number of DNA damage.

Multicellular micro-irradiation: Radio-induced effect *in vivo*

Two different stages of a living organism, *C. elegans*, were irradiated *in vivo*.

To validate the experimental procedure to micro-irradiate a multicellular living organism in development using the AIFIRA microbeam and to observe the radio-induced effects and the transmission of damage signaling in real time, a specific cell from two cell stage embryos were irradiated with protons. The first cell division was followed using time-lapse imaging system. IRIF and chromosomal aberrations were observed in the irradiated cell nucleus and also in the daughter cells. A synchronization disruption of cell divisions within the 4-cell stage was also observed.

To study chronic induced stress response after exposure to IRs, *C.elegans* L1 larvae have been chosen to be irradiated because of the presence of the two somatic gonad precursor cells at this stage. These 2 cells give rise to the entire somatic gonad responsible of the production of gametes (called testes in male and ovaries in female)⁶⁸.

To determine the specific contribution of these cells in the stress response of IR, they were irradiated with 3 MeV protons using AIFIRA microbeam. The challenge was to perform the irradiation of these 2 small cells (3.32 μm diameter) in a living organism that moves using the AIFIRA microbeam. To overcome this challenge, the dose must be delivered homogeneously to the area around the 2 cells by using CPM irradiation. *C. elegans* L1 larvae stage were irradiated with 0.3 Gy, 3 Gy and 30 Gy to compare the results with a second irradiation strategy where the whole larvae is irradiated with the 3 different cumulative doses of gamma rays performed at the MIRE platform⁶⁹ (collaboration with the IRSN).

V. Microdosimetry

Microdosimetry is the theoretical or experimental investigation of imparted energy probability distributions in a cellular or sub-cellular volume of matter that is traversed by an ionizing particle. This original approach was founded by Harald H. Rossi, when he recognized the fundamental difference between macroscopic absorbed dose and the fluctuation of ED in microscopic structures described by stochastic variables^{70,71}. Using this concept, physical quantities can be calculated with a full theoretical body, which describe the radiation interaction with the matter, or measured with specific detectors⁷².

Performing targeted irradiations with a microbeam, ED is localized in a cellular/sub-cellular structure and the responses to IRs depends on its stochastic distribution, which in turn, depends on the type and energy of particles and on the target size (different compartments of the irradiated sample). For biological samples, the main target of IR is the DNA and its size is smaller than the lateral extension of the ionization cloud surrounding the majority of charged-particles used in radiobiological experiments. It is therefore reasonable to think that the ionization fluctuations, and hence the biological effectiveness, depend on the position of the site within the particle track. Therefore, the track structure, based on the microdosimetry concept, is believed to be very important to understand and explain results that apparently have no suitable explanation by considering only average quantities like absorbed dose. Track structure relates to the manner or pattern in which energy is deposited in a medium by tracks of particles as they slow down.

In our CPM studies, the dosimetric quantities of interest are not measurable directly during micro-irradiation. Nevertheless, physical characteristics of the ion track structure can be measured offline by using track detectors and physical quantities can be simulated by using Monte Carlo codes.

Track detectors

Microdosimetry detectors have been used widely for qualitatively and quantitatively analyzing and detecting radiation. Traditionally, the Tissue Equivalent Proportional Counters (TEPC) has been used to estimate microdosimetrical quantities. They are based on gas proportional counters with a rigid wall made of tissue equivalent plastic surrounding a gas filled cavity. TEPC present several limits (spatial resolution, time response, need of a gas supply and a high voltage...) which make it non-useful in many applications⁷³. In contrast,

semiconductor detectors are widely used in radiation detection because they are small, have a high energy resolution in particle detection, a low bias voltage, and a fast response time. Over the 20 last years, the Center for Medical Radiation Physics (CMRP) at the University of Wollongong (Australia) has developed semiconductor microdosimeter and the most current Silicon on Insulator (SOI) detectors (five generations) for RBE (Relative biological effectiveness) characterization in different radiation fields of hadron therapy facilities⁷⁴. Another example of active microdosimeter is the prototypes of scCVD diamond membrane based microdosimeters for hadron therapy developed for more than 10 years at the Diamond Sensors Laboratory of CEA-LIST (France). These detectors are characterized by using 2 MeV protons at the AIFIRA microbeam and 16.6 MeV carbons at the IRB Croatia (Institute Ruđer Bošković)⁷⁵.

Apart from the active microdosimetry detectors already mentioned, passive microdosimetry detectors that do not provide direct readouts of the recorded ED of the incident radiation are also available. Track detectors are part of passive microdosimetry detectors that allow to measure and visualize particle track structures experimentally. The size and the shape of these tracks yield information about the particle energy and its physical processes distribution. In general, we can distinguish between gas track structure detectors⁷⁶ and solid track structure detectors. The most common solid track detectors are CR39 Plastic Nuclear Track Detectors (PNTDs) and Fluorescent Nuclear Track Detectors (FNTD).

CR39 PNTDs have been widely used for more than 30 years for various common applications (radon monitoring⁷⁷, neutron dosimetry⁷⁸, the radiotherapy dosimetry⁷⁹...). Additionally, they can be used as LET spectrometers allowing to estimate the quality of irradiation^{80, 81}. Ionizing particles leave narrow trails of damage referred to as latent tracks fixed by chemical etching and observed under an optical microscope.

FNTDs are novel track detectors based on Al₂O₃:C,Mg single crystals allowing the detection and visualization of highly localized EDs of individual charged-particle tracks through its volume with sub-micrometer resolution and a full 3D resolution. FNTDs contain aggregate color centers (F-center) exhibiting radio-chromatic transformation under IR. These transformed centers produce high yield fluorescence when stimulated with confocal laser scanning microscopy (CLSM), enabling non-destructive read-out with the intensity signal depending on the local ED⁸²⁻⁸⁵.

Monte Carlo simulation codes : Geant4/Geant4-DNA

IR interactions at the micrometer and sub-micrometer scales have a fundamental role in the initial formation of biological DNA damage. However, experimental data of ionization yield in condensed DNA material are not directly measurable during irradiation with the currently available techniques.

Theoretical simulations using Monte Carlo techniques and methods allow their calculation and quantification in well-defined conditions (beam extraction and focalization, realistic phantom of cellular volume...). These codes reproduce the stochastic nature of the interaction of elementary particles with matter using random draws.

Several Monte Carlo codes based on macroscopic description of the particle transport like Fluka⁸⁶, MCNP/MCNPX⁸⁷, Penelope⁸⁸ and, Geant4^{89, 90} were developed originally for modeling physics experiments of radiation-matter interactions (nuclear physics and particle physics). Some of them are extended for biophysics, dosimetry and microdosimetry, clinical radiotherapy, and radiation protection applications. Monte Carlo codes that characterize the primary properties of radiation tracks and microdosimetric quantities are referred to as track structure codes. Track structure codes allow to calculate the physical interactions and the EDs of ionizing particles within biological matter by modeling particle tracks “step-by-step” at the nanometric scale and low energy. Some codes are limited to the simulation of the physical interactions, while others include the simulation of the physical, the physico-chemical and chemical stages as well as the biological damage and repair processes quantification^{91, 92}. The main references are the KURBUC code^{93,94}, the PARTRAC code^{95,96}, the open source toolkit Geant4-DNA^{97,98} and the Geant4-DNA based MC code TOPAS-nBio⁹⁹.

Since 2007, the Geant4-DNA project was developed to extend the Geant4 toolkit (an open-source and publicly available simulation platform) to molecular level simulations^{97,98,100,101}. It has been widely adopted as investigation tool in the radiobiology^{102–108} and radiation therapies community^{109–111}. Regardless of the physics models chosen in Geant4-DNA, all electromagnetic interactions of particles (electrons, α -particles, protons and neutral hydrogen atoms) with their surrounding medium (liquid water) are discrete. For α -particles, protons and neutral hydrogen atoms these interactions are nuclear scattering, ionization, electronic excitation or charge exchange. For electrons the interactions are elastic scattering, electronic excitation, vibrational excitation, ionization or molecular attachment. This permits the simulation to achieve a very high spatial accuracy, down to the nanometer scale, whilst the statistical nature of the Monte Carlo simulations ensures quantum limits are not violated¹¹². The physics modeling in Geant4-DNA takes place rapidly compared to other events and is

typically said to have terminated within 1 fs. The propagation of particles takes place in liquid water (validation data is frequently based upon data coming from the vapor or solid phases of water, due to the experimental difficulties of measuring interaction cross- sections in liquid). Particles are tracked down to energies around 8 eV, where they are solvated or thermalized⁹⁷. The electron interactions were modeled down to eV energies since 50% of all ionizations are produced by electrons with energy less than 1 keV in the case of irradiation with proton beam¹¹³.

The iRiBio (*ionizing Radiation interactions and Biology*) group has initiated a simulation activity based on the Geant4 simulation toolkit in order to develop models for track structure calculation of IR traversals through living biological specimens and to compare prediction results with experimental data¹¹⁴. The Geant4-DNA tracking capabilities at the sub-micrometer scale were first extended and validated by the group, allowing to propose a complete simulation platform for the design of specific micron and sub-micron beam irradiation¹¹⁵. Barberet *et al.* developed a methodology to provide microdosimetric quantities calculated from realistic cellular volumes for two types of irradiation protocols: the 3 MeV α -particle microbeam at AIFIRA used for targeted irradiation and a ^{239}Pu alpha source used for large angle random irradiation¹⁰². A correlation between the ED along the ion tracks and the DNA damage signaling proteins obtained by using immunocytofluorescence has been shown for ^{239}Pu alpha source. For microbeam irradiations, the damaged areas showed a bigger diameter compared to the area where the energy is deposited according to the simulation. This was explained by the beam scattering, the targeting accuracy of the microbeam and the influence of the biological processes such as chromatin mobility¹⁰².

These setups allow for example a precise control of delivered ionizing doses by a microbeam to living organisms. In this manner the total energy distribution after microbeam irradiation can be calculated and early biological damage induced by IRs at the DNA scale can be estimated.

In this context, during the PhD my efforts were dedicated to developed microdosimetric models for measuring or simulating physical quantities that cannot be measured directly during irradiations at the AIFIRA microbeam facility. Using the toolkit Geant4 and Geant4-DNA track structure code, the link between the physical characterization of IR and its biological effects at the cellular scale have been established relying on the microdosimetric quantities. The idea was to correlate these quantities, mainly ED, specific energy and DNA damage with the effects observed when cells were irradiated with CPM.

This manuscript is structured in three main parts.

- **PART I: Experimental characterization of the charged-particles microbeam using FNTDs**

In this part, we developed a protocol (i) to set up the irradiation of Fluorescent Nuclear Track Detector (FNTD) with protons and α -particles at the AIFIRA CPM and (ii) to read-out the trajectories of single and multiple charged-particles throughout the detector volume with sub-micrometer resolution and full 3D information using confocal laser scanning microscopy. We used FNTD detectors to visualize experimentally the different characteristics of the ion microbeam, such as the size, the intensity (as function of the number of the delivered particles) and the positioning accuracy of the system for different proton and α -particle LETs. Preliminary results of FNTD test irradiations with single tracks and increasing number of proton and α -particle are presented. It shows the capability of FNTDs to provide detailed characterization of the CPM beam spot (size and positioning accuracy) the detection efficiency with sub-micrometer resolution with full 3D information. It allows the reconstruction of the particle tracks in relation with the particles LET.

- **PART II: Kinetic study of detection and repair of DNA damage proteins after irradiations at cellular scale**

For the analysis of the dynamics of GFP-labeled proteins (GFP-XRCC1 and GFP-RNF8) involved in signaling and repair of DNA damage after irradiations with an increasing number of 3 MeV α -particles and protons, first, the track structure of one α -particle and one proton are reconstructed from simulated data to compare the ED distribution for the 2 types of particles.

To compare the proteins recruitment time responses after irradiations with the 2 types of particles in a cell nucleus, I simulated the energy distribution in a homogeneous liquid water cube of 6 μ m in thickness corresponding to the average thickness of human cell and then clustered them based on the “Clustering” example of Geant4-DNA to predict the number of 3 types of DNA damage (Single Strand Breaks (SSBs), Double Strand Breaks (DSBs) and Complex Strand Breaks (CSB))^{116,98}. The clustering of the DNA damage was performed also at the chromatin sub-structure scale (micrometer scale) to investigate their spatial distribution and to determine their complexities.

- **PART III: Multicellular micro-irradiation: Biological radio-induced effects by ionizing radiations *in vivo***

To characterize the irradiation of *C. elegans* embryo with 3 MeV protons for studying the radio-induced effects at the DNA scale during the first cell division, I simulated the ED distribution in a *C. elegans* embryo modeled as realistic phantom based on high resolution confocal imaging^{102, 114}. The energy distribution was simulated in 3 different compartments of the *C. elegans* embryo (chromatin, nuclear volume and the whole embryo) using a 3D cellular “phantom”. These “phantoms” allow high-resolution modeling of the embryo geometries and a realistic estimation of the ED enabling to consider the chromatin condensation state during embryos development. Several embryo nuclei having different chromatin condensations were tested to investigate if the chromatin condensation had an impact on the ED during our irradiation.

For the study of chronic induced stress response after exposure to IRs of *C.elegans* L1 larvae⁶⁹, and to compare the two irradiation strategies (at MIRE and AIFIRA) for the 3 doses (0.3 Gy, 3 Gy and 30 Gy), the aim of my contribution was to model the micro-irradiation of *C. elegans* L1 larva with 3 MeV protons in Geant4 and to find a way to deliver homogeneously the 3 selective doses to the area around the 2 somatic gonad precursor cells by using the CPM at the AIFIRA facility. Several patterns and microbeam sizes were tested to choose the most adequate configuration.

References

1. ICRU Report 33. *Radiation Quantities and Units*, (International Commission on Radiation Units and Measurements, Bethesda, MD). (1980).
2. Hall, E. J. & Giaccia, A. J. *Radiobiology for the Radiologist: 7th edition*, Lippincott Williams and Wilkins Publishing; ISBN 978-1-60831-193-4; 546 pages; Hardback. (2012).
3. ICRU Report 60. *Fundamental Quantities and Units of Ionizing Radiation* (International Commission on Radiation Units and Measurements, Bethesda, MD). (1998).
4. Fleet, A. *Radiobiology for the Radiologist: 6th edition*, Eric J. Hall, Amato J. Giaccia, Lippincott Williams and Wilkins Publishing; ISBN 0-7817-4151-3; 656 pages; Hardback; £53. *J. Radiother. Pract.* **5**, 237–237 (2006).
5. Lorat, Y. *et al.* Nanoscale analysis of clustered DNA damage after high-LET irradiation by quantitative electron microscopy - The heavy burden to repair. *DNA Repair (Amst)*. **28**, 93–106 (2015).
6. McLaughlin, W. L. THE MEASUREMENT OF ABSORBED DOSE AND DOSE GRADIENTS. 9–38 (1980).
7. Morgan, W. F. & Bair, W. J. Issues in Low Dose Radiation Biology: The Controversy Continues. A Perspective. *Radiat. Res.* **179**, 501–510 (2013).
8. Randers-Pehrson, G. Microbeams, microdosimetry and specific dose. *Radiat Prot Dosim.* **99**, 471–472 (2002).
9. Kellerer, A. M. & Chmelevsky, D. Concepts of microdosimetry - I. Quantities. *Radiat. Environ. Biophys.* **12**, 61–69 (1975).
10. ICRU Microdosimetry Report 36. *Bethesda, MD: International Commission on Radiation Units and Measurements*. (1983).
11. Suzuki, K., Yamauchi, M., Oka, Y., Suzuki, M. & Yamashita, S. A novel and simple micro-irradiation technique for creating localized DNA double-strand breaks. *Nucleic Acids Res.* **38**, (2010).
12. Suzuki, K., Yamauchi, M., Oka, Y., Suzuki, M. & Yamashita, S. Creating localized DNA double-strand breaks with microirradiation. *Nat. Protoc.* **6**, 134–139 (2011).
13. Mortusewicz, O., Leonhardt, H. & Cardoso, M. C. Spatiotemporal dynamics of regulatory protein recruitment at DNA damage sites. *J. Cell. Biochem.* **104**, 1562–1569

- (2008).
14. Gassman, N. R. & Wilson, S. H. Micro-irradiation tools to visualize base excision repair and single-strand break repair. *DNA Repair (Amst)*. **31**, 52–63 (2015).
 15. Solarczyk, K. J., Kordon, M., Berniak, K. & Dobrucki, J. W. Two stages of XRCC1 recruitment and two classes of XRCC1 foci formed in response to low level DNA damage induced by visible light , or stress triggered by heat shock. *DNA Repair (Amst)*. **37**, 12–21 (2016).
 16. Feng, L. & Chen, J. The E3 ligase RNF8 regulates KU80 removal and NHEJ repair. *Nat. Struct. Mol. Biol.* **19**, 201–206 (2012).
 17. Mailand, N. *et al.* RNF8 Ubiquitylates Histones at DNA Double-Strand Breaks and Promotes Assembly of Repair Proteins. *Cell* **131**, 887–900 (2007).
 18. Drexler, G. A. & Ruiz-Gómez, M. J. Microirradiation techniques in radiobiological research. *J. Biosci.* **40**, 629–643 (2015).
 19. Tobias, F., Durante, M., Taucher-Scholz, G. & Jakob, B. Spatiotemporal analysis of DNA repair using charged particle radiation. *Mutat. Res. - Rev. Mutat. Res.* **704**, 54–60 (2010).
 20. Tobias, F. *et al.* Spatiotemporal Dynamics of Early DNA Damage Response Proteins on Complex DNA Lesions. *PLoS One* **8**, e57953 (2013).
 21. Kraft, G. *et al.* Irradiation chamber and sample changer for biological samples. *Nucl. Instruments Methods* **168**, 175–179 (1980).
 22. M. Belli, R. Cherubini, G. Galeazzi , S. Mazzucato, G. Moschini, O. Sapor, G. S. and M. A. T. Proton irradiation facility for radiobiological studies at a 7 MN Can De Graaff accelerator. *Lichenol. Lat. Am. Hist. Curr. Knowl. Appl.* **256**, 576–580 (1998).
 23. Folkard, M. *et al.* Inactivation of V79 cells by low-energy protons, deuterons and helium-3 ions. *Int. J. Radiat. Biol.* **69**, 729–738 (1996).
 24. Besserer, J. *et al.* An irradiation facility with a vertical beam for radiobiological studies. *Nucl. Instrum. Methods Phys. Res. A* **430**, 154–160 (1999).
 25. Scampoli, P. *et al.* Low-energy light ion irradiation beam-line for radiobiological studies. *Nucl. Instruments Methods Phys. Res. Sect. B Beam Interact. with Mater. Atoms* **174**, 337–343 (2001).
 26. Wéra, A. C., Riquier, H., Heuskin, A. C., Michiels, C. & Lucas, S. In vitro irradiation station for broad beam radiobiological experiments. *Nucl. Instruments Methods Phys. Res. Sect. B Beam Interact. with Mater. Atoms* **269**, 3120–3124 (2011).
 27. Friedrich, T., Scholz, U., Elsässer, T., Durante, M. & Scholz, M. Systematic analysis of

- RBE and related quantities using a database of cell survival experiments with ion beam irradiation. *J. Radiat. Res.* **54**, 494–514 (2013).
28. Prise, K. M., Schettino, G., Vojnovic, B., Belyakov, O. & Shao, C. Microbeam studies of the bystander response. *J. Radiat. Res.* **50**, A1–A6 (2009).
29. Braby, L. A. & Reece, W. D. Studying low dose effects using single particle microbeam irradiation. *Radiat Prot Dosim.* **31**, 311–314 (1990).
30. Geard, C. R., Brenner, D. J., Randers-Pehrson, G. & Marino, S. A. Single-particle irradiation of mammalian cells at the radiological research accelerator facility: induction of chromosomal changes. *Nucl. Inst. Methods Phys. Res. B* **54**, 411–416 (1991).
31. GERARDI, S. Ionizing Radiation Microbeam Facilities for Radiobiological Studies in Europe. *J. Radiat. Res.* **50**, A13–A20 (2009).
32. Prise, K. M. & Schettino, G. Microbeams in radiation biology: Review and critical comparison. *Radiat. Prot. Dosimetry* **143**, 335–339 (2011).
33. Barberet, P. & Seznec, H. Advances in microbeam technologies and applications to radiation biology. *Radiat. Prot. Dosimetry* **166**, 182–187 (2015).
34. Miller, R. C., Randers-Pehrson, G., Geard, C. R., Hall, E. J. & Brenner, D. J. The oncogenic transforming potential of the passage of single particles through mammalian cell nuclei. *Proc. Natl. Acad. Sci.* **96**, 19–22 (1999).
35. Hei, T. K. *et al.* Mutagenic effects of a single and an exact number of α particles in mammalian cells. *Proc. Natl. Acad. Sci.* **94**, 3765–3770 (1997).
36. M. A. Kadhim, S. J. Marsden, A. M. Malcolmson, M. Folkard, D. T. Goodhead, K. M. P. and B. D. M. Long-Term Genomic Instability in Human Lymphocytes Induced by Single-Particle Irradiation. *Radiat. Res.* **155**, 122–126 (2001).
37. Tartier, L., Gilchrist, S., Burdak-Rothkamm, S., Folkard, M. & Prise, K. M. Cytoplasmic irradiation induces mitochondrial-dependent 53BP1 protein relocalization in irradiated and bystander cells. *Cancer Res.* **67**, 5872–5879 (2007).
38. Walsh, D. W. M. *et al.* Live cell imaging of mitochondria following targeted irradiation in situ reveals rapid and highly localized loss of membrane potential. *Sci. Rep.* **7**, 46684 (2017).
39. Jakob, B. *et al.* DNA double-strand breaks in heterochromatin elicit fast repair protein recruitment, histone H2AX phosphorylation and relocation to euchromatin. *Nucleic Acids Res.* **39**, 6489–6499 (2011).
40. Bourret, S. *et al.* Fluorescence time-lapse imaging of single cells targeted with a

- focused scanning charged-particle microbeam. *Nucl. Instruments Methods Phys. Res. Sect. B Beam Interact. with Mater. Atoms* **325**, 27–34 (2014).
41. Hable, V. *et al.* The live cell irradiation and observation setup at SNAKE. *Nucl. Instruments Methods Phys. Res. Sect. B Beam Interact. with Mater. Atoms* **267**, 2090–2097 (2009).
42. Hable, V. *et al.* Recruitment kinetics of DNA repair proteins Mdc1 and Rad52 but not 53BP1 depend on damage complexity. *PLoS One* **7**, 1–11 (2012).
43. Guo, N. *et al.* Live cell imaging combined with high-energy single-ion microbeam. *Rev. Sci. Instrum.* **87**, (2016).
44. Mosconi, M. *et al.* 53BP1 and MDC1 foci formation in HT-1080 cells for low- and high-LET microbeam irradiations. *Radiat. Environ. Biophys.* **50**, 345–352 (2011).
45. Greubel, C. *et al.* Competition effect in DNA damage response. *Radiat. Environ. Biophys.* **47**, 423–429 (2008).
46. Girst, S. *et al.* Subdiffusion supports joining of correct ends during repair of DNA double-strand breaks. *Sci. Rep.* **3**, 1–6 (2013).
47. Zlobinskaya, O., Girst, S., Greubel, C. & Hable, V. Reduced side effects by proton microchannel radiotherapy : study in a human skin model Reduced side effects by proton microchannel radiotherapy : study in a human skin model. *Radiat Env. Biophys* **52**, 123–133 (2013).
48. Miller, J. H., Chrisler, W. B., Wang, X. & Sowa, M. B. Confocal microscopy for modeling electron microbeam irradiation of skin. *Radiat Env. Biophys* **50**, 365–369 (2011).
49. Belyakov, O. V *et al.* Biological effects in unirradiated human tissue induced by radiation damage up to 1 mm away. *PNAS* **102**, 14203–14208 (2005).
50. Sedelnikova, O. A. *et al.* DNA double-strand breaks form in bystander cells after microbeam irradiation of three-dimensional human tissue models. *Cancer Res.* **67**, 4295–4302 (2007).
51. Merz, F. *et al.* Tissue slice cultures from humans or rodents : a new tool to evaluate biological effects of heavy ions. *Radiat Env. Biophys* **49**, 457–462 (2010).
52. Schmid, T. E. *et al.* Relative biological effectiveness of pulsed and continuous 20 MeV protons for micronucleus induction in 3D human reconstructed skin tissue. *Radiother. Oncol.* **95**, 66–72 (2010).
53. Fukamoto, K. *et al.* Development of the Irradiation Method for the First Instar Silkworm Larvae Using Locally Targeted Heavy-ion Microbeam. *J. Radiat. Res* **48**,

- 247–253 (2007).
54. Choi, W. V. Y. *et al.* Adaptive Response in Zebrafish Embryos Induced Using Microbeam Protons as Priming Dose and X-ray Photons as Challenging Dose. *J. Radiat. Res* **51**, 657–664 (2010).
55. Choi, W. V. Y. *et al.* Triphasic Low-dose Response in Zebrafish Embryos Irradiated by Microbeam Protons. *J. Radiat. Res* **53**, 475–481 (2012).
56. Sugimoto, T. *et al.* Cell cycle arrest and apoptosis in *Caenorhabditis elegans* germline cells following heavy-ion microbeam irradiation. *Int. J. Radiat. Biol.* **82**, 31–38 (2006).
57. Bertucci, A., Pocock, R. D., Randers-Pehrson, G. & Brenner, D. J. Microbeam irradiation of the *C. elegans* nematode. *J. Radiat. Res.* **50**, A49–A54 (2009).
58. Adenle, A. A., Johnsen, B. & Szewczyk, N. J. Review of the results from the International *C. elegans* first experiment (ICE-FIRST). *Adv. Sp. Res.* **44**, 210–216 (2009).
59. Buonanno, M. *et al.* Microbeam irradiation of *C. elegans* nematode in microfluidic channels. *Radiat. Environ. Biophys.* **52**, 531–537 (2013).
60. Suzuki, M. *et al.* Region-specific irradiation system with heavy-ion microbeam for active individuals of *Caenorhabditis elegans*. *J. Radiat. Res.* **58**, 881–886 (2017).
61. Barberet, P. *et al.* Development of a focused charged particle microbeam for the irradiation of individual cells. *Rev. Sci. Instrum.* **76**, (2005).
62. Muggiolu, G. *et al.* Single α -particle irradiation permits real-time visualization of RNF8 accumulation at DNA damaged sites. *Sci. Rep.* **7**, 41764 (2017).
63. Barberet, P. *et al.* Cell micro-irradiation with MeV protons counted by an ultra-thin diamond membrane. *Appl. Phys. Lett.* **111**, 243701 (2017).
64. Osinga, J. *et al.* High-accuracy fluence determination in ion beams using fluorescent nuclear track detectors. **56**, 294–298 (2013).
65. Muggiolu, G. Deciphering the biological effects of ionizing radiations using charged particle microbeam: from molecular mechanisms to perspectives in emerging cancer therapies. Cancer. Université de Bordeaux. English. <NNT:2017BORD0599>. <tel-01820606>. (2017).
66. Goodarzi, A. A. & Jeggo, P. A. Irradiation induced foci (IRIF) as a biomarker for radiosensitivity. *Mutat. Res. - Fundam. Mol. Mech. Mutagen.* **736**, 39–47 (2012).
67. Bekker-Jensen, S. *et al.* Spatial organization of the mammalian genome surveillance machinery in response to DNA strand breaks. *J. Cell Biol.* **173**, 195–206 (2006).
68. Albert Hubbard, E. J. & Greenstein, D. The *Caenorhabditis elegans* gonad: A test tube

- for cell and developmental biology. *Dev. Dyn.* **218**, 2–22 (2000).
69. Lecomte-Pradines, C. *et al.* A dynamic energy-based model to analyze sublethal effects of chronic gamma irradiation in the nematode *Caenorhabditis elegans*. *J. Toxicol. Environ. Heal. - Part A Curr. Issues* **80**, 830–844 (2017).
70. Rossi, H. H. ROLE OF MICRODOSIMETRY IN RADIOBIOLOGY AND RADIATION PROTECTION. Ebert HG, Ed. *Proc. third Symp. Microdosim. Rep. No. EUR 4810. Luxembg. Comm. Eur. Communities* (1972).
71. Rossi, H. H. & Zaider, M. *Microdosimetry and Its Applications*. (Springer-Verlag Berlin Heidelberg, 1996).
72. Santa Cruz, G. A. Microdosimetry: Principles and applications. *Reports Pract. Oncol. Radiother.* **21**, 135–139 (2016).
73. Fleta, C. *et al.* 3D cylindrical silicon microdosimeters: Fabrication, simulation and charge collection study. *J. Instrum.* **10**, (2015).
74. Rozenfeld, A. B. Novel detectors for silicon based microdosimetry, their concepts and applications. *Nucl. Instruments Methods Phys. Res. Sect. A Accel. Spectrometers, Detect. Assoc. Equip.* **809**, 156–170 (2016).
75. Zahradnik, I. A. *et al.* scCVD Diamond Membrane based Microdosimeter for Hadron Therapy. *Phys. Status Solidi Appl. Mater. Sci.* **215**, 1–10 (2018).
76. Casiraghi, M., Bashkurov, V. A., Hurley, R. F. & Schulte, R. W. Characterisation of a track structure imaging detector. *Radiat. Prot. Dosimetry* **166**, 223–227 (2015).
77. Franci, D., Aureli, T. & Cardellini, F. an Alternative Calibration of Cr-39 Detectors for Radon Detection Beyond the Saturation Limit. *Radiat. Prot. Dosimetry* **172**, 496–500 (2016).
78. Reitz, G. Neutron dosimetric measurements in shuttle and MIR. *Radiat. Meas.* **33**, 341–346 (2001).
79. Shweikani, R. & Anjak, O. Estimation of photoneutron intensities around radiotherapy linear accelerator 23-MV photon beam. *Appl. Radiat. Isot.* **99**, 168–171 (2015).
80. Yokota, Y. *et al.* Development of an ion microbeam system for irradiating single plant cell[s]. *Biol Sci Sp.* **17**, 298–301 (2003).
81. Peng, S. *et al.* Measurements of the targeting accuracy of the Gray Laboratory charged-particle microbeam. *Nucl. Instruments Methods Phys. Res. Sect. B Beam Interact. with Mater. Atoms* **179**, 145–150 (2001).
82. Osinga, J. M. Fluorescent Nuclear Track Detectors: High-Accuracy Fluence Determination in Ion Beams. (Faculty of Natural Sciences II - Chemistry, Physics and

- Mathematics, Heidelberg, 2012).
83. Kouwenberg, J. J. M., Pooter, J. A. De, Wolterbeek, H. T., Denkova, A. G. & Bos, A. J. J. Alpha radiation dosimetry using Fluorescent Nuclear Track Detectors. *Radiat. Meas.* **113**, 25–32 (2018).
 84. Greubel, C. *et al.* Low LET proton microbeam to understand high-LET RBE by shaping spatial dose distribution. *Nucl. Instruments Methods Phys. Res. Sect. B Beam Interact. with Mater. Atoms* **404**, 155–161 (2017).
 85. Sawakuchi, G. O. *et al.* Nanoscale measurements of proton tracks using fluorescent nuclear track detectors. *Med. Phys.* **43**, 2485–2491 (2016).
 86. Ferrari, A. Sala, P.R. Fasso, A. Ranft, J. FLUKA: A multi-particle transport code (Program version 2005). *Cern-2005-010* (2005). doi:10.5170/cern-2005-010
 87. X-5 Monte Carlo Team. MCNP — A General Monte Carlo N-Particle Transport Code, Version 5. (2003).
 88. Salvat, F., Fernández-Varea, J. M. & Sempau, J. *PENELOPE -2006 : A Code System for Monte Carlo Simulation of Electron and Photon Transport ORGANISATION FOR ECONOMIC CO-OPERATION AND DEVELOPMENT.* (2006).
 89. Agostinelli, S. *et al.* GEANT4 - A simulation toolkit. *Nucl. Instruments Methods Phys. Res. Sect. A Accel. Spectrometers, Detect. Assoc. Equip.* **506**, 250–303 (2003).
 90. Allison, J. Amako, K. Apostolakis, J. H. Araujo, P. Arce Dubois, M. Asai, G. Barrand, R. Capra, S. C. *et al.* Geant4 Developments and Applications. *IEEE Trans. Nucl. Sci.* **53**, 270 – 278 (2006).
 91. Nikjoo H., Uehara S., Wilson W. E., Hoshi M. & Goodhead D. T. Track structure in radiation biology: theory and applications. *Int. J. Radiat. Biol.* **73**, 355–364 (1998).
 92. Nikjoo, H., Uehara, S., Emfietzoglou, D. & Cucinotta, F. A. Track-structure codes in radiation research. *Radiat. Meas.* **41**, 1052–1074 (2006).
 93. Nikjoo, H., O'Neill, P., Goodhead, D. T. & Terrissol, M. Computational modelling of low-energy electron-induced DNA damage by early physical and chemical events. *Int. J. Radiat. Biol.* **71**, 467–483 (1997).
 94. Nikjoo, H., Neill, P. O., Wilson, W. E. & Goodhead, D. T. Computational Approach for Determining the Spectrum of DNA Damage Induced by Ionizing Radiation. **583**, 577–583 (2001).
 95. Friedland, W., Jacob, P., Bernhardt, P., Paretzke, H. G. & Dingfelder, M. Simulation of DNA damage after proton irradiation. *Radiat. Res.* **159**, 401–10 (2003).
 96. Alloni, D., Campa, A., Friedland, W., Mariotti, L. & Ottolenghi, A. Track structure,

- radiation quality and initial radiobiological events: Considerations based on the PARTRAC code experience. *Int. J. Radiat. Biol.* **88**, 77–86 (2012).
97. Incerti, S., Douglass, M., Penfold, S., Guatelli, S. & Bezak, E. Review of Geant4-DNA applications for micro and nanoscale simulations. *Phys. Medica* **32**, 1187–1200 (2016).
 98. Bernal, M. A. *et al.* Track structure modeling in liquid water: A review of the Geant4-DNA very low energy extension of the Geant4 Monte Carlo simulation toolkit. *Phys. Med.* **31**, 861–74 (2015).
 99. McNamara, A. *et al.* Validation of the radiobiology toolkit TOPAS-nBio in simple DNA geometries. *Phys. Medica* **33**, 207–215 (2017).
 100. Chauvie, S. *et al.* Geant4 physics processes for microdosimetry simulation: Design foundation and implementation of the first set of models. *IEEE Trans. Nucl. Sci.* **54**, 2619–2628 (2007).
 101. Allison, J. *et al.* Recent developments in GEANT4. *Nucl. Instruments Methods Phys. Res. Sect. A Accel. Spectrometers, Detect. Assoc. Equip.* **835**, 186–225 (2016).
 102. Barberet, P. *et al.* Monte-Carlo dosimetry on a realistic cell monolayer geometry exposed to alpha particles. *Phys. Med. Biol.* **57**, 2189–2207 (2012).
 103. McMahon, S. J. *et al.* Biological consequences of nanoscale energy deposition near irradiated heavy atom nanoparticles. *Sci. Rep.* **1**, 1–10 (2011).
 104. McNamara, A. L., Guatelli, S., Prokopovich, D. A., Reinhard, M. I. & Rosenfeld, A. B. A comparison of X-ray and proton beam low energy secondary electron track structures using the low energy models of Geant4. *Int. J. Radiat. Biol.* **88**, 164–170 (2012).
 105. Douglass, M., Bezak, E. & Penfold, S. Monte Carlo investigation of the increased radiation deposition due to gold nanoparticles using kilovoltage and megavoltage photons in a 3D randomized cell model. *Med. Phys.* **40**, (2013).
 106. Douglass, M., Bezak, E. & Penfold, S. Development of a radiation track structure clustering algorithm for the prediction of DNA DSB yields and radiation induced cell death in Eukaryotic cells. *Phys. Med. Biol.* **60**, 3217–3236 (2015).
 107. Meylan, S. *et al.* Simulation of early DNA damage after the irradiation of a fibroblast cell nucleus using Geant4-DNA. *Sci. Rep.* **7**, 11923 (2017).
 108. Chatzipapas, K. P., Obeidat, M., McConnell, K. A., Kirby, N. & Papanikolaou, N. Quantification of DNA double-strand breaks using Geant4-DNA. *Med. Phys.* **46**, 405–409 (2018).
 109. Huang, C. Y., Oborn, B. M., Guatelli, S. & Allen, B. J. Monte Carlo calculation of the

- maximum therapeutic gain of tumor antivascular alpha therapy. *Med. Phys.* **39**, 1282–1288 (2012).
110. Tajik, M., Rozatian, A. S. H. & Semsarha, F. Calculation of direct effects of ^{60}Co gamma rays on the different DNA structural levels: A simulation study using the Geant4-DNA toolkit. *Nucl. Instruments Methods Phys. Res. Sect. B Beam Interact. with Mater. Atoms* **346**, 53–60 (2015).
111. Pham, Q. T. *et al.* Coupling of Geant4-DNA physics models into the GATE Monte Carlo platform: Evaluation of radiation-induced damage for clinical and preclinical radiation therapy beams. *Nucl. Instruments Methods Phys. Res. Sect. B Beam Interact. with Mater. Atoms* **353**, 46–55 (2015).
112. Liljequist, D. & Nikjoo, H. On the validity of trajectory methods for calculating the transport of very low energy ($<1\text{keV}$) electrons in liquids and amorphous media. *Radiat. Phys. Chem.* **99**, 45–52 (2014).
113. Nikjoo, H. & Goodhead, D. T. Track structure analysis illustrating the prominent role of low-energy electrons in radiobiological effects of low-LET radiations. *Phys. Med. Biol.* **36**, 229–238 (1991).
114. Incerti, S. *et al.* Monte Carlo dosimetry for targeted irradiation of individual cells using a microbeam facility. *Radiat. Prot. Dosimetry* **133**, 2–11 (2009).
115. Incerti, S. *et al.* the Geant4-Dna Project. *Int. J. Model. Simulation, Sci. Comput.* **01**, 157–178 (2010).
116. Francis, Z., Villagrasa, C. & Clairand, I. Simulation of DNA damage clustering after proton irradiation using an adapted DBSCAN algorithm. *Comput. Methods Programs Biomed.* **101**, 265–270 (2011).

PART I

**Experimental characterization of the
charged-particles microbeam using FNTDs**

Introduction

The physical characteristics of the ion track structure and physical quantities of interest for radiation response studies (ED, specific energy and particles LET) are usually assessed either by numerical simulations or measured with detectors.

Measurements can be conducted by different complementary approaches using either active or passive detectors. Active detectors provide a direct readout of the recorded EDs in micrometric volumes. They are based on ionizing chambers filled with tissue equivalent gases or on semiconducting materials as silicon¹ or scCVD diamond membrane². Passive detectors accumulate particle tracks for long periods and can be readout offline. Amongst the various types of passive detectors, track detectors can be used to measure and visualize experimentally charged-particle track structure characteristics. The particle incoming energy and its distribution can be extrapolated from the size and the shape of these tracks. CR39 detectors and Fluorescent Nuclear Track Detectors FNTDs are the most commonly used solid track detectors.

CR39 Plastic Nuclear Track Detectors (PNTDs) are used as solid track etches detectors³. Energetic particles colliding with the detector structure leave a trail of damage referred to latent tracks. After chemical etching these tracks can be observed and measured under an optical microscope. The resulting etched plastic contains a permanent record of not only the location of the radiation on the plastic but also gives spectroscopic information about the source. CR39 have been used widely for more than 30 years for several applications such as radon monitoring⁴, dosimetry on board of aircrafts⁵, the dosimetry in radiotherapy⁶ and the estimation of the quality and the physical characterization of radiation. CR39 detectors are also frequently used to characterize ion microbeams^{7,8}. At the AIFIRA facility, the characteristics of the CPM, such as its size, positioning accuracy and targeting accuracy were evaluated so far using CR39^{9,10}. The use of such detector presents limitations. First, the precise measurement of single or several particle track sizes is tedious because such measurements depend highly on the chemical etching conditions (concentrations, temperature...). Second, CR39 detectors have a LET detection threshold limiting its use for particles with low LET, such as 3 MeV protons at the AIFIRA CPM.

In the last decade, FNTDs have been developed by Landauer, Inc.¹¹ to overcome some of CR39 limitations. FNTDs are based on Al₂O₃:C,Mg single crystals allowing the detection and visualization of highly localized EDs of individual charged-particle tracks with sub-

micrometer and a full 3D resolution^{12–14}. Compared to CR39 detectors, FNTDs exhibit a superior spatial resolution and do not require chemical treatment for the read-out¹³. The major advantage of using FNTD is its capability of being read out by confocal laser scanning microscopy (CLSM) commonly used in life science¹⁵. FNTDs show a high detection efficiency (close to 100%)¹⁶, a wide range of LET sensitivity¹⁷ and depth information in 3D¹⁸. FNTDs have been used so far for radiotherapy and heavy ion therapies research^{15,19}, for spectroscopic radionuclide analysis^{20,21}, and for fluence determination in ion beams^{16,22}. It has been also used more recently for microbeam characterization. Greubel *et al.* have characterized beam spot of low LET 20 MeV proton using FNTDs to correlate spot size with measured cell survival in unstained cells²³.

In this study, we used FNTDs to visualize experimentally the different characteristics of the CPM at the AIFIRA facility. We developed a protocol to micro-irradiate FNTDs with protons and α -particles and to read-out their trajectories using CLSM. Pattern irradiations with single particles and increasing number of delivered particles were performed to investigate:

- The capability of FNTDs to provide detailed characterization of the CPM beam spot: size and positioning accuracy.
- The FNTD detection efficiency with sub-micrometer resolution of single particle track especially for low LET particles.
- The exploitation of the full 3D information allowing the reconstruction of the particles tracks in relation with the particles LET and incoming energy.
- If a relationship exists between the size of detector response fluorescent spots and the LET of the particles.
- The relationship between the fluorescent intensity and the delivered dose / energy in terms of number of delivered particles per irradiated spot.

Methods

I. Fluorescent Nuclear Track Detectors (FNTDs)¹

FNTDs are single aluminum oxide crystals doped with both carbon and magnesium impurities (Al_2O_3 : C, Mg) giving them a characteristic yellow-green color. FNTDs are developed by the Crystal Growth Division of Landauer Inc., Glenwood, Illinois, USA. These crystals have been provided as samples with a dimension of $4 \times 8 \times 0.5 \text{ mm}^3$ (Fig. 3.a) *. One of the large sides is engraved with letters (Fig 3.b) and the other side is polished to obtain an optically transparent surface. Al_2O_3 : C, Mg based FNTD allows the detection and the visualization of individual charged-particle tracks thought its volume with a sub-micrometer spatial resolution giving full 3D information and high-resolution ED patterns¹⁷. These detectors are non-destructive read-out detectors, insensitive to room light before and after the irradiation and stable up to 600°C .

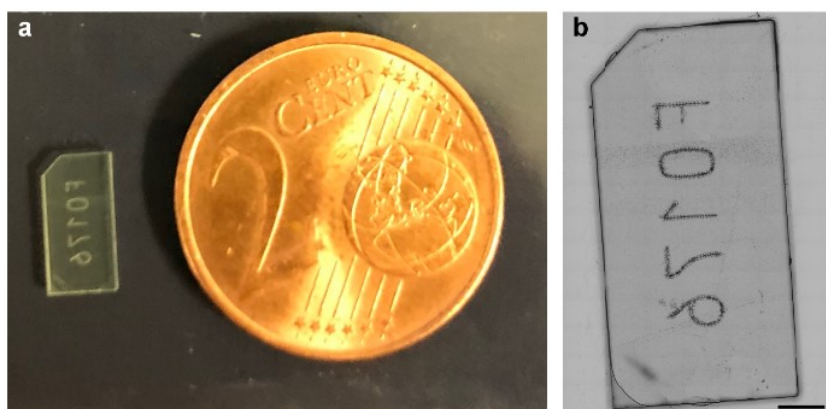


Fig. 3. a. FNTDs dimensions $4 \times 8 \times 0.5 \text{ mm}^3$. **b.** Microscopic image acquisition of the engraved side of the FNTD with 10x lens. Scale bar 1 mm.

Mg-doped Al_2O_3 crystals have green coloration and contain high concentrations of F_2^{2+} (2Mg) aggregate defects color centers (F-centers), responsible for the blue absorption band (435 nm). Al_2O_3 : C used in thermally and optically stimulated luminescence dosimetry shows an excellent dosimetric property which is the very long luminescence lifetime (35 ms) of the F-centers. These color centers undergo radiochromic transformations when exposed to IR, produce high yield fluorescence at 750 nm when stimulated at 620 nm with a short life time ($75 \pm 5 \text{ ns}$)¹³.

*We would like to thank Dr. Brahim MORENO, Landauer Inc. Paris for providing the samples and for his courtesy.

II. CPM irradiation of FNTDs

The FNTDs irradiations were carried out using the CPM at the AIFIRA facility.

First the FNTDs were cleaned using lens paper tissues soaked with ethanol. To facilitate the irradiation and the read-out microscopy after irradiation, the FNTDs were fixed from the engraved side on a glass slide using epoxy glue (Fig. 4).

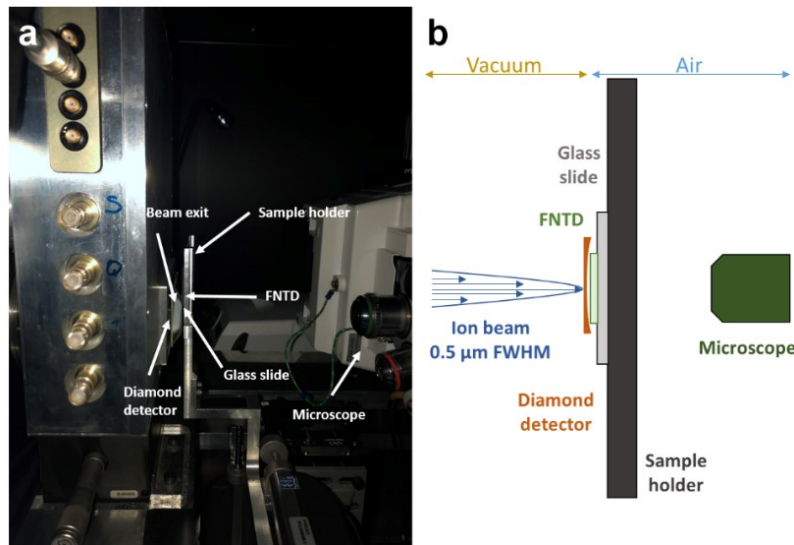


Fig. 4. Experimental set-up of CPM irradiation at the AIFIRA platform. The FNTD is glued on a microscope glass slide placed on the sample holder. The FNTD is positioned as close as possible to the exit window which is the diamond detectors. Downstream the sample, an inverted microscope installed at the end of the beam line is used for the visualization of the FNTD and to choose the irradiation position according to the engraved letters.

The glass slide was mounted on the irradiation line vertically using the same sample holder used for the biological irradiation experiments (Fig. 4). The letters engraved on the detector were used as reference for the irradiation positioning and the microscopy read-out. At the microbeam end-station, an inverted microscope is installed to visualize the samples and to choose the irradiation position according to the engraved letters. The detectors are mounted to position the polished side as close as possible to the beam exit window. They were irradiated with protons and α -particles of 1.5 MeV and 3 MeV (Fig. 4.b). Preliminary measurements were performed to study the suitability of FNTDs for single ion detection. For this purpose, irradiations, with 1 particle per point (ppp) were produced. The number of ion hits was precisely controlled by means of an ultra-thin transmission detector positioned upstream the sample : a thin single-crystal chemical-vapor-deposited (scCVD) diamond membrane²⁴ for

protons and a BNCD thin membrane² for α -particles. Irradiation patterns with increasing number of particles per points were then produced to establish the relationship between the detector response in terms of fluorescence intensity and the number of delivered particles (dose).

III. FNTDs read-out using confocal laser scanning microscopy

The FNTDs read-out was performed using a confocal laser scanning microscope (CLSM) Leica DM6 confocal microscope CFS TCS SP8 at the Bordeaux Imaging Center (BIC).

The irradiated patterns were located using the engraved letters as positioning references. However, the choice of the first stack slice corresponding to the detector surface is inaccurate, since this polished side is unmarked and difficult to spot. To overcome this problem, the images were acquired at 2 to 3 slices below the detector surface to ensure that the acquisition position is located in the detector body. A 63x oil immersion lens (Leica HC PL APO CS2 63x, numerical aperture NA = 1.4, XY resolution of about 150 nm and Z resolution of about 535 nm), 600 Hz scan speed and 96 lines averaging was used for images and z-stacks acquisition. The images pixel size in (x, y) was chosen as 0.1 μm x 0.1 μm , and the distance between 2 z-stack slices was 0.4 μm . A 638 nm laser diode with 100% intensity was used for the FNTD excitation. The fluorescence emission was detected using a photomultiplier tube (PMT) with a wavelength range between 652 nm - 800 nm and a maximum gain to detect the single particle tracks.

IV. Confocal Images processing using ImageJ

The confocal images were analyzed using the ImageJ software (<http://rsbweb.nih.gov/ij/>). The intensity profiles of the irradiated spots were measured by selecting the region around the particle impacts then by using the plot profile function of ImageJ as shown in Fig.5.

The fluorescent spot intensity profile has a Gaussian distribution. To access the intensity and the spot size, the measured data was fitted in Python with a Gaussian + linear function (Fig. 5.b):

$$I(a.u.) = A.e^{\frac{-(x-\mu)^2}{2.\sigma^2}} + ax + b \quad (1)$$

Some of the image acquisitions had a background noise with a non-homogeneous intensity values described by the linear equation added to the fit function.

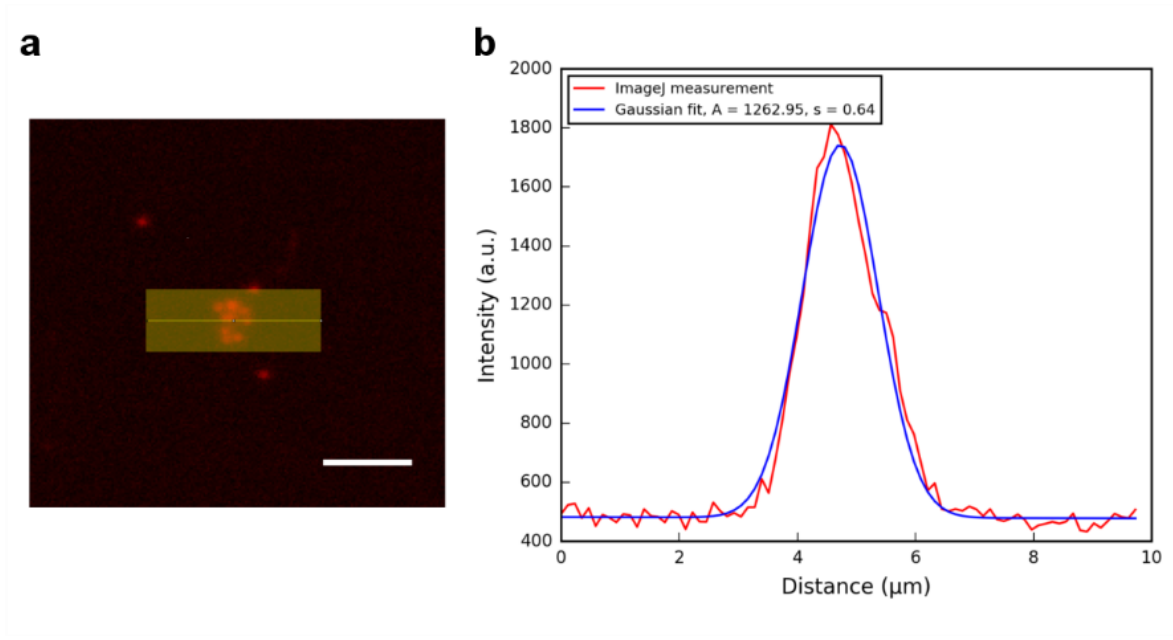


Fig. 5. a. ImageJ analyzing of selected fluorescent spot after irradiation with 12 protons of 3 MeV. **b.** The intensity profile of the selected area in (a) is plotted in red. The blue plot shows the Gaussian fit (in Python) with a max intensity value $A = 1263$ a.u. and a FWHM = $1.5 \mu\text{m}$ according to the equation (2). Scale bar = $5 \mu\text{m}$.

The fit provides 2 parameters: A is the max intensity value and σ the standard deviation. The A value is an intensity value with an arbitrary unit depending on the microscope configuration, and the spot size is given by the Full Width at Half Maximum:

$$FWHM = 2.35 \times \sigma (\mu\text{m}) \quad (2)$$

The track length through the detector body was measured from the z-stack acquisitions of single particle using the z-axis profile function in ImageJ. These z-stacks acquisitions are also exploited for the 3D particle tracks reconstruction as a surface rendering using the *Image3DViewer* plugin of ImageJ.

V. SRIM simulations

The SRIM (Stopping and Range of Ions in Matter) 2013 toolkit²⁵ was used to calculate the different particle LETs, and the energy deposition depth profile (Bragg curves) of the 4 particle LETs through the detector depth.

These simulations were carried out in Aluminum oxide (alpha) material with a density of 3.98 g/cm^3 . The Bragg curves (dE/dx ($\text{keV}/\mu\text{m}$)) were calculated as the average ED depth profile of 1000 incident particles.

Results

I. Single proton and α -particle tracks

I.1. Single particle 3D visualization

The 3D single tracks distribution of 1.5 MeV α -particles and 1.5 MeV protons are presented in Fig. 6.a and 6.b respectively. These 3D tracks are reconstructed as a surface rendering of the intensity of the stack slices using the *Image3DViewer* plug-in of ImageJ. We observed that the particle tracks get thicker while entering the detector volume. Some of the tracks contain 2 particles and we can observe the diffusion of the 2 particles through the detector (Fig. 6.b white arrow).

Unlike the CR39, FNTDs make it possible to distinguish tracks containing 2 particles from tracks with one particle.

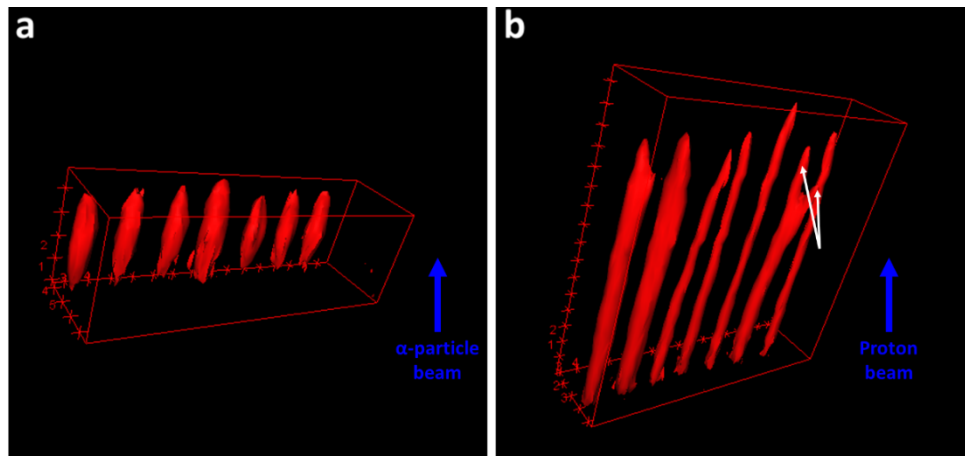


Fig. 6. A 3D surface rendering of the microscopic stack images measured for 7 single tracks distant of 2 μm with a CLSM in a FNTD after irradiation with (a) 1.5 MeV α -particles and (b) 1.5 MeV protons. The apparent length of the tracks is 4.5 μm for the α -particles and 17.3 μm for the protons averaged over 10 tracks measurements.

Single particle irradiations performed with 3 MeV α -particles and protons according to the pattern in Fig. 7.a and Fig. 8.a respectively, are shown in Fig. 7.b and Fig. 8.b. The mean single particle spot size was estimated by averaging the values obtained from 100 spots. We obtained a FWHM of $0.84 \pm 0.04 \mu\text{m}$ for 3MeV α -particles and $0.58 \pm 0.04 \mu\text{m}$ for 3 MeV protons.

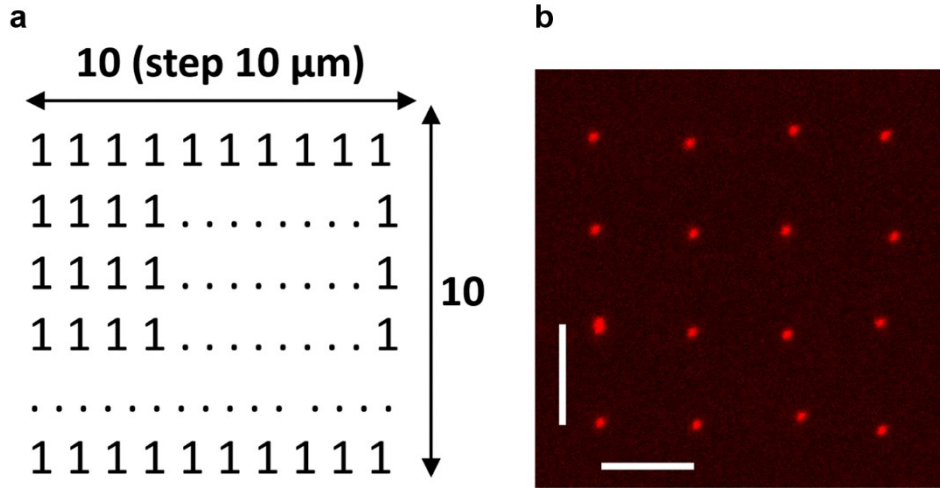


Fig. 7. Single 3 MeV α -particles detection using FNTD. **(a)** Scheme of the pattern 10 x 10 points used for the irradiation of the FNTD with 3 MeV α -particles at the AIFIRA microbeam. **(b)** Zoom on 4x4 pattern of the microscopic image acquisition using CLSM of the FNTD irradiated. Scale bar = 10 μ m.

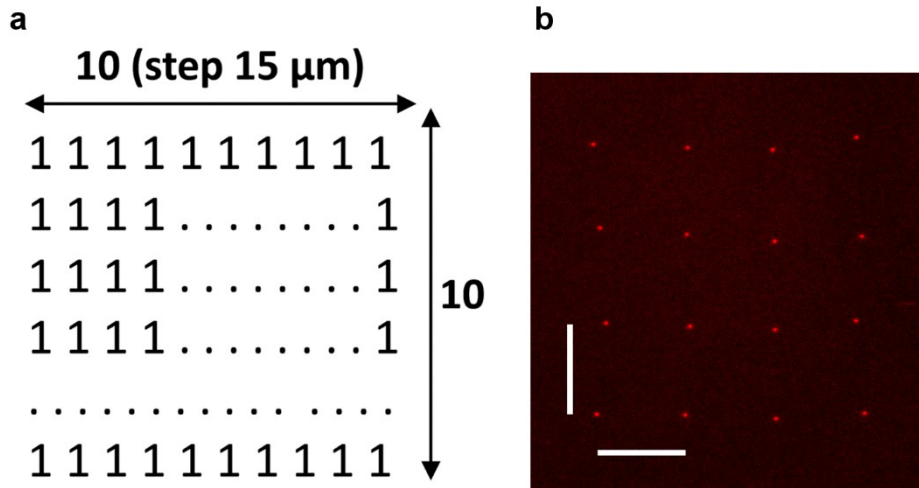


Fig. 8. Single 3 MeV protons detection using FNTD. **(a)** Scheme of the pattern 10 x 10 points used for the irradiation of the FNTD with 3 MeV protons at the AIFIRA microbeam. **(b)** Zoom on 4x4 pattern of the microscopic image acquisition using CLSM of the FNTD after irradiation. Scale bar = 15 μ m.

I.2. Single particle track length measurements

The track length of 3 MeV and 1.5 MeV protons and α -particles were measured using the z-stack acquisitions of single tracks. Fig. 9 shows the depth profiles of the fluorescence intensity of single tracks averaged over 10 different tracks measurements. The intensity values are arbitrary depending on the microscope acquisition configuration. Using these profiles, we measured a track length at the maximum intensity value of 4.5 μ m for 1.5 MeV α -particles

(Fig. 9.a), 6.7 μm for 3 MeV α -particles (Fig. 9.b), 17.3 μm for 1.5 MeV protons (Fig. 9.c) and 42.1 μm for 3 MeV protons (Fig. 9.d). The 10 values of the max intensity for each particle type and energy are located in the same stack slice and at the same depth position.

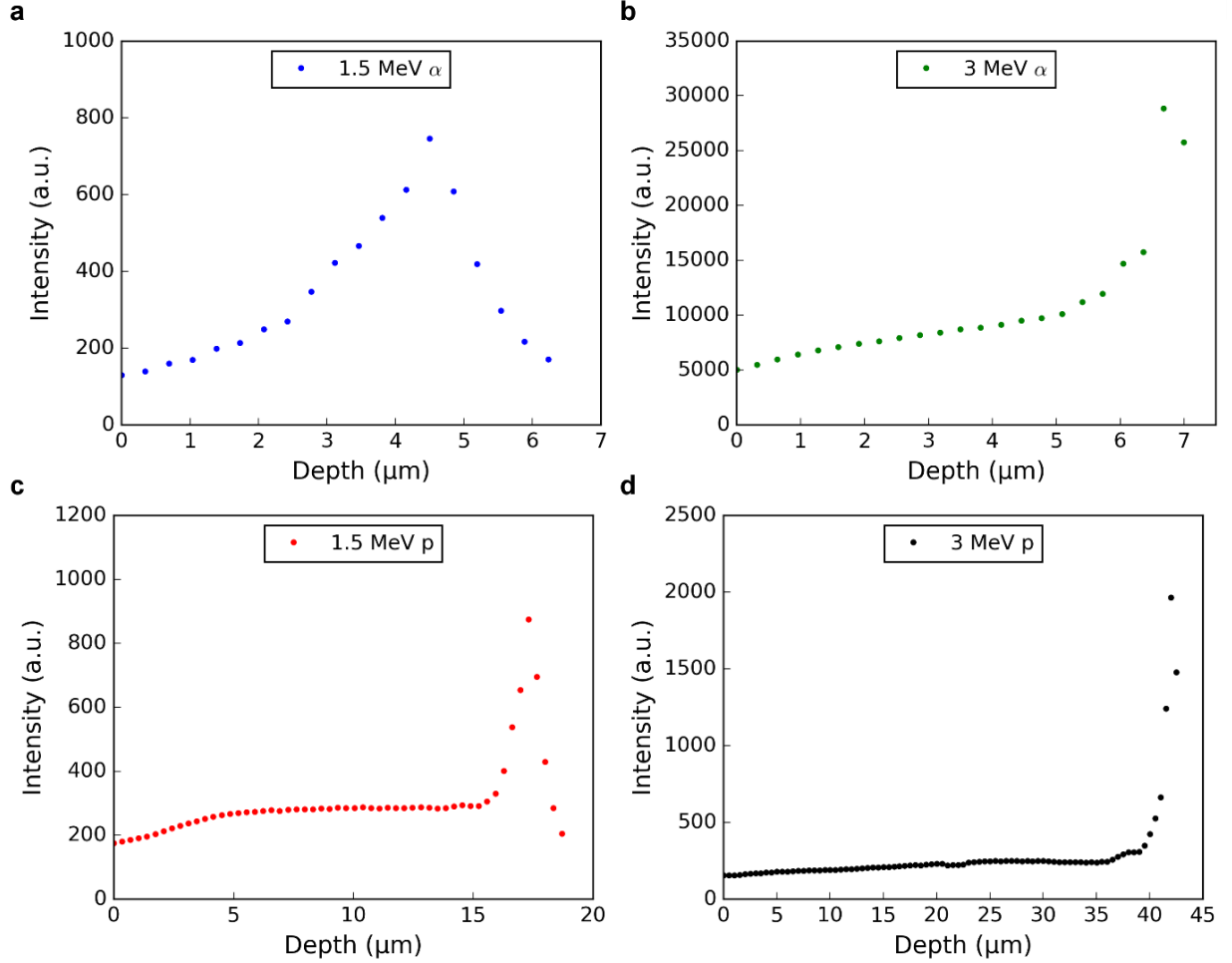


Fig. 9. Depth profiles of fluorescence intensity of single 3 MeV and 1.5 MeV protons and α -particles in the FNTD. The measurements show a track length at the maximum intensity value of (a) 4.5 μm for 1.5 MeV α -particles, (b) 6.7 μm for 3 MeV α -particles, (c) 17.3 μm for 1.5 MeV protons, and (d) 42.1 μm for 3 MeV protons.

We also simulated these track lengths averaged over 1000 particles in Aluminum oxide (alpha) material using the SRIM 2013 toolkit²⁵. We obtained a track length of 2.96 μm (1.52 μm at max intensity value) for 1.5 MeV α -particles, 6.53 μm (5.25 μm at max intensity value) for 3 MeV α -particles, 16.7 μm (16.2 μm at max intensity value) for 1.5 MeV protons, and 50.4 μm (49.5 μm at max intensity value) for 3 MeV protons (Fig. 10).

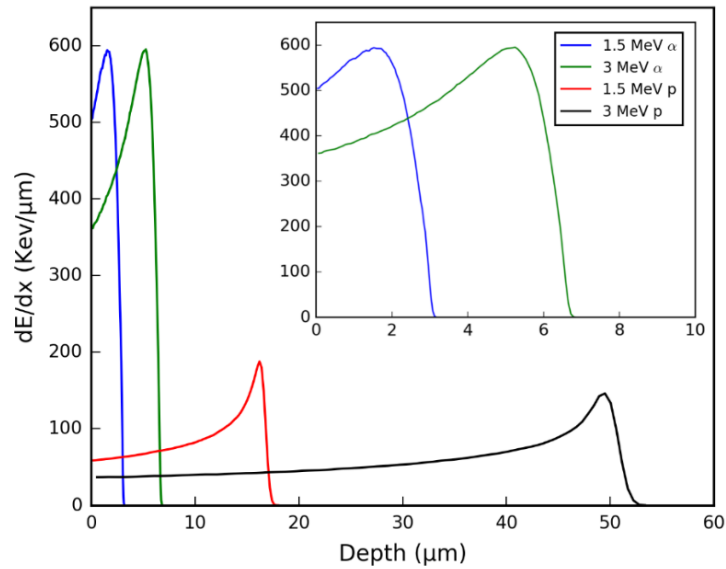


Fig. 10. SRIM 2013 simulations of energy loss average for 1000 protons and α -particles of 3 MeV and 1.5 MeV in Aluminum oxide (alpha) with a density of 3.98 g/cm^3 . Simulations show that 1.5 MeV α -particles pass through $2.96 \pm 0.12 \text{ } \mu\text{m}$, 3 MeV α -particles pass through $6.53 \pm 0.15 \text{ } \mu\text{m}$, 1.5 MeV protons pass through $16.7 \pm 0.45 \text{ } \mu\text{m}$, and 3 MeV protons pass through $50.4 \pm 0.90 \text{ } \mu\text{m}$ of Al_2O_3 before losing all their energy.

Compared to the simulated value, the track length of single particles measured using the FNTD are overestimated. For instance, the difference between the measured and the simulated averaged track length for 1.5 MeV protons (Fig. 11) can be estimated to $1 \text{ } \mu\text{m}$ to $2 \text{ } \mu\text{m}$ (corresponding to 3 to 5 slices). This overestimation could be due to the poorly choice of the stack first slices.

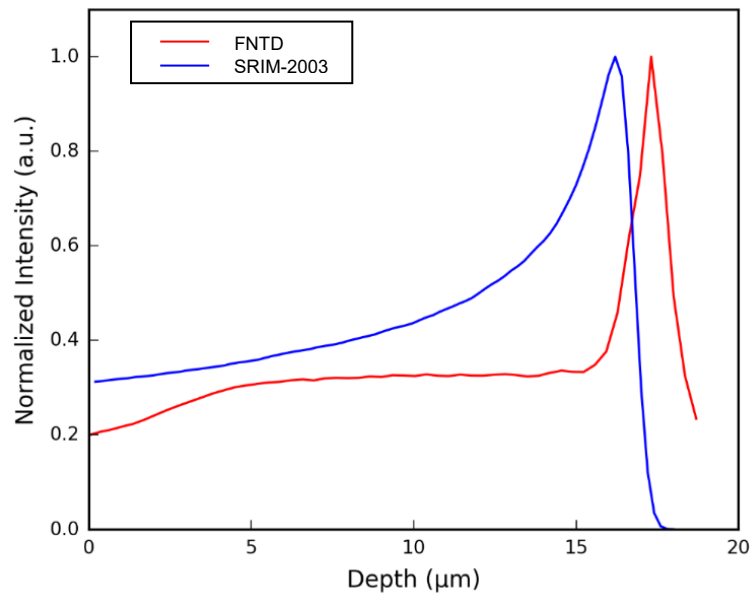


Fig. 11. Comparison of track amplitude as a function of depth in FNTD (red curve) and the Bragg curve calculated using SRIM-2003 and normalized to the measured intensity max value (blue curve) for 1.5 MeV proton.

I.3. Single track spot sizes as function of particle LETs

As the single-track irradiations were tested for 2 types of charged-particles and 2 energies, we investigated the variation of the single spot size as function of the particles LETs. The spot sizes (FWHM in μm) were averaged over 15 spots and are shown in Fig. 12. The uncertainties on the track length due to the choice of the first stack slice are represented in the LET error bars. For protons, the spot sizes increase with the LET values (negligible uncertainties). For α -particles, the spot sizes variations as function of the LET don't have the same behavior. The highest LET value corresponding to 1.5 MeV α -particle have smaller spot size. In fact, the track length of 1.5 MeV α -particles in the FNTD is so short and induce a large LET error bar value at first microns depth, thus the choice of the stack slice where the FWHM were measured may be inaccurate.

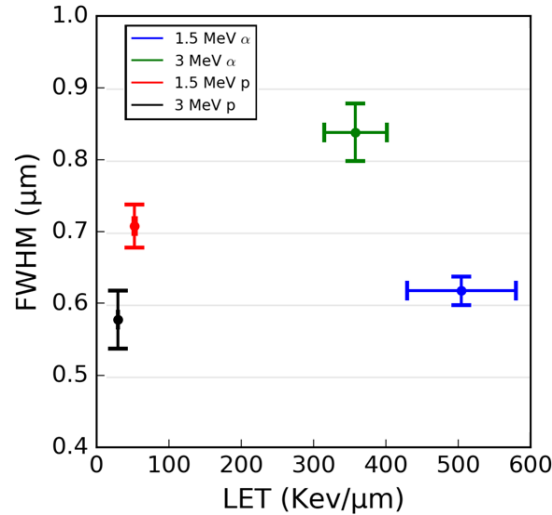


Fig. 12. FWHM mean values measured for single tracks with the FNTD as function of the LET of the incident particle.

II. FNTD intensity response as function of delivered dose

To establish a relation between the numbers of delivered particles (dose) and the intensity of the fluorescent spot and to measure the microbeam size, patterns with an increasing number of particles (Fig. 13.a) were used for the irradiations. Image acquisitions using the CLSM after irradiation with the patterns are presented in Fig. 13.b and Fig. 13.(c&d) for 3 MeV α -particles and protons respectively. For α -particles, the full pattern was acquired in one image. For protons the pattern didn't fit into one image acquisition and it was splitted into two images with different microscope parameters since the high and low doses don't have the

same dynamic range of the fluorescent. For this reason, the column of 14 protons per point was acquired in the 2 images as reference for the intensity values to allow the comparison of the spot intensities.

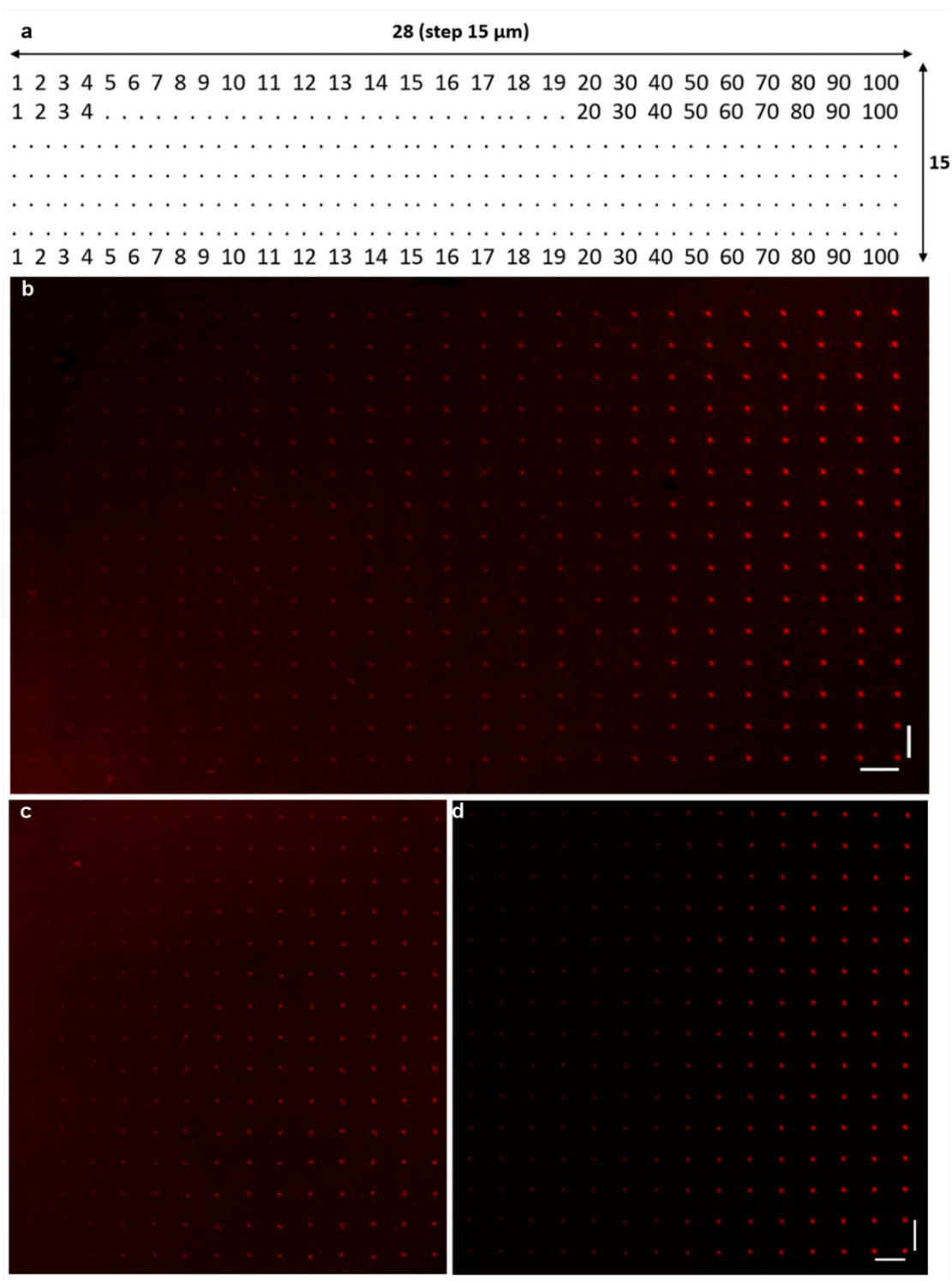


Fig. 13. (a) Scheme of the pattern used for the irradiation of the FNTD with an increasing number of particles repeated 15 times at the AIFIRA microbeam. Microscopic image acquisition using CLSM of the FNTD after irradiations with (b) 3 MeV α -particles and (c, d) 3 MeV protons. Scale bar = 15 μm .

The intensities and the FWHM of each spot were extracted from data measured using ImageJ and then fitted with a Gaussian function using Python. The intensity for each dose is calculated as the mean intensity of the 15 values of each column. Fig. 14 shows the experimental data of the relative intensity with respect to the intensity of a single particle impact as function of the dose in terms of number of delivered (a) α -particles and (b) protons.

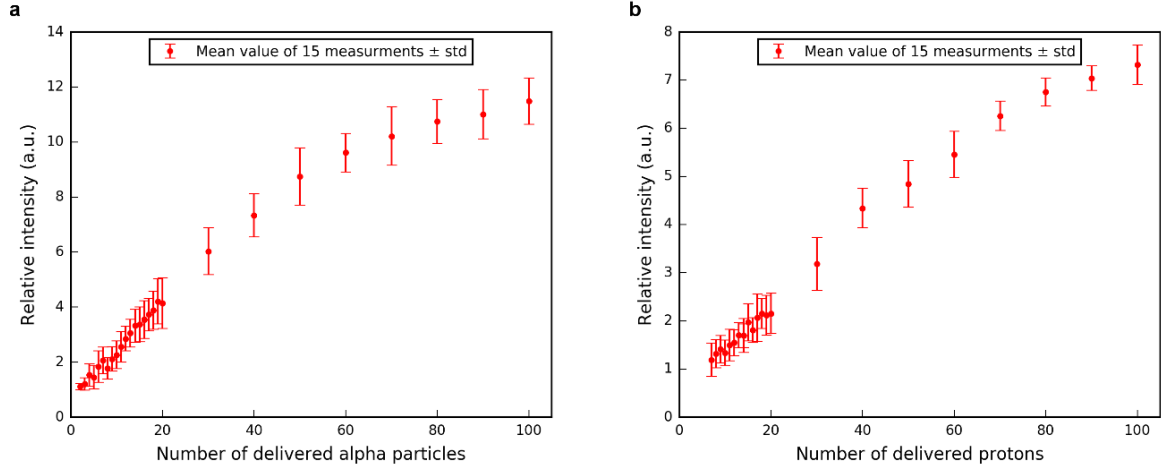


Fig. 14. The mean relative intensity of the measured spots as function of the number of delivered (a) α -particles and (b) protons.

The particle spot intensity determination assumes that the detector shows a linear response up to fifty particles and tends towards an exponential above it. The relative intensity curves reveal a non-linear response of the detectors. The fluorescence intensity seems to saturate for doses above 50 α -particles and 60 protons. The quantitative measurements of the microbeam size (FWHM) can be sensitive to this saturation effects.

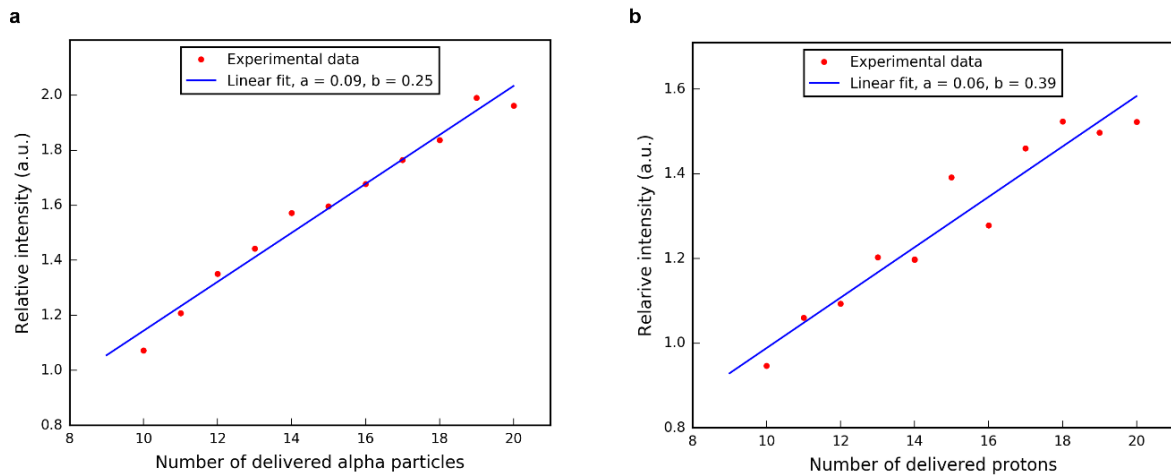


Fig. 15. The mean relative intensity of the measured spots as function of the number of delivered particles from (a) 10 to 20 α -particles and (b) 10 to 20 protons, fitted with a linear function $I \text{ (a.u.)} = a \cdot n + b$.

For the measurement of the microbeam size, only the number of delivered particles from 10 to 20 where the relative intensity was considered. In this interval, the intensity of the fluorescent spots increases linearly with the number of delivered particles (Fig. 15).

The linear fit shows that one α -particle increases the fluorescent intensity by 9% while one proton increases it by 6%.

III. Beam size measurement

The beam size was measured using the data from fluorescent spots after delivering 10 to 20 particles per spot deconvoluted from the detector response to one particle using:

$$FWHM_{microbeam} = \sqrt{FWHM_{measured}^2 - FWHM_{single\ track}^2} \quad (3)$$

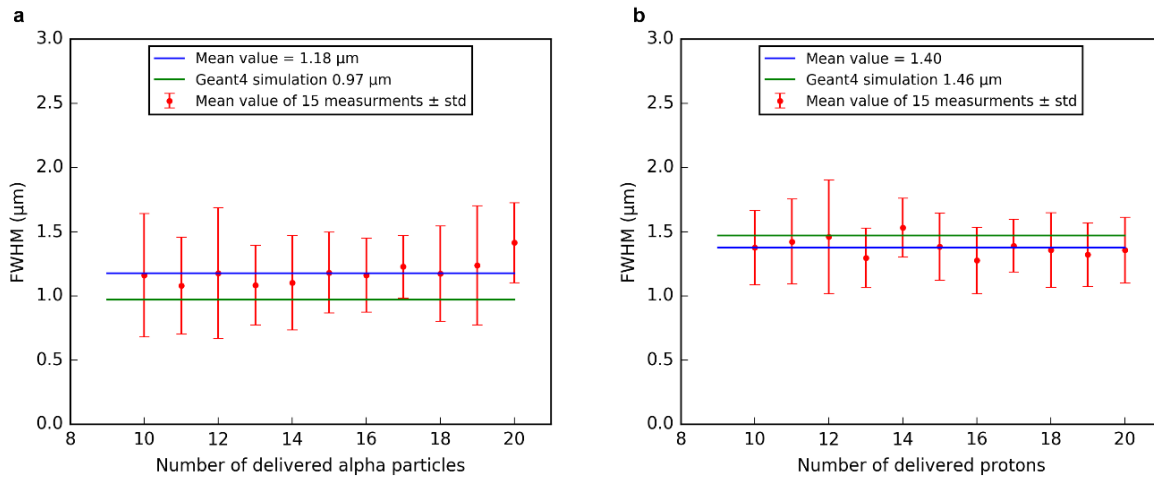


Fig. 16. Microbeam size measurements deconvoluted from the detector response of 1 particle as a function of the number of delivered particles from (a) 10 to 20 3 MeV α -particles and (b) 10 to 20 3 MeV protons. The mean FWHM measured value is $1.18 \pm 0.37 \mu\text{m}$ after irradiation with α -articles and $1.40 \pm 0.27 \mu\text{m}$ after irradiation with protons. These values are similar to the Geant4 simulation results with $0.97 \mu\text{m}$ for α -particles and $1.46 \mu\text{m}$ for protons.

The beam size averaged over 15 spot measurements for each number of delivered particles between 10 and 20 are shown in Fig. 16. After irradiations with α -particles the mean value of the beam size is $1.18 \mu\text{m}$ and after irradiations with protons the mean value of the beam size is $1.40 \mu\text{m}$. These measurements of the beam size are comparable to the Geant4 simulation values of $0.97 \mu\text{m}$ for α -particles and $1.46 \mu\text{m}$ for protons, and to measured values in biological cells¹⁰ of approximately $1.5 \mu\text{m}$.

Discussion

Nuclear track detectors present interesting features for quality assurance in microbeam cell irradiation. This type of detectors is used since many years to validate the beam spot size and the positioning accuracy at the micrometer scale. As they provide a clear visualization of single particle tracks, they are also widely used to validate the dose delivery in terms of number of traversals.

In this study, we investigated the use of FNTDs to measure the characteristics of the CPM at the AIFIRA facility. Compared to the common CR39 nuclear track detector, FNTDs present interesting features such as a high spatial resolution, wide dynamic range of ED measurements, three-dimensional particle information, do not require chemical treatment for the read-out, and the measurements depend only on the irradiations.

Single tracks of MeV protons and α -particles are unambiguously detected, and the size of the fluorescent spot is below one micrometer. To this respect, FNTDs are more efficient than CR39 for which single proton tracks are difficult to distinguish.

Moreover, by deconvoluting the detector response to a single particle and the response to several particles, it was possible to measure precisely the microbeam spot size in air. This could be achieved by delivering 10 to 20 particles per spot to avoid the response non-linearity at higher doses. The value obtained using this approach ($1.18 \pm 0.37 \mu\text{m}$ for α -articles and $1.40 \pm 0.27 \mu\text{m}$ for protons) is consistent with Monte Carlo simulations and the use of FNTDs is to date the most reliable approach for measuring the beam spot size. The measured microbeam size is different for the 2 types of particles due to the difference in thickness of the diamond detector placed at the microbeam exit before reaching the FNTD.

Above 50 delivered particles, the detector intensity response presents nonlinearity as function of the delivered number of particles, showing intensity saturation. The saturation of the fluorescent spots may be due to the limited number of color centers available in the actual track core where very high energy densities can occur^{16,26}.

In addition to the spatial information about the particle delivery, the fluorescence intensity was investigated to check whether this parameter could be related to physical parameters such as LET, energy and range.

The values obtained for the track lengths are in most cases overestimated by 1 to 2 μm compared to SRIM simulations. This discrepancy is mainly due to the inaccuracy in determining the exact position of the FNTD surface on CLSM images. Indeed, the polished

surface cannot be unambiguously distinguished on such images. For more accurate measurement, this limitation could be solved by marking the polished surface of the detector with a reference mark as described in ²⁶.

According to the measurement of the single-track spot sizes, it is difficult to relate the FWHM of these spots with the particle LET. In some cases, the FWHM seems to increase with the LET, which is in agreement with other studies^{16,26}. Nevertheless, it is not the case for all measured conditions and especially for the highest LET value (1.5 MeV α -particles). This interesting property of the FNTD response to charged-particles does not seem to be preserved for particles presenting a very short range in the detector.

Apart from this limitation, the results reported in this preliminary study shows that the FNTD provides a reliable technique to characterize precisely the CPM at the AIFIRA facility.

References

1. Rozenfeld, A. B. Novel detectors for silicon based microdosimetry, their concepts and applications. *Nucl. Instruments Methods Phys. Res. Sect. A Accel. Spectrometers, Detect. Assoc. Equip.* **809**, 156–170 (2016).
2. Zahradnik, I. A. *et al.* scCVD Diamond Membrane based Microdosimeter for Hadron Therapy. *Phys. Status Solidi Appl. Mater. Sci.* **215**, 1–10 (2018).
3. Yokota, Y. *et al.* Development of an ion microbeam system for irradiating single plant cell[s]. *Biol Sci Sp.* **17**, 298–301 (2003).
4. AHN GIL HOON;LEE JAI-KI. CONSTRUCTION OF AN ENVIRONMENTAL RADON MONITORING SYSTEM USING CR-39 NUCLEAR TRACK DETECTORS. *Nucl. Eng. Technol.* **37**, 395–400 (2005).
5. Horwacik, T., Bilski, P., Olko, P., Spurny, F. & Turek, K. Investigations of doses on board commercial passenger aircraft using CR-39 and thermoluminescent detectors. *Radiat. Prot. Dosimetry* **110**, 377–380 (2004).
6. Yoon, M. *et al.* Radiation-induced cancers from modern radiotherapy techniques: Intensity-modulated radiotherapy versus proton therapy. *Int. J. Radiat. Oncol. Biol. Phys.* **77**, 1477–1485 (2010).
7. Peng, S. *et al.* Measurements of the targeting accuracy of the Gray Laboratory charged-particle microbeam. *Nucl. Instruments Methods Phys. Res. Sect. B Beam Interact. with Mater. Atoms* **179**, 145–150 (2001).
8. Heiss, M. *et al.* Targeted irradiation of Mammalian cells using a heavy-ion microprobe. *Radiat. Res.* **165**, 231–9 (2006).
9. Bourret, S. *et al.* Fluorescence time-lapse imaging of single cells targeted with a focused scanning charged-particle microbeam. *Nucl. Instruments Methods Phys. Res. Sect. B Beam Interact. with Mater. Atoms* **325**, 27–34 (2014).
10. Muggiolu, G. *et al.* Single α -particle irradiation permits real-time visualization of RNF8 accumulation at DNA damaged sites. *Sci. Rep.* **7**, 41764 (2017).
11. Akselrod, M. S., Akselrod, A. E., Orlov, S. S., Sanyal, S. & Underwood, T. H. New

- aluminum oxide single crystals for volumetric optical data storage. *Opt. Data Storage* **2003** **5069**, 244 (2003).
12. Akselrod, M. S., Yoder, R. C. & Akselrod, G. M. Confocal fluorescent imaging of tracks from heavy charged particles utilising new Al₂O₃:C,Mg crystals. *Radiat. Prot. Dosimetry* **119**, 357–362 (2006).
13. Akselrod, M. S. & Akselrod, A. E. New Al₂O₃:C,Mg crystals for radiophotoluminescent dosimetry and optical imaging. *Radiat. Prot. Dosimetry* **119**, 218–221 (2006).
14. Niklas, M. *et al.* Ion track reconstruction in 3D using alumina-based fluorescent nuclear track detectors. *Phys. Med. Biol.* **58**, (2013).
15. Greulich, S. *et al.* Fluorescent nuclear track detectors as a tool for ion-beam therapy research. *Radiat. Meas.* **56**, 267–272 (2013).
16. Osinga, J. *et al.* High-accuracy fluence determination in ion beams using fluorescent nuclear track detectors. **56**, 294–298 (2013).
17. Akselrod, M. S. & Sykora, G. J. Fluorescent nuclear track detector technology - A new way to do passive solid state dosimetry. *Radiat. Meas.* **46**, 1671–1679 (2011).
18. Akselrod, G. M., Akselrod, M. S., Benton, E. R. & Yasuda, N. A novel Al₂O₃ fluorescent nuclear track detector for heavy charged particles and neutrons. *Nucl. Instruments Methods Phys. Res. Sect. B Beam Interact. with Mater. Atoms* **247**, 295–306 (2006).
19. Niklas, M. *et al.* Spatial correlation between traversal and cellular response in ion radiotherapy - Towards single track spectroscopy. *Radiat. Meas.* **56**, 285–289 (2013).
20. Bartz, J. A., Kodaira, S., Kurano, M., Yasuda, N. & Akselrod, M. S. High resolution charge spectroscopy of heavy ions with FNTD technology. *Nucl. Instruments Methods Phys. Res. Sect. B Beam Interact. with Mater. Atoms* **335**, 24–30 (2014).
21. Bartz, J. A., Zeissler, C. J., Fomenko, V. V. & Akselrod, M. S. An imaging spectrometer based on high resolution microscopy of fluorescent aluminum oxide crystal detectors. *Radiat. Meas.* **56**, 273–276 (2013).
22. Greulich, S., Ulrich, L., Kouwenberg, J. J. M. & Rahmanian, S. Measurement of

- fluence, LET, and dose in a carbon ion spread-out Bragg-peak using fluorescent nuclear track detectors and an automated reader. 1–21 (2017). at <<https://arxiv.org/ftp/arxiv/papers/1610/1610.05054.pdf>>
23. Greubel, C. *et al.* Low LET proton microbeam to understand high-LET RBE by shaping spatial dose distribution. *Nucl. Instruments Methods Phys. Res. Sect. B Beam Interact. with Mater. Atoms* **404**, 155–161 (2017).
 24. Barberet, P. *et al.* Cell micro-irradiation with MeV protons counted by an ultra-thin diamond membrane. *Appl. Phys. Lett.* **111**, 243701 (2017).
 25. Ziegler, J. F. & Biersack, J. P. in 93–129 (Springer US, 1985).
 26. Osinga, J. M. Fluorescent Nuclear Track Detectors: High-Accuracy Fluence Determination in Ion Beams. (Faculty of Natural Sciences II - Chemistry, Physics and Mathematics, Heidelberg, 2012).

PART II

**Kinetic study of detection and repair of DNA
damage proteins after irradiations at
cellular scale**

Introduction

To study radiation-induced DNA repair mechanisms, charged-particle beams have been used to generate extremely localized DNA damage along the particle tracks. Combined with the development of fluorescent protein marker techniques and to time lapse imaging, these systems have been used to study the dynamics of DNA repair proteins. Such systems have been set up, firstly on the beamline at GSI^{1,2}. Using the GSI irradiation beamline, Tobias *et al.* studied the recruitment and binding kinetics of early damage response NBS1, MDC1 and 53BP1 proteins at increasing lesions clustering (C- and V-ion irradiation). They have shown that the recruitment of the NBS1 and MDC1 proteins accelerate with increasing lesion density. 53BP1 recruitment was found to be almost identical for the 2 ion types indicating that it is independent of LET³.

In the last decade, the use of CPMs have been extended to study the *in vitro* kinetics of proteins response involved in different DNA damage signaling and repair pathways⁴. Indeed, microbeams present unique features to perform this type of measurements:

- A micrometer precision for targeting cellular or subcellular compartments.
- The delivery of a precise number of particles per cell down to a single particle.
- The choice of different particle types and energies allowing to cover a wide range of LETs. This parameter is of particular importance for studying the impact of clustered or complex damage.
- The irradiation following geometrical patterns.
- Their easy coupling to beamline microscopy to visualize the accumulation of GFP-tagged proteins in living cells expressing immediately after irradiation.

The combination of all these features opens the possibility to investigate the protein dynamics as a function of their role, time, delivered dose and particle LETs. A few research groups worldwide have used CPM combined to time-lapse imaging to study radiation-induced DNA repair mechanisms. At the PTB microbeam, Mosconi *et al.* studied and compared the kinetic formation of 53BP1 and MDC1 after irradiation with α -particles or protons. It has been shown that, with both high TEL and low TEL particles, the generated foci 53BP1 and MDC1 are of similar size, with a slight difference in kinetics depending on the type of particle. They showed in all cases the presence of time lags between the recruitment of MDC1 and that of 53BP1, confirming the hierarchical nature of these two proteins.⁵ Hable *et al.* studied the recruitment kinetics of MDC1, 53BP1 and RAD52 proteins after micro-irradiation with two

type ions (carbon ions and protons) having different LETs and inducing different types of DNA damage. Using the microbeam facility SNAKE⁶, they have shown that the recruitments of MDC1 and RAD52 proteins depend on the complexity of the damage generated, which is not the case for 53BP1⁷.

Apart from studying DNA repair mechanisms, the combination of fluorescence time lapse imaging with microbeam irradiation provides the opportunity to visualize the cell early response to localized DNA damage in the first seconds/minutes post-irradiation. The correlation of the response dynamics with the damage complexity can provide useful information on the impact of the physical parameters of the irradiation on the nature of the radiation-induced DNA damage.

The properties of radiation tracks and microdosimetric quantities can be characterized using specific Monte Carlo codes, referred to track structure codes. Track structure codes allow to calculate the ED at the DNA scale by modeling particle tracks “step-by-step” and predict the number of different types of DNA damage. This is in particular the case of Geant4-DNA that provides dedicated tools for investigating such effects in open access^{8,9,10}.

The dosimetry associated to cell micro-irradiation with charged-particles raises a number of challenging questions:

- What is the number of the different type of DNA lesions?
- What is the spatial distribution of the DNA lesions?
- How do these parameters relate to the particles LET?
- Is the damage complexity influenced by the beam focusing and the potential overlap of single tracks?
- How to consider the clustering of the DNA damage at the ion track scale (nm) and the chromatin sub-structure scale (μm)?

In this study, the AIFIRA CPM was used to micro-irradiate single cell nuclei from 2 different cell lines expressing GFP-tagged DNA repair proteins and measure the kinetics of the DNA damage response of these proteins. Irradiations were performed with α -particles and protons having LETs of 12 keV.μm⁻¹ and 140 keV.μm⁻¹ respectively. The first protein, XRCC1, is known as essential scaffold protein, recruited immediately after irradiation and involved in DNA SSBs repair^{11–13}. The second protein is RNF8, a ring-finger ubiquitin ligase and one of the first proteins rapidly recruited at DNA DSBs^{14,15}. These two proteins were chosen for their fast accumulation at damage sites which allows the visualization of the early response after

irradiations and because they are involved in the repair of different types of DNA lesions (SSB and DSB).

In the following, I will present the experimental methodology to micro-irradiate cell nuclei of the 2 cell lines and to follow the accumulation of XRCC1 and RNF8 proteins at the damage sites. The measurement of the fluorescent intensity and the recruitment time for various physical parameters (LETs and doses) will be given. Then, a detailed description of my contribution for this study to develop the microdosimetry modeling of these irradiations using the toolkit Geant4-DNA will be presented. It consists on simulating the energy distribution deposited by the 2 charged-particles in a cell nucleus and to predict the different type and amount of DNA damage induced after the different irradiation conditions at the nanometric and micrometric scales.

Methods

I. Experimental cellular micro-irradiation using CPM

I.1. Cell lines expressing GFP-XRCC1 and GFP-RNF8 proteins

The GFP-expressing cells are widely used to monitor genes expression and proteins localization in living cell¹⁶. For this study, two cell lines expressing GFP-tagged proteins involved in different DNA repair pathways have been developed previously¹⁷. The selected protein are GFP-XRCC1¹⁸ and GFP-RNF8¹⁹.

- **GFP-XRCC1 protein: Base Excision and Single Strand Break Repair**

DNA single-strand breaks (SSB) are one of the most frequent DNA lesions produced by endogenous reactive oxygen species or generated by IR or through base hydrolysis²⁰. This lesion can be defined as a nick in the sugar-phosphate backbone of one strand of the DNA double helix. The base excision repair (BER) is the repair pathway for SSBs²¹. When SSB occurs, one of the first events induced to bind it is the activation of the enzyme poly (ADP-ribose) polymerase-1 (PARP-1). A critical component of SSB repair recruited by PARP-1 is the protein XRCC1. It is an essential scaffold protein required for the coordination of different repair pathways and associated with SSB Repair (SSBR) pathway²²⁻²⁴. XRCC1 is considered to act as a central loading platform in SSB repair, which plays the role of a matchmaker for recruitment of other proteins involved in SSB repair^{25,26}.

- **GFP-RNF8 protein: Double Strand Break Repair**

Double strand breaks (DSBs) are the most lethal lesions since they can cause cell death if unrepaired and, they can result in the etiology of carcinogenesis if misrepaired²⁷. This lesion can be defined as a rupture in the double stranded of DNA molecule disrupting the sugar-phosphate backbone on both strands at sites located directly opposite each other and just a few nucleotides apart (up to ~10 bp). There is two major pathways to repair DSBs, which differ in the fidelity and template requirement: non-homologous end joining (NHEJ)²⁸ or homologous recombination (HR)²⁹. NHEJ modifies the broken DNA ends and ligates them together using Ku protein without regard for any homologous template generating deletions or insertions. In contrast, HR uses an undamaged homologous

sequence of DNA template to repair the break, leading to the reconstitution of the original sequence. When DSBs occurs, the ATM (ataxia telangiectasia mutated) protein is recruited and activated. A very early step in the cellular response to DSBs is the phosphorylation of the histone H2AX by the ATM resulting in discrete γ -H2AX (phosphorylated-H2AX) foci at the DNA damage sites (4). This phosphorylation generates binding sites for adaptor proteins such as RNF8. RNF8 is among the first proteins to accumulate at the DSBs sites. RNF8, acting as an ubiquitin ligase to tether DNA repair molecules at DNA lesions in HR pathway^{30–32}.

I.2. Cells micro-irradiation and time lapse imaging

The GFP-XRCC1 and GFP-RNF8 cells were plated in the dedicated microbeam cell dish³³. During irradiation and time-lapse imaging, the cells were maintained in FluoroBrite™ DMEM medium (GIBCO, ThermoFisher Scientific) to ensure a low fluorescence background. The cell culture well is mounted in vertical position on the microbeam line as shown in Fig.17.

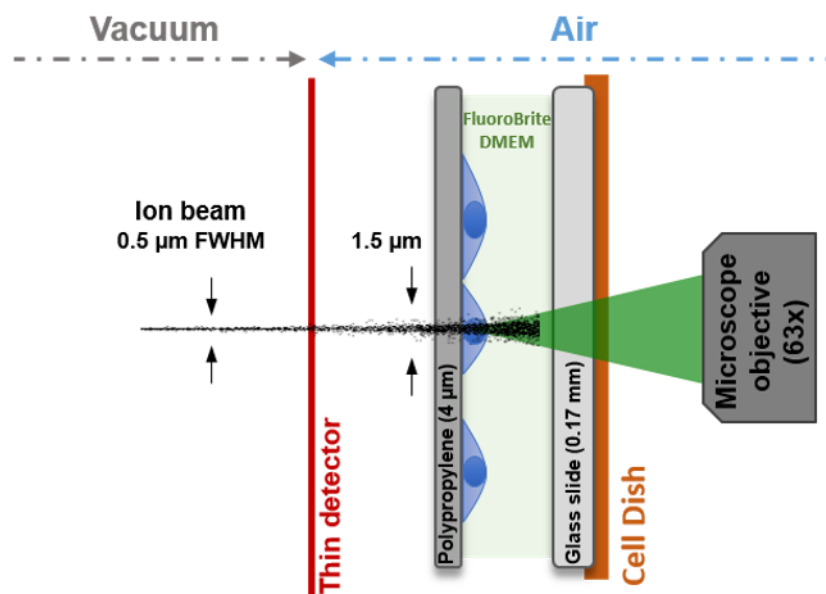


Fig. 17. Scheme of the irradiation end-station. The cells adhere on a 4 μm-thick polypropylene foil and are maintained vertically. The nucleus of each cell is targeted with 3 MeV protons or α -particles. The microbeam is extracted through a diamond detector or Si_3N_4 window. The irradiated cell nuclei were then followed using online fluorescence microscopy.

Cell nuclei were targeted with increasing numbers of 3 MeV protons or α -particles from 1 to several thousands of particles per cell. In the case of α -particle irradiation the exact number of delivered particles was detected upstream the sample with a BNCD-coated extraction window coupled to a channeltron electron multiplier. In the case of protons, the number of delivered ions N was chosen by adjusting the beam opening time leading to a statistical fluctuation of \sqrt{N} . The proteins re-localization at the damaged sites was followed for 30 min using the inverted fluorescent microscope equipped with a 63x objective (LD Plan-Neofluar 63x/0.75, Optical resolution of about 400 nm, Carl Zeiss MicroImaging GmbH) and a 14 bits Rolera EM-C²™ Camera (QImaging) positioned horizontally at the end of the beam line.

I.3. Fluorescent images treatment and data fitting models

The fluorescence images were treated using the ImageJ software (<http://rsbweb.nih.gov/ij/>). The fluorescence intensity was measured in a region of interest (ROI) delimiting the irradiated areas. This intensity was corrected by subtracting the background intensity. Photo bleaching was corrected using the fluorescence signal of non-irradiated cells present in each image. The fluorescent intensity increase relative to the initial value before irradiation was then fitted using mathematical models to access relevant parameters: the recruitment time T (s) and the amplitude of the intensity A (u.a.).

For the GFP-RNF8 protein, the fluorescent intensity distribution was fitted using a first order step response as described in Luka *et al.*³⁴:

$$I_{rel} = 1 + A \left(1 - e^{\frac{(t-t_0)}{T}} \right) \quad (1)$$

T (s) represents the mean recruitment time of the protein at the damage site. A (a.u.) represents the highest fluorescent intensity value. t_0 is the irradiation time relative to the beginning of the video.

For the GFP-XRCC1 protein, the fluorescent intensity distribution was fitted using the model used by Hable *et al.*⁷:

$$I_{rel} = 1 + A \left(1 - e^{\frac{(t-t_0)}{T}} \right) * e^{\frac{(t-t_0)}{T_2}} \quad (2)$$

The first part of the function is the same as the one used previously, as well as the T , A and t_0 parameters. However, the intensity decreases over longer periods and it is described by the second part of the function. The parameter T_2 (s) represent the mean decay time when the fluorescent intensity decreases as already done in other studies^{7,11}.

All these parameters are determined for each cell separately, and then a statistical distribution in the form of box plot is calculated for each irradiation condition (type and number of delivered charged-particles).

II. Microdosimetry of the cellular ion microbeam irradiations

When targeting biological cells with a CPM, the charged-particles interact with these cells in a sequence of complex events that can be separated in 4 consecutive temporal stages: physical, physicochemical, chemical and biological stages. For this study, my efforts were dedicated to develop the physical stage from the calculation of the ED to the prediction of the number of different DNA damage using the Geant4-DNA version of the toolkit Geant4^{35, 36}. It will include only the direct DNA damage. The indirect damage corresponding to the physicochemical stage is not included since its calculation requires a real DNA structure not available in the current Geant4-DNA version.

II.1. Simulation of track structures and energy distributions

First, the track structures of one α -particle and one proton having 2 different LETs were simulated in a cell nucleus using the same experimental irradiation conditions. For these calculations, the cell nucleus was modeled with a homogeneous water cube of 6 μm side corresponding to the average thickness of a human nucleus cell. Since the calculation in Geant4-DNA takes place in liquid water, the ion beam was delivered at the entry of the water cube volume. To consider all the material traversed by the ions, the microbeam was modeled as a Gaussian beam with FWHM of 1.5 μm and mono-energetic with energy 3 MeV for protons and of 2.5 MeV for α -particle taking into account the energy loss before reaching the target. A Geant4-DNA Physics list based on the recommended “G4EmDNAPhysics_option4” constructor was used³⁷. The Geant4-DNA processes are all step-by step processes; as such, they simulate explicitly all the physical interactions of ionizing particles in the irradiated medium and do not use any production cut-off.

For each physical interaction, the ED, the particle position and the interaction name were recorded. The 3D track structure of α particles and protons were reconstructed using the dataset that considers the physical interactions having non-zero ED (nuclear scattering, electronic excitation, ionization, and charge exchange) as shown in Fig. 18.

The energy distribution for the different irradiation conditions will be presented with 2D histogram projected along the z-axis (the volume depth) with a binning of $0.2 \times 0.2 \mu\text{m}^2$ similar to the pixel size of the microscope fluorescent images.

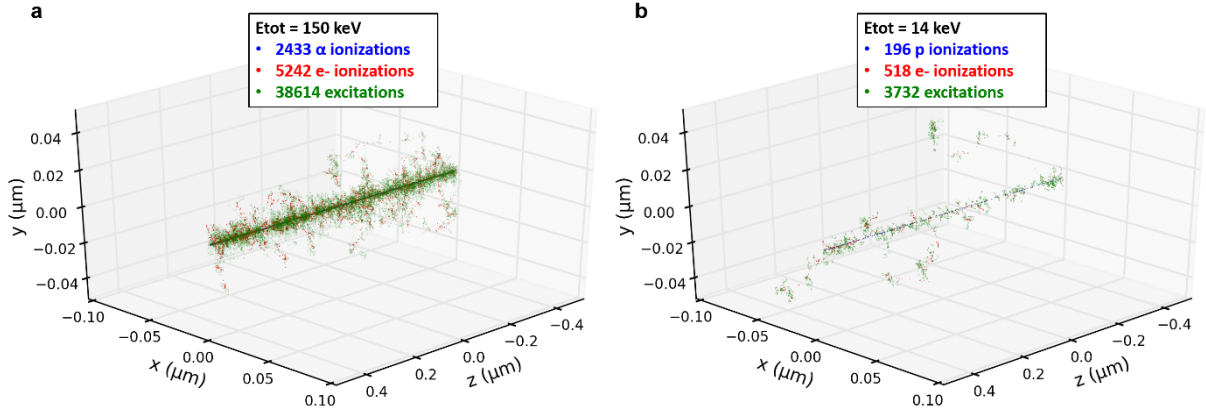


Fig. 18. Track structure simulation of single 3 MeV α -particle/proton in 1 μm water. When (a) one α -particle and (b) one proton traverse 1 μm of liquid water, the density of physical interactions (ionizations and excitations) and the ED is 10 times higher for α -particle than for proton, due to the α -particle's higher LET.

II.2. Clustering of DNA damage

II.2.1. Calculation of the induction of Strand breaks

The position and the EDs of the physical interaction can be used to predict DNA stand breaks (SBs) induced after the different irradiation conditions. Strand breaks have been assumed to occur by defining 3 parameters.

- A uniform probability that defines if an interaction is situated in a sensitive zone or not (SPointsProb). The sensitive location is composed of a volume containing the DNA double helix plus a virtual aura surrounding it. I chose a SPointsProb value of 0.2 as the value used by Bernal *et al.*³⁸.
- To take into account that not all interactions induce DNA SB, a probability of damage induction is defined as a linear function increasing with the value of the ED. I used a function similar to that used by Friedland *et al.* with a linear probability of damage induction increases from zero at EMinDamage = 5 eV to 1 at EMaxDamage = 37.5 eV (Fig. 19)³⁹.

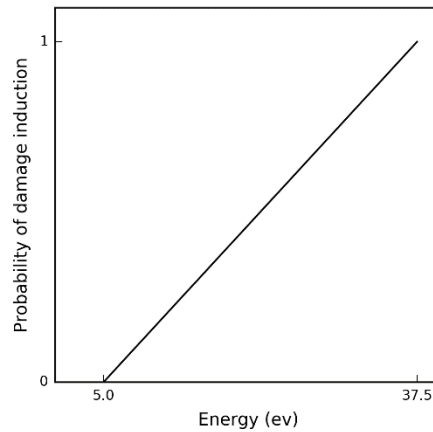


Fig. 19. The probability of DNA damage induction. It is a linear function varying from 0 to 1 for a ED between 5 ev to 37.5 ev.

II.2.2. Clustering of DNA damage

Based on the “Clustering” example of Geant4-DNA, the number and the position of DNA SBs can be calculated and then clustered into 3 types of DNA damage (SSBs, DSBs and CSBs). The “Clustering” example of Geant4-DNA is based on the DBSCAN (Density Base Spatial Clustering of Applications with Noise) algorithm that relies on density-base notion of clusters and groups points that are closely packed together in the space to form clusters of arbitrary shapes (Fig. 20). Density-based clusters are dense areas in the data space separated from each other by sparser areas⁴⁰. The DBSCAN algorithm uses two main parameters for data clustering: the minimum number of points to form a cluster (MinPts) and the maximum distance between 2 points to form a cluster (esp).

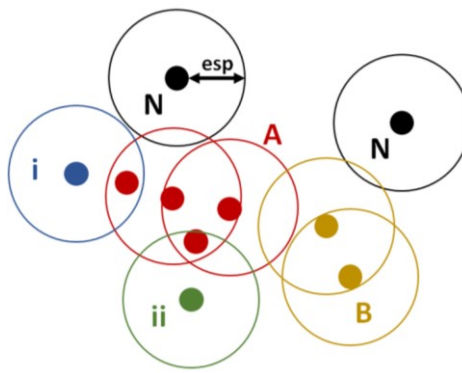


Fig. 20. Diagram of the DBSCAN data clustering algorithm concept. The 2 required parameters of DBSCAN for this diagram are the minimum number of point to form a cluster setted to 2 and the maximum distance between 2 points to be considered in the same cluster setted to esp. The red points and the yellow points are core points of 2 separated clusters (A and B), since these points are within an esp radius area containing at least 2 points. The points i and ii are not core points but they are reachable from A (via other core points) and thus belong to the cluster A as well. The points N are noise points that are neither core points nor directly reachable.

To perform the simulations for the different irradiation conditions using this Geant4-DNA example, the MinPts number was set to 2 since the induction of DSB takes at least 2 SSBs (2 points). For the maximum distance between 2 points, an eps value of 3.4 nm which corresponds to 10 base pairs was chosen^{8,38,41}.

Beside the definition of the “Clustering” parameters, I modified the code to calculate the damage numbers at the end of the run for the contribution of all the tracks together and not track by track. This could help also to test if there is a focusing effect of the microbeam at the micron scale (1.5 μm) where tracks can overlap and influence the damage complexity and change the proportion of each DNA damage type. The clustering example outputs are the 3 types of DNA damage and their size in term of number of damage grouped in the same cluster.

- SSBs (Single Strand Breaks): correspond to a localized interaction in a sensitive location and having an energy verifying the probability of damage induction. This type of damage corresponds to noise points in the DBSCAN algorithm that does not belong to a cluster.
- DSBs (Double Strand Breaks): correspond to clusters formed of 2 SSBs of less than esp, of which at least 1 is located on an opposite strand. To determine on which strand is located the SSB, each SSBs have a flag value either 0 or 1 corresponding to the first strand if it is touched or the second strand.
- CSBs (Complex Strand Breaks): correspond to clusters formed of more than 2 SSBs that are distant by less than esp.

II.3. DSBs clustering at the micron scale

Apart from the number of each DNA damage, I added to the output data of the clustering example the 3 DNA damage positions allowing the visualization of their spatial distribution within the cell nucleus volume (water cube). These positions allow damage clustering at different level other than the basic DNA damage at the nanometer scale. The micrometer scale is often associated to a higher severity of the induced damage, and thus to a prolonged persistence and enhanced lethality. At the micron scale the DNA damage can interact with

further proximate bps distance or other DNA damage such as DSB-DSB interaction revealing more complex damage^{42,43}. To compare the behavior of the DNA-repair proteins for the 2 types of particles especially for GFP-RNF8 involved in DSBs, it is important to investigate such interactions.

Since the modified “Clustering” code of Geant4-DNA gives access to the position of the DNA damage (DSBs) in 3D dimensional space the DSBs spatial distribution was investigated at the micron scale by clustering these damage within chromatin loops (30 nm) of the DNA fiber using the DBSCAN method from the Scikit-learn library in python. The inputs for this method are the positions (x, y, z) of each DSB, the minimum number of DSBs to form a cluster, and the maximum distance between 2 DSBs to be considered in the same cluster. A min number of 2 and a max distance of 30 nm corresponding to chromatin loop of the DNA fiber was chosen^{41,42,43}. The clustering of the DSBs at the micron scale was calculated for the 2 LETs of particles, and for the different number of delivered particles. The outputs of the calculation are (i) the number of 2 classes of DSBs namely isolated DSBs (iDSBs) and clustered DSBs (cDSBs) according to whether one or more than one DSB are simultaneously included in the same cluster respectively, (ii) the barycenter for each cluster, (iii) the clusters size (in term of DSBs number), and (iv) the cluster spatial size using the maximal distance between the 2 DSBs within it.

Results

I. Experimental results

It is known that the DNA damage complexity, i.e. the formation of SSBs or DSBs, increases with particle LETs⁴⁴. The AIFIRA CPM gives the opportunity of delivering controlled number of 3 MeV α -particles and protons having respectively a LET of 148 and 12 keV. μm^{-1} . Therefore, it permits to study the XRCC1 and RNF8 proteins responses dependency with the particle LET and/or its ED.

I.1. Recruitment kinetics of GFP-XRCC1 protein to DNA damage sites after α -particle and proton irradiations

To study the recruitment kinetic of GFP-XRCC1 at DNA damage sites, GFP-XRCC1 cells were irradiated with increasing numbers of α -particles (10, 50, 100 and 1000) and protons (100 ± 10 , 500 ± 22 and 1000 ± 32), then followed using online live cell microscopy. Images were taken before, during, and up to 30 minutes after irradiation. The microscopic acquisitions were then used to measure the intensity of the fluorescent spot corresponding to the accumulation of GFP-XRCC1 during time at the damage site as shown in Fig. 21.a. At $t=0 \text{ min}$, the GFP-XRCC1 protein is distributed homogeneously in the nucleus giving it this homogeneous green color. For all irradiation conditions, the formation of GFP-XRCC1 radiation-induced foci appeared within 10 seconds. The protein recruitment kinetic was quantified using the normalized fluorescence intensity curves as function of time after irradiation (Fig. 21.b). It is characterized by the recruitment time T , the decay time T_2 , and the amplitude of the fluorescent intensity A . These parameters are obtained by fitting the data using equation 2.

The T_2 values presented large data dispersion that can be due to several causes such as the individual capacity of cells to repair damage, the cell cycle position, and the amount of DNA damaged or the GFP-level expression. For these reasons the T_2 parameter is not discussed in this study, but it was used to fit correctly the model function. The results were shown for the recruitment time T and the maximum fluorescent intensity A calculated for at least 16 cell nuclei per irradiation condition (Fig .22).

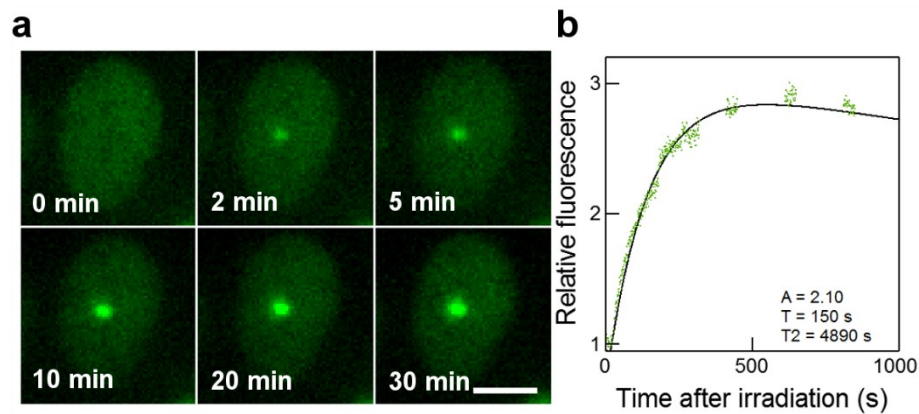


Fig. 21. Real time recruitment of GFP-XRCC1 to the micro-irradiated area. (a) Cell nucleus irradiated with 100 α -particles. The time at which the cell is hit by particles is set as $t = 0$. At $t = 0$ min, the GFP-XRCC1 protein is distributed homogeneously in the nucleus giving it this homogeneous green color. Selected time points, covering the signal of the fluorescent spot corresponding to the accumulation of GFP-XRCC1 at the irradiated site are shown. Scale bar: 10 μ m. (b) Kinetics curve showing the normalized data from the cell nucleus in panel a, fitted using a double-exponential curve and cropped at 15 min. The distribution of the GFP-XRCC1 protein is recorded at 1 s intervals during 300 s, then at 10 min, 15 min et 30 min during 100 s to minimize the GFP photobleaching.

Fig. 22.a shows that T does not vary significantly between 10 and 50 α -particles (p-value of 0.8 with significant level at 5%). This may be due to a weak fluorescent signal or to reaching the detection limit of the system. After irradiations with 50, 100 and 1000 α -particles, the recruitment time decreased significantly as a function of the number of delivered particles (p-value $< 10^{-7}$). In the same manner, a decrease in the mean recruitment time is observed when the number of delivered protons is increased from 100 to 1000 (p-value $< 10^{-5}$). Considering the 2 LETs, T is similar for the same ED by α -particles and protons. For instance, the recruitment time after 10 α -particles and 100 protons is the same (p-value of 0.46), as well as for 50 α -particles and 500 protons (p-value of 0.22), and 100 α -particles and 1000 protons (p-value of 0.15) for which the mean ED is similar (0.9 MeV/ α -particle and 0.7 MeV/proton).

Fig. 22.b shows that A increased significantly as a function of the number of delivered particles following irradiations from 10 to 1000 α -particles (p-value of 0.1) and 100 to 1000 protons (p-value of 0.4). The number of DNA damage increases with the number of delivered particles which will cause an increase of the amount of GFP-XRCC1 protein at the damage site producing greater fluorescent intensity. Comparing the 2 LETs, A is similar for the same ED by α -particles and protons. For instance, A remains the same after irradiations with 10 α -particles and 100 protons (p-value of 0.07), as well as for 50 α -particles and 500 protons (p-value of 0.1).

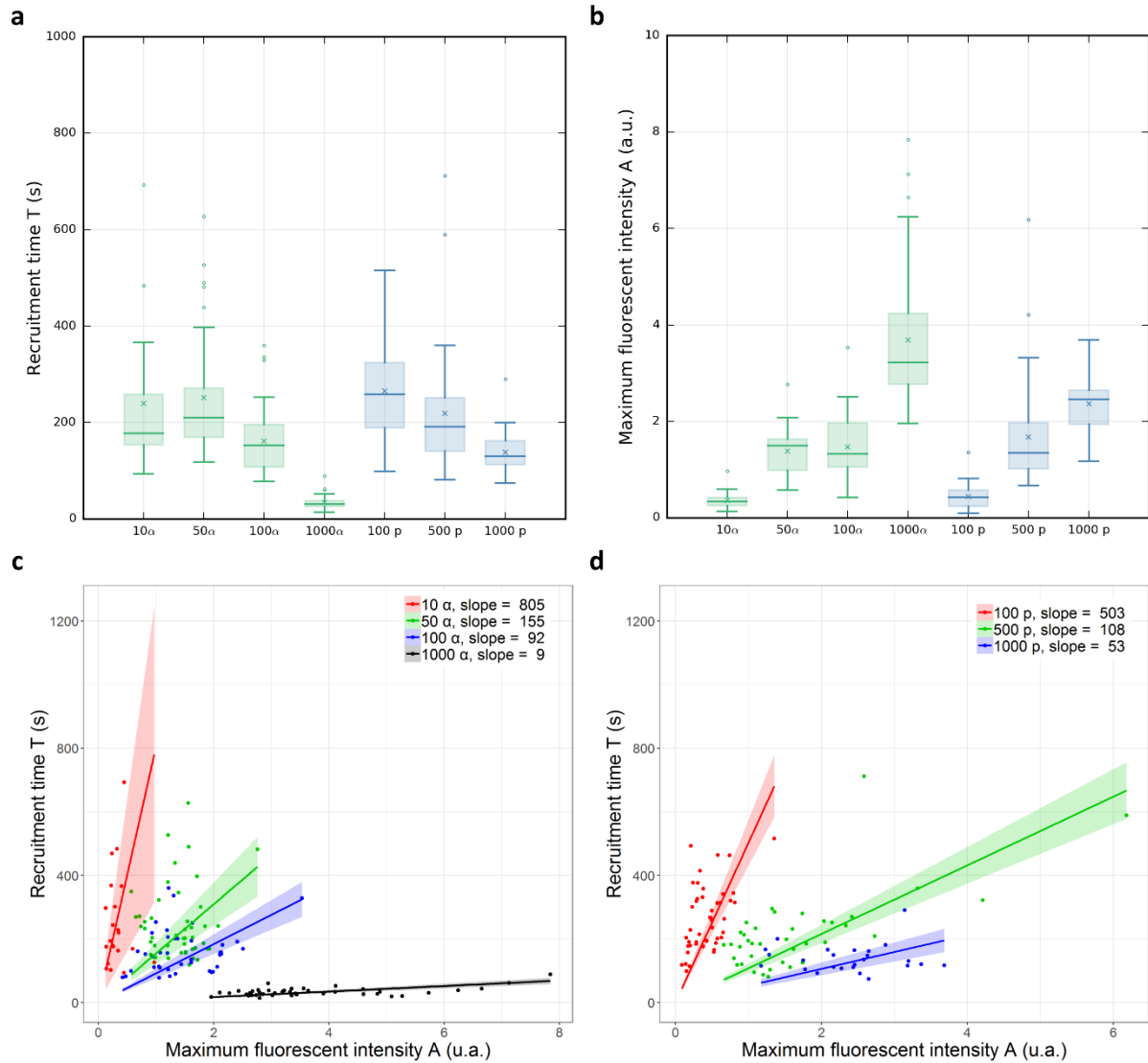


Fig. 22. Mean recruitment time (T) and amplitude of the fluorescent intensity (A) of GFP-XRCC1 after proton and α -particle irradiations. (a) Box plots representing the distribution of recruitment times (T) of GFP-XRCC1 cells after irradiation with increasing numbers of α -particles (green) and protons (blue). T decreases with increasing numbers of delivered particles independently from their type and LET. (b) Box plots representing the amplitude of the GFP-XRCC1 intensity with increasing numbers of α -particles (green) and protons (blue). A increases, indicating that the amount of GFP-XRCC1 also increases with the increasing of the number of delivered particles. Considering the two parameters T and A together for (c) α -particles and (d) protons, T increases while A decreases when the number of delivered particles increases.

Considering the two parameters, Fig. 22.c and Fig. 22.d show that T varies linearly with A for all number of delivered particles. While increasing the number of delivered particles, the recruitment time T decreases and the amplitude of the fluorescent intensity increases in the same manner for the 2 LET values.

I.2. Recruitment kinetics of GFP-RNF8 protein at DNA damage sites after CPM irradiations

Irradiations performed with charged-particles are known to be more effective than photons in damaging biological systems (higher RBE). Their capacity to induce clustered DNA damage, especially DSBs, are the main cause of this greater effectiveness⁴⁵. For this reason, we used a cell line expressing the GFP-RNF8 protein, a ubiquitin ligase that accumulates at DSB sites. To study the kinetic accumulation of RNF8 at DNA damage sites, cells expressing GFP-RNF8 protein were irradiated with increasing number of α -particles (1, 10, and 100) and protons (100 ± 10 and 1000 ± 32), and then followed using online live cell microscopy. At $t=0$ min, the GFP-RNF8 protein is distributed homogeneously in the nucleus. The formation of GFP-RNF8 radiation-induced foci became visible within 2 min for all the irradiation conditions. The fluorescent spot corresponding to the accumulation of GFP-RNF8 at the damage site was measured and normalized using the same method as for XRCC1 (Fig. 23.a). The normalized fluorescence intensity was plotted as a function of time after irradiation in form of a curve characterized by the recruitment time constant T and the fluorescent intensity amplitude A , obtained using equation 1 (Fig. 23.b). The 2 parameters T and A were calculated after integrating at least 16 cells per irradiation condition.

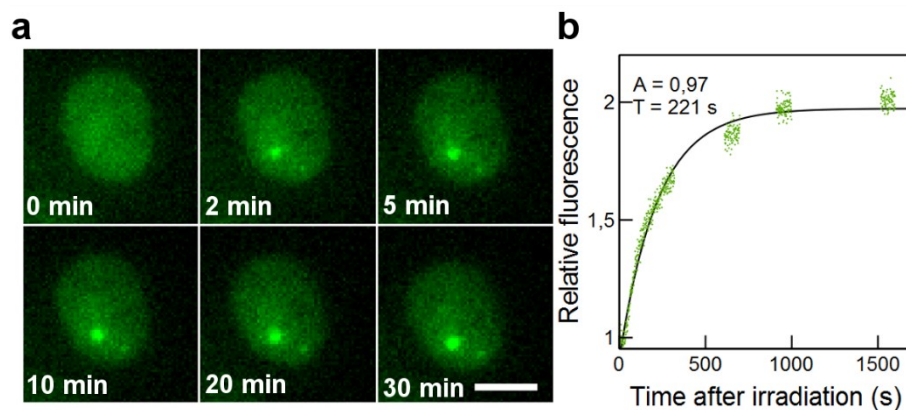


Fig. 23. Real time recruitment of GFP-RNF8 to the micro-irradiated area. (a) Cell nucleus irradiated with 100 α -particles. The time at which the cell is hit by particles is set as $t = 0$. At $t=0$ min, the GFP-RNF8 protein is distributed homogeneously in the nucleus. Selected time points, covering the signal of the fluorescent spot corresponding to the accumulation of GFP-RNF8 at the irradiated site are shown. Scale bar: 10 μ m. (b) Kinetics curve showing the normalized data from the cell nucleus in the fig. a, fitted to a model for the first-order response. The distribution of the GFP-RNF8 protein is recorded at 1 s intervals during 300 s, then at 10 min, 15 min et 30 min during 100 s to minimize the GFP photobleaching.

Fig. 24.a. shows that the recruitment time T of the GFP-RNF8 does not significantly change after increasing the number of incident particles from 1 to 10 α -particles (p-value of 0.15). By contrast, when 100 α -particles are delivered the recruitment time decreases significantly

compared to that obtained after 10 α -particles (p-value $< 10^{-7}$). When 100 and 1000 protons are delivered, the mean time does not change significantly (p-value of 0.18). Comparing different particle LETs with similar ED (i.e. 10 α -particles and 100 protons) the mean recruitment time is shorter when cells are irradiated with α -particles with respect to the mean recruitment time of cells irradiated with protons (p-value of 0.02). This tendency is also observed when cells are irradiated with 100 α -particles and 1000 protons (p-value $< 10^{-10}$).

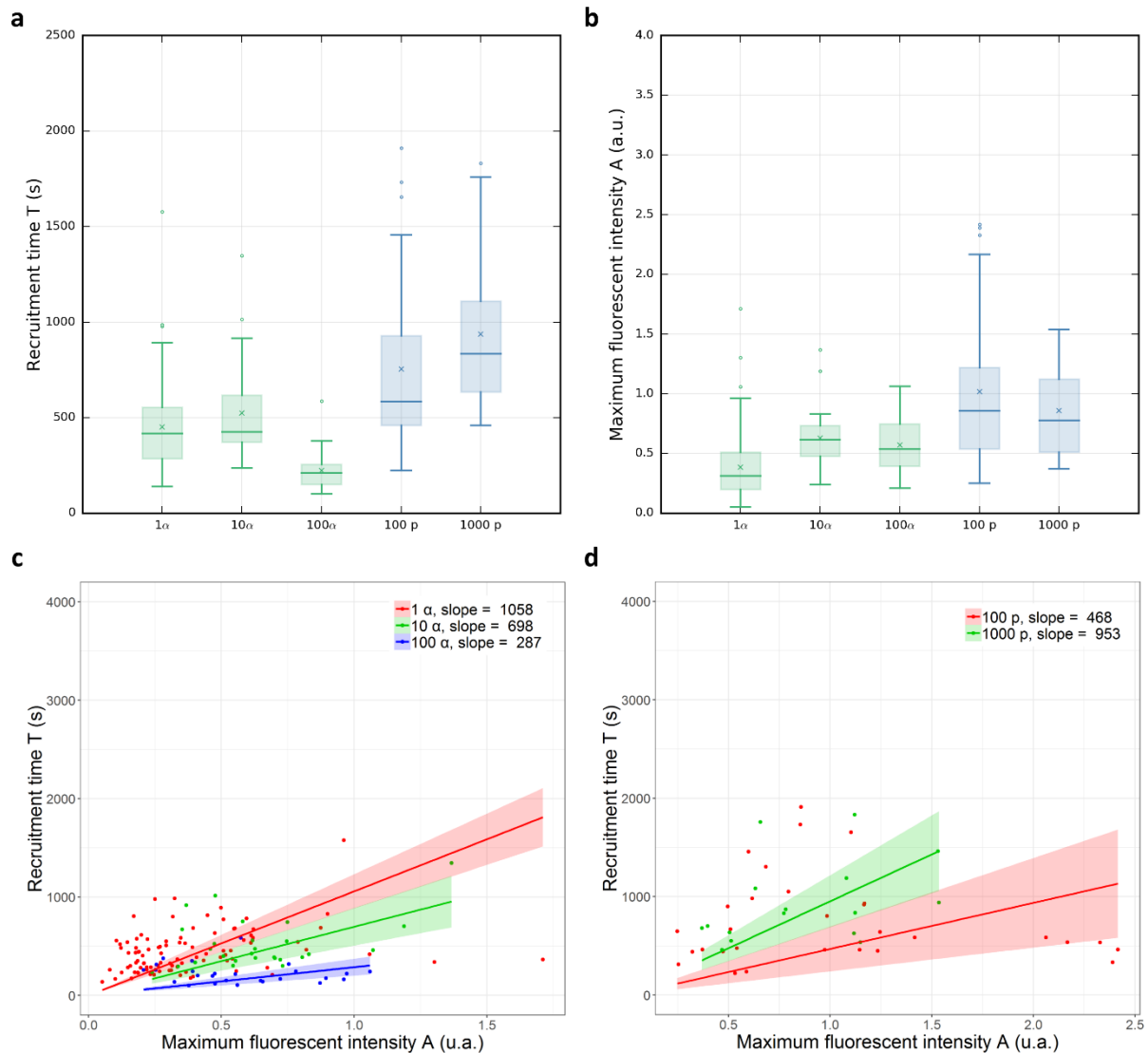


Fig. 24. Recruitment time (T) and amplitude of the fluorescent intensity (A) of GFP-RNF8 after proton and α -particle irradiations. (a) Box plots representing the recruitment times (T) of GFP-RNF8 cells after irradiation with increasing numbers of α -particles (green) and protons (blue). T changes as a function of the ED when α -particles are increased from 10 to 100; it does not significantly change for the other irradiation condition. GFP-RNF8 protein is faster when cells are irradiated with α -particles with respect to protons. (b) Box plots representing the amplitude of the GFP-RNF8 intensity in cell nuclei after irradiation with increasing numbers of α -particles (green) and protons (blue). A doesn't change significantly with the increasing of the number of delivered particles. Considering the two parameter T and A together for (c) α -particles and (d) protons, there is no dependency between T and A by increasing the number of delivered particles.

Fig. 24.b. shows that the amplitude of the intensity A of the GFP-RNF8 does not significantly change after increasing the number of incident particles from 1 to 100 α -particles and 100 to 1000 protons. Comparing different particle LETs with similar ED (i.e. 100 α -particles and 1000 protons), there is no significant difference in the statistical distribution of the A values. Considering the 2 parameters, Fig. 24.c and Fig. 24.d show T and A are independent for all number of delivered particles. While increasing the number of delivered particles, the recruitment time T present no dependency with the amplitude of the fluorescent intensity for the 2 LET values.

II. Modelling results using Geant4-DNA

II.1. Track structure and energy distributions of α -particles and protons after CPM irradiations

The first step of the microdosimetric study was to simulate the track structure of single 3 MeV α -particle and proton. It is presented as a spatial distribution of the physical interactions in the target volume with highly localized ED along the particle path: the charged-particles ionizations, the secondary electrons ionizations, and the excitations events. Fig. 18 presents 3D track structures of (a) one α -particle and (b) one proton in 1 μm with the physical interactions having non-zero EDs. The EDs by all the events correspond to the particle LET value ($\text{keV}/\mu\text{m}$). The data shows that one α -particle produces 10 times more physical interactions per unit length than one proton. This ratio of 10 corresponds to the one between the two particles LETs. Comparing the spatial distribution of the physical interactions, for α -particle the events are distributed around the track core while for proton the events are more dispersed from the particle track. In fact, protons are lighter than α -particles. When entering the water volume, protons are faster than α -particles for the same initial energy (3 MeV). Therefore, the secondary electrons produced (delta-rays) by protons have higher velocity than those produced by α -particles which results in physical interactions of electron farther from the particle track.

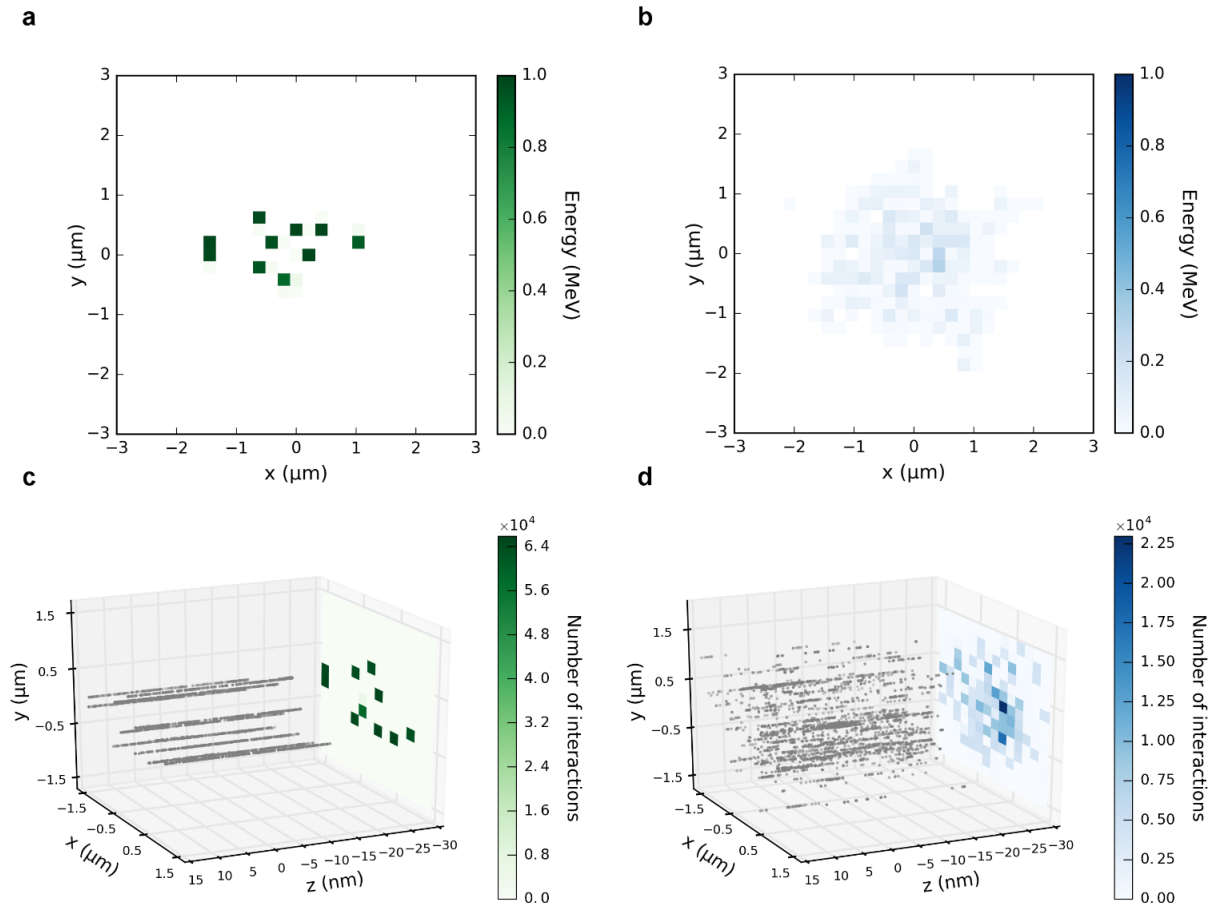


Fig. 25. Geant4 simulations of the EDs and the physical interaction distributions in a homogeneous cubic nucleus. (a, b) The ED is calculated in this volume with $6 \mu\text{m}$ in thick. The 2D histograms represent the sum of the EDs along the z-axis with $0.2 \times 0.2 \mu\text{m}^2$ binning corresponding to the resolution of the experimental microscopic fluorescent images. Similar mean total ED is recorded when (a) 10 α -particles (9.74 MeV) and (b) 100 protons (7.08 MeV) are delivered, but the spatial distribution of the EDs is different. For α -particles, the EDs are projected into one saturated bin, while for protons the EDs are more dispersed in a continuous way. **(c, d)** The distributions of the physical interactions in 3D corresponding to the EDs in panels a and b are calculated in similar volume but with 30 nm thick (visualization memory limit constraints). The charged-particles are delivered at the entry of the water volume along the z-axis (from left to right). The 3D scatter-plot grey points correspond to physical interactions having non-zero EDs. (c) For α -particles, the physical interactions are concentrated around the particle tracks and the 10 α -particles are presented as 10 individual particle tracks while for protons the physical interactions are more dispersed.

The second step of the microdosimetric study was to compare the energy distribution by the 2 particle types for the similar EDs (ratio of 10). Similar mean total EDs per beam spot were reached after 10 α -particles or 100 protons and after 100 α -particles or 1000 protons (0.9 MeV/ α -particle, 0.07 MeV/proton). Fig. 25.a and 25.b present 2D histogram of the EDs by 10 α -particles and 100 protons projected along the z-axis ($6 \mu\text{m}$ depth) respectively with a binning of $0.2 \times 0.2 \mu\text{m}$ (x and y axis). The chosen binning corresponds to the pixel size of the microscope fluorescent images acquired during the experimental cellular micro-irradiation. To compare the spatial distribution in 3D of the EDs by 10 α -particles and 100 protons, the

physical interaction with non-zero EDs are presented respectively in Fig. 25.c and 25.d. These physical interactions are simulated in a homogeneous water cube with 30 nm in thick. This thickness was chosen to be able to visualize the 3D distribution because of the memory limit constraints for thicker water volume. The 10 α -particles delivered in 1.5 μ m FWHM can be considered as 10 individual single tracks in close vicinity (Fig. 25.c). When 100 protons are delivered in 1.5 μ m FWHM, the distributions of physical interactions and the EDs are more dispersed in a continuous way.

II.2. DNA damages prediction and distribution based on clustering calculation at the nanometric scale

The difference in the distribution of the EDs at the nanometer scale between α -particles and protons can induce a difference in the number of each type of DNA damage. In addition, beam focusing may lead to an overlap of particle tracks and also change the proportion of each DNA damage type. For these reasons, based on the “Clustering” example available in Geant4-DNA, I calculated the number of 3 types of DNA damages, including SSBs, DSBs and CSBs, after the different irradiation conditions at the nanometric scales. Fig. 26 show the total number of DNA damages after α -particles (green bars) and protons (blue bars) irradiations for different numbers of incident particles. The number of lesions increases linearly with the delivered number of incident particles independently from their types.

The proportion of each type of DNA damage with respect to the number of total damages is 56% SSBs, 31% DSBs and 13% CSBs for α -particles , and 86% SSBs, 8% DSBs and 6% CSBs for protons. Despite the increasing number of incident particles, the proportion of each damage type does not change which means that even with a microbeam focused at 1.5 μ m, there is no focusing effect on the number of induced DNA damages.

The (CSBs+DSBs)/SSBs ratio values are 0.78 for α -particles and 0.15 for protons, indicating that α -particles induce mostly DSBs and CSBs, and protons induce mostly SSBs. In addition, the clustering example gives access to the clusters size, corresponding to the number of SSBs in each cluster. Comparing similar EDs, the clusters size is bigger after irradiations with α -particles with respect to protons. The clusters sizes calculated after irradiation with α -particles are between 2 and 26 SSBs while for protons are between 2 and 6 SSBs, showing that the DNA damage induced after α -particle irradiations are more complex.

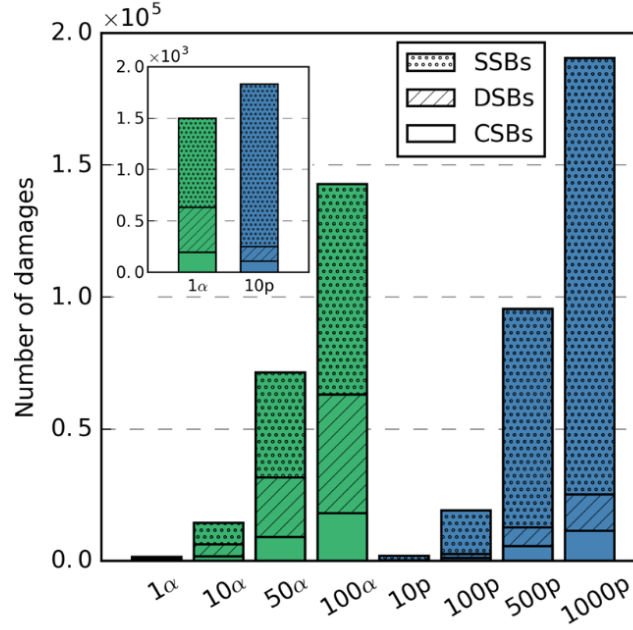


Fig. 26. Calculation of the number of different type of DNA damage based on the clustering algorithm of Geant4-DNA. The number of SSBs, DSBs and CSBs was calculated for α -particles (green) and protons (blue) after irradiations with increasing number of incident particles. For all the numbers of delivered α -particles, the ratio (CSBs+DSBs)/SSBs value is 0.78, and for the protons is 0.15. The proportion of each type of DNA damage with respect to the number of total damage is 56% SSBs, 31% DSBs and 13% CSBs for α -particles, and 86% SSBs, 8% DSBs and 6% CSBs for protons.

II.3. DSBs clustering at the micron scale

A further step was to investigate the spatial interaction of the clustered DSBs at the micrometer scale within a chromatin domain (30 nm) leading to more complex DNA lesions, where the complexity refers to additional lesions within some nm distance^{42,43}. Comparing the spatial distribution of DSBs for similar EDs (for example 10 α -particles and 100 protons, Fig. 27), the DSBs induced after irradiations with α -particles are more concentrated around the particle tracks while for protons the DSBs are more dispersed.

After the simulation of the number and the position of DSBs, once again DSBs were clustered using DBSCAN algorithm⁴⁰ with a maximum distance between 2 DSBs to be clustered of 30 nm corresponding to the value of a chromatin domain.

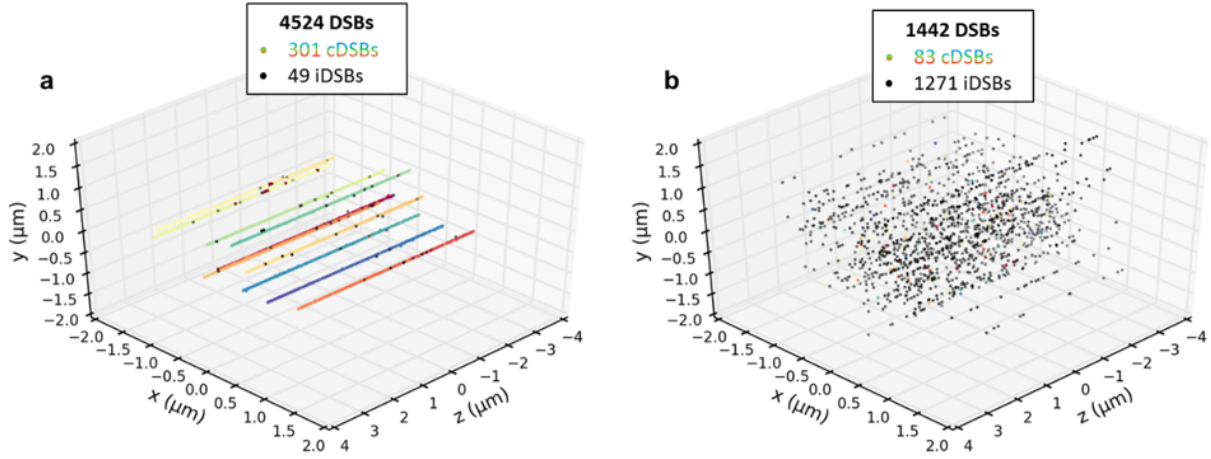


Fig. 27. Three-dimensional spatial distribution of isolated DSBs (iDSBs) and clustered DSBs (cDSBs) calculated using DBSCAN algorithm. A cDSB is defined as a cluster formed by 2 DSBs distant by 30 nm corresponding to the value of a chromatin domain. **(a)** For α -particles, we obtained a value of 30 cDSBs/track and 5 iDSBs/track, and **(b)** for protons 1 cDSBs/track and 13 iDSBs/track. The color dots correspond to clustered DSBs belonging to the same cluster (cDSBs) and the black dots correspond to iDSBs.

The results are shown in Fig. 28. For α -particles, we obtained a value of 30 cDSBs/track and 5 iDSBs/track, and for protons 1 cDSBs/track and 13 iDSBs/track. In addition, considering the size of these cDSBs (in term of numbers of DSBs), the cluster sizes calculated are considerably larger when irradiated with α -particles (between 2 and 450 DSBs) than with 100 protons (between 2 and 6 DSBs).

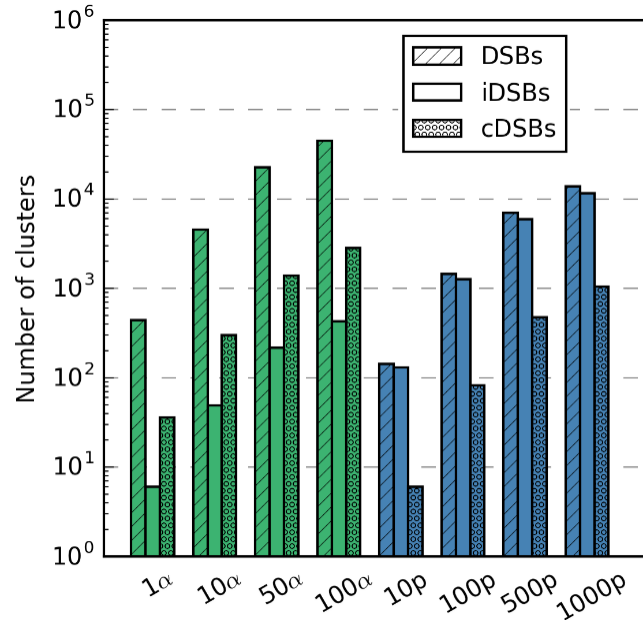


Fig. 28. Calculation of isolated DSBs (iDSBs) and clustered DSBs (cDSBs) using DBSCAN algorithm. After the simulation of the number and the position of DSBs, once DSBs were clustered using DBSCAN algorithm with a maximum distance between 2 DSBs to be clustered is 30 nm corresponding to the value of a chromatin domain.

Discussion

In the present work, we combine experimental measurements of the kinetics of DNA repair proteins with track structure simulation. The main goal is to investigate whether experimental observables such as the recruitment time and the amount of recruited protein are correlated to the nature, the quantity and the localization in space of the DNA damage sites extracted from the simulations. The micro-irradiation experiments were conducted at the AIFIRA microbeam with increasing numbers of protons and α -particles. The impact of both LET and the number of delivered particles (dose) on the *in situ* recruitment kinetics of the GFP-tagged proteins RNF8 and XRCC1 have been investigated.

The XRCC1 protein is considered to act as a central loading platform in SSB repair and BER^{25,26}. GFP-XRCC1 recruitment occurs a few seconds after irradiations. Compared to other studies, immediate and fast recruitment of XRCC1 was observed by all authors^{11–13}. While increasing the number of delivered particles in micrometric spots, (i) the maximum fluorescent intensity increases suggesting that the amount of XRCC1 proteins accumulated at damaged sites increases, and (ii) the recruitment time decreases which means the XRCC1 proteins is recruited faster at damaged sites. When similar energies are deposited by α -particles (LET of 140 keV. μm^{-1}) or protons (LET of 12 keV. μm^{-1}), the recruitment time and the fluorescent intensity do not vary significantly. Compared to studies in the literature using particles having higher LET, XRCC1 showed a fast recruitment to DNA damage similar to the kinetic results obtained in our study. For instance, after irradiation with 0.36 GeV nickel ions (LET of 3873 keV. μm^{-1}) XRCC1 was recruited within 20 s at the ion hit positions in cells and it reached a maximum at about 200 s post-irradiation⁴⁶. Likewise after irradiations with xenon (LET of 8900 keV. μm^{-1}) or uranium (LET of 14300 keV. μm^{-1}), fast recruitment kinetics of XRCC1 accumulation in human cell nuclei were recorded 17 s after irradiation.¹² Therefore, the recruitment of XRCC1 seems to be independent from the particle LET and depends mainly on the amount of ED.

The RNF8 protein has recently been shown to be a key regulator of DNA repair complexes foci and is mainly involved in the DNA ubiquitination of DSBs^{14,15,47,48}. When 1 or 10 α -particles are delivered the GFP-RNF8 recruitment time does not change but a significant decrease was observed with 100 α -particles. These responses can be influenced by the microscopic spatial distributions of physical interactions and EDs⁴⁹. We did not observe changes of GFP-RNF8 recruitment time after increasing the number of delivered protons.

Considering the fluorescent intensity of the protein accumulation spots, no significant variation has been recorded for all the number of delivered α -particles and protons which could indicate that the amount of proteins at the DNA damage sites doesn't change while it accumulates faster. These results suggest that the recruitment time of GFP-RNF8 to radiation-induced DNA damages is mainly dependent on the type of the incident particles (LETs) and the density, the complexity and amount of DNA DSBs.

The microdosimetric simulations provide the spatial distribution of physical interactions and EDs. For protons, they are more dispersed than for α -particles for which they are densely distributed around the particle track. For α -particle, Fig. 25 shows clearly that 10 α -particle tracks are distributed as discrete events at the scale considered in microscopy experiments and can be considered as single impacts with respect to 100 α -particles that cover almost all the irradiated area. In fact, the difference of spatial distribution reflects the complexity of the induced DNA damage⁵⁰. Indeed, based on the clustering calculations, protons generate sparse, simple damage events (mainly SSBs) while α -particles induce mainly DSBs. While increasing the number of delivered particles in a 1.5 μm spot, the proportion of each type of DNA damage remains the same, which means the DNA damage complexity is not influenced by the beam focusing, at least at the nanometer scale. At the micrometer scale, Fig. 27 shows that the spatial distribution of DSBs remains more concentrated around the particle tracks leading to a large number of clustered DSBs forming more complex DNA lesions after α -particle irradiations, while for protons these DSBs are more dispersed leading to a large number of isolated DSBs.

The role of XRCC1 is a loading platform for other proteins after DNA damage. It is recruited with the same kinetic after irradiations with 2 different LETs for which the microdosimetric calculation show different damage complexity for the 2 particle LETs. This suggests that XRCC1 is independent of damage complexity. It depends mainly on the amount of ED and the DNA damage. This probably means that cells recognize DNA damage independently of its complexity, and recruit XRCC1, and then cells recruit specific proteins, such as RNF8, that act to repair complex DNA damage, as underlined by its dependency on particle LET. For RNF8, as its role is mainly involved in DSBs repair, it is recruited faster to damage sites when α -particles are used to irradiate cells inducing mainly DSBs rather than protons inducing mainly SSBs.

The full interpretation of the biological results reported in this study may require overcoming a few limitations related to the microdosimetric calculations. It is in particular the case for the clustering of the DNA lesions. The clustering at nanometer scale was calculated only for

direct effects in a homogeneous water cube. According to recent studies, indirect effects due to free radicals contribute up to 60% of the total induced SBs^{10,41}. The indirect effect calculations are approximate and depend on the choice of different parameters: the probability to induce a strand break, the maximum distance to kill all chemical species created away from any DNA molecules, and the range cut (in ns) to stop simulation after diffusion started. Based on the results obtained by^{10,41}, there is no significant difference of the number of SBs from indirect effects induced by the α -particles (140 keV. μm^{-1}) and protons (12 keV. μm^{-1}).

Taking into account these effects would require more complex modelling of the chromatin structure. Such models are under development in Geant4-DNA and will soon be available. As an example, Sakata *et al.* recently developed a fully integrated MC simulation that calculates early single strand breaks (SSBs) and double strand breaks (DSBs) in a fractal chromatin based human cell nucleus model using Geant4-DNA¹⁰. This complete model open perspective to simulate the different DNA damage with realistic models of DNA starting from nucleotides to the nucleus.

Apart from these limitations, the different DNA damage types and complexity dependency with particle LETs show an agreement with other studies^{7,42,50,51}. The lesions induced by α -particles (140 keV. μm^{-1}) are mostly DSBs and complex damage and the lesions induced by protons (12 keV. μm^{-1}) are mostly SSBs and individual well separated DSBs. However, the number of SSBs and DSBs presented in the present work and based on “Clustering” example of Geant4-DNA are 3 times higher than the results reported by Francis *et al.*⁸ for the same simulations conditions (geometry and clustering parameters). This difference may be due to the choice of the physic list used for the calculation. The physic lists have been evolved with the updated versions of Geant4-DNA. The “G4EmDNAPhysics_option4” used in our calculations may differ from the physic list used in Francis *et al.* In addition, the yields of the different DNA damage were expressed in (Gy⁻¹.Da⁻¹) that depends on the cell nucleus volume considered in the simulations. Therefore, the difference of the nuclear volume thickness used in the calculations of Francis *et al.* (0.5 μm) and in this work (6 μm) may also be at the origin of these discrepancies.

Compared to other studies using real DNA geometries, the amount of these damage are as well over-estimated^{42,43,10}. The number of SBs considered to be clustered as SSBs and DSBs are overestimated. Using a real structure of the DNA, only SBs separated at least by one base-pair are considered as two distinct SBs which is not possible to be taken into account using homogeneous water cube. In addition, when the DNA structure is ruptured several times in

near vicinity, these several lesions are counted as one DNA damage. This cannot be controlled without a real structure of the DNA.

Shortly the Geant4-DNA example allowing the calculation of DNA damage from direct and indirect effects in complex DNA geometries as found in human cells will be open access¹⁰. The use of this example will improve the clustering calculation and the DNA damage number prediction in this study.

References

1. Jakob, B., Rudolph, J. H., Gueven, N., Lavin, M. F. & Taucher-Scholz, G. Live cell imaging of heavy-ion-induced radiation responses by beamline microscopy. *Radiat. Res.* **163**, 681–90 (2005).
2. Jakob, B., Splinter, J., Durante, M. & Taucher-Scholz, G. Live cell microscopy analysis of radiation-induced DNA double-strand break motion. *Proc. Natl. Acad. Sci.* **106**, 3172–3177 (2009).
3. Tobias, F. *et al.* Spatiotemporal Dynamics of Early DNA Damage Response Proteins on Complex DNA Lesions. *PLoS One* **8**, e57953 (2013).
4. Durante, M. & Friedl, A. A. New challenges in radiobiology research with microbeams. *Radiat. Environ. Biophys.* **50**, 335–338 (2011).
5. Mosconi, M. *et al.* 53BP1 and MDC1 foci formation in HT-1080 cells for low- and high-LET microbeam irradiations. *Radiat. Environ. Biophys.* **50**, 345–352 (2011).
6. Hable, V. *et al.* The live cell irradiation and observation setup at SNAKE. *Nucl. Instruments Methods Phys. Res. Sect. B Beam Interact. with Mater. Atoms* **267**, 2090–2097 (2009).
7. Hable, V. *et al.* Recruitment kinetics of DNA repair proteins Mdc1 and Rad52 but not 53BP1 depend on damage complexity. *PLoS One* **7**, 1–11 (2012).
8. Francis, Z., Villagrasa, C. & Clairand, I. Simulation of DNA damage clustering after proton irradiation using an adapted DBSCAN algorithm. *Comput. Methods Programs Biomed.* **101**, 265–270 (2011).
9. Meylan, S. *et al.* Simulation of early DNA damage after the irradiation of a fibroblast cell nucleus using Geant4-DNA. *Sci. Rep.* **7**, 11923 (2017).
10. Sakata, D. *et al.* Evaluation of early radiation DNA damage in a fractal cell nucleus model using Geant4-DNA. *Phys. Medica* **62**, 152–157 (2019).
11. Jakob, B. *et al.* DNA double-strand breaks in heterochromatin elicit fast repair protein recruitment, histone H2AX phosphorylation and relocation to euchromatin. *Nucleic Acids Res.* **39**, 6489–6499 (2011).
12. Tobias, F., Durante, M., Taucher-Scholz, G. & Jakob, B. Spatiotemporal analysis of DNA repair using charged particle radiation. *Mutat. Res. - Rev. Mutat. Res.* **704**, 54–60 (2010).
13. Asaithamby, A. & Chen, D. J. Mechanism of cluster DNA damage repair in response to

- high-atomic number and energy particles radiation. *Mutat. Res. Mol. Mech. Mutagen.* **711**, 87–99 (2011).
14. Kolas, N. K. *et al.* Orchestration of the DNA-Damage Response by the RNF8 Ubiquitin Ligase. *Science (80-.)*. **318**, 1637–1640 (2007).
15. Mok, M. T. S., Cheng, A. S. L. & Henderson, B. R. The ubiquitin ligases RNF8 and RNF168 display rapid but distinct dynamics at DNA repair foci in living cells. *Int. J. Biochem. Cell Biol.* **57**, 27–34 (2014).
16. Chalfie, M., Tu, Y., Euskirchen, G., Ward, W. W. & Prasher, D. C. Green Fluorescent Protein as a Marker for Gene Expression. *Science (80-.)*. **263**, 802–805 (1994).
17. Muggioli, G. Deciphering the biological effects of ionizing radiations using charged particle microbeam: from molecular mechanisms to perspectives in emerging cancer therapies. Cancer. Université de Bordeaux. English. <NNT:2017BORD0599>. <tel-01820606>. (2017).
18. Lan, L. *et al.* In situ analysis of repair processes for oxidative DNA damage in mammalian cells. *Proc. Natl. Acad. Sci.* **101**, 13738–13743 (2004).
19. Mailand, N. *et al.* RNF8 Ubiquitylates Histones at DNA Double-Strand Breaks and Promotes Assembly of Repair Proteins. *Cell* **131**, 887–900 (2007).
20. Okano, S., Lan, L., Caldecott, K. W., Mori, T. & Yasui, A. Spatial and Temporal Cellular Responses to Single-Strand Breaks in Human Cells. *Mol. Cell. Biol.* **23**, 3974–3981 (2003).
21. Caldecott, K. W. Single-strand break repair and genetic disease. *Nat. Rev. Genet.* **9**, 619–631 (2008).
22. Campalans, A. *et al.* Distinct spatiotemporal patterns and PARP dependence of XRCC1 recruitment to single-strand break and base excision repair. *Nucleic Acids Res.* **41**, 3115–3129 (2013).
23. Solarczyk, K. J., Kordon, M., Berniak, K. & Dobrucki, J. W. Two stages of XRCC1 recruitment and two classes of XRCC1 foci formed in response to low level DNA damage induced by visible light , or stress triggered by heat shock. *DNA Repair (Amst)*. **37**, 12–21 (2016).
24. Wei, L. *et al.* Damage response of XRCC1 at sites of DNA single strand breaks is regulated by phosphorylation and ubiquitylation after degradation of poly(ADP-ribose). *J. Cell Sci.* **126**, 4414–4423 (2013).
25. Mortusewicz, O., Leonhardt, H. & Cardoso, M. C. Spatiotemporal dynamics of regulatory protein recruitment at DNA damage sites. *J. Cell. Biochem.* **104**, 1562–1569

- (2008).
26. Campalans, A. *et al.* Interaction with OGG1 Is Required for Efficient Recruitment of XRCC1 to Base Excision Repair and Maintenance of Genetic Stability after Exposure to Oxidative Stress. *Mol. Cell. Biol.* **35**, 1648–1658 (2015).
 27. Löbrich, M. & Jeggo, P. A. The impact of a negligent G2/M checkpoint on genomic instability and cancer induction. *Nat. Rev. Cancer* **7**, 861–869 (2007).
 28. Mahaney, B. L., Meek, K. & Lees-Miller, S. P. Repair of ionizing radiation-induced DNA double-strand breaks by non-homologous end-joining. *Biochem. J.* **417**, 639–650 (2009).
 29. Beucher, A. *et al.* ATM and Artemis promote homologous recombination of radiation-induced DNA double-strand breaks in G2. *EMBO J.* **28**, 3413–3427 (2009).
 30. Yan, J. & Jetten, A. M. RAP80 and RNF8, key players in the recruitment of repair proteins to DNA damage sites. *Cancer Lett.* **271**, 179–90 (2008).
 31. Thorslund, T. *et al.* Histone H1 couples initiation and amplification of ubiquitin signalling after DNA damage. *Nature* **527**, 389–93 (2015).
 32. Doil, C. *et al.* RNF168 Binds and Amplifies Ubiquitin Conjugates on Damaged Chromosomes to Allow Accumulation of Repair Proteins. *Cell* **136**, 435–446 (2009).
 33. Bourret, S. *et al.* Fluorescence time-lapse imaging of single cells targeted with a focused scanning charged-particle microbeam. *Nucl. Instruments Methods Phys. Res. Sect. B Beam Interact. with Mater. Atoms* **325**, 27–34 (2014).
 34. Lukas, C. *et al.* Mdc1 couples DNA double-strand break recognition by Nbs1 with its H2AX-dependent chromatin retention. *EMBO J.* **23**, 2674–2683 (2004).
 35. Agostinelli, S. *et al.* GEANT4 - A simulation toolkit. *Nucl. Instruments Methods Phys. Res. Sect. A Accel. Spectrometers, Detect. Assoc. Equip.* **506**, 250–303 (2003).
 36. Incerti, S. *et al.* the Geant4-Dna Project. *Int. J. Model. Simulation, Sci. Comput.* **01**, 157–178 (2010).
 37. Incerti, S. *et al.* Geant4-DNA example applications for track structure simulations in liquid water: A report from the Geant4-DNA Project. *Med. Phys.* **45**, e722–e739 (2018).
 38. Bernal, M. A. *et al.* Track structure modeling in liquid water: A review of the Geant4-DNA very low energy extension of the Geant4 Monte Carlo simulation toolkit. *Phys. Med.* **31**, 861–74 (2015).
 39. Friedland, W., Jacob, P., Bernhardt, P., Paretzke, H. G. & Dingfelder, M. Simulation of DNA damage after proton irradiation. *Radiat. Res.* **159**, 401–10 (2003).

40. Ester, M., Kriegel, H.-P., Sander, J. & Xu, X. A density-based algorithm for discovering clusters in large spatial databases with noise. *Kdd* **96**, 226–231 (1996).
41. Friedland, W. *et al.* Comprehensive track-structure based evaluation of DNA damage by light ions from radiotherapy- relevant energies down to stopping. *Nat. Publ. Gr.* 1–15 (2017). doi:10.1038/srep45161
42. Friedrich, T. *et al.* DNA damage interactions on both nanometer and micrometer scale determine overall cellular damage. *Sci. Rep.* **8**, (2018).
43. Tommasino, F. *et al.* Induction and processing of the radiation-induced gamma-H2AX signal and its link to the underlying pattern of DSB: A combined experimental and modelling study. *PLoS One* **10**, 1–25 (2015).
44. Vadhavkar, N. *et al.* Combinatorial DNA Damage Pairing Model Based on X-Ray-Induced Foci Predicts the Dose and LET Dependence of Cell Death in Human Breast Cells. *Radiat. Res.* **000**, 273–281 (2014).
45. Tabocchini, M. A., Campa, A. & Dini, V. DNA and cellular effects of charged particles. *Health Phys.* **103**, 547–555 (2012).
46. Guo, N. *et al.* Live cell imaging combined with high-energy single-ion microbeam. *Rev. Sci. Instrum.* **87**, (2016).
47. Huen, M. S. Y. *et al.* RNF8 transduces the DNA-damage signal via histone ubiquitylation and checkpoint protein assembly. *Cell* **131**, 901–14 (2007).
48. Bartocci, C. & Denchi, E. L. Put a RING on it: regulation and inhibition of RNF8 and RNF168 RING finger E3 ligases at DNA damage sites. *Front. Genet.* **4**, 128 (2013).
49. Goodhead, D. T. Mechanisms for the biological effectiveness of high-LET radiations. *J. Radiat. Res.* **40 Suppl**, 1–13 (1999).
50. Nikjoo, H., Neill, P. O., Wilson, W. E. & Goodhead, D. T. Computational Approach for Determining the Spectrum of DNA Damage Induced by Ionizing Radiation. **583**, 577–583 (2001).
51. Reindl, J. *et al.* Chromatin organization revealed by nanostructure of irradiation induced γ H2AX, 53BP1 and Rad51 foci. *Scientific Reports* **7**, (2017).

PART III

**Multicellular micro-irradiation: Biological
radio-induced effects by ionizing radiations
in vivo**

Introduction

The ability of CPM to deliver a precise number of particles per cell makes it a relevant tool to study the risks associated to low doses exposure of IR on living organisms. If *in vitro* cell models are mostly used for the characterization of radiation-induced biological mechanisms, the transposition of the results obtained using such models to *in vivo* responses cannot be done directly because the complex tissue responses can intervene. The CPM irradiation of multicellular models can provide a better understanding of these phenomena. Such irradiations have been developed slowly, mainly because of technological challenges that they introduce^{1, 2, 3}. CPM has been gradually extended from the irradiation of monolayers *in cellulo* experiments to the irradiation of three-dimensional tissue models and small multicellular specimens. The definition and the choice of biological models are usually restricted by the limited range of the particles used at CPMs. The first attempts were performed by Belyakov *et al.* to study bystander effects on three-dimensional human tissues irradiated with 7.2 MeV α particles using the Colombia University CPM⁴. Other tissue model like slice culture preparations from humans and rodents were used as a new model system for studying effects of X-rays and heavy ions (Carbon and Xenon) within normal and tumor tissues⁵. So far, several studies focused on small multicellular organisms as biological models such as silkworm larvae⁶, zebrafish embryos^{7,8}, and *Caenorhabditis elegans* (*C. elegans*)^{9, 10, 11}. Among these models, *C. elegans* is the most used living organism for CPM irradiation. *C.elegans* is a free-living transparent nematode that presents numerous advantages justifying its use for *in vivo* investigation of radiation effects. *C. elegans* have a fixed number of cells (959 cells at the adult stage) and is small enough to be compatible with CPM irradiation (the adult body is 50 μm in diameter and 1 mm in length). Its transparent body allows visualizing, directly, specific tissues especially for studying the production and the transfer of damage signals in a whole organism during its development. It has a fast life cycle, simple culture conditions and maintenance, and its cell division is invariant between the nematodes allowing its irradiation in different stages of development.

The microbeam irradiation of this nematode represents a challenge because it requires the targeting of a specific cell within a living and moving multicellular organism. Video microscopy and targeting techniques must therefore be adapted in order to allow precise irradiation. There are several studies that use the combination between the CPM and the *C. elegans* which made it the most widely used multicellular organism for ion microbeam

irradiation. The first work of this type was carried out by Taknami *et al.*, who combined the use of ion beams with *C. elegans* to demonstrate the formation of chromosomal aberrations in the germ cells of adult nematodes after irradiation with 125 MeV carbon ions and 95 MeV Argon ions¹². Bertucci *et al.* developed a new technique to expose specific site of *C. elegans* young adult to 3 MeV protons using the Colombia University RARAF charged-particle accelerator¹⁰. Later they developed a microfluidic tool and they implanted it to the microbeam irradiation of *C. elegans*. The device allows the immobilization of *C. elegans* worms, without the use of anesthesia to minimize the stress, for a rapid and controlled microbeam irradiation of multiple samples in parallel¹¹. More recently, at TIARA microbeam facility in Japan adult nematodes were irradiated with 18.3 MeV/u carbon ions in 3 independent regions (head region, mid region around the intestine and uterus, and tail region) to study the responsible mechanisms for reducing the nematode mobility¹³.

In this study, *C. elegans* was chosen as biological model for the CPM irradiations with protons of 3 MeV at the AIFIRA facility. It presents numerous advantages to perform investigations on late effects of IRs. The protocols and the experimental procedures for micro-irradiate *C. elegans* were carried out within a previous thesis work in the group iRiBio before my integration into it¹⁴. Two stages of *C. elegans* were selected for 2 different studies: 2-cell stage embryos and L1 larvae.

All the studies using CPM to irradiate *C. elegans* are performed either on larvae or adults. To validate the experimental procedure to reproducibly micro-irradiate this organism and observe the IR effects at the AIFIRA platform, 2-cell stage *C. elegans* embryos was chosen as biological target. This simple stage of *C. elegans* life cycle with 2 cells allowed following more easily the irradiated cell in the first cell divisions following irradiation.

In contrary to the irradiation of adherent cells *in vitro* that are at a defined and stable stage of the cell cycle for the considered time scale, the early embryos of *C. elegans* have a much faster division cycle. A 2-cell stage embryo passes to the 4-cell stage in less than 20 minutes. The challenge was thus to be able to irradiate rapidly dividing cells at a well-defined stage of the cell cycle, i.e. the 2-cell stage, and to follow the radiation induced response throughout the first cell divisions. For this purpose, online time lapse fluorescence microscopy was used. Using this approach, it is possible to determine precisely the moment at which the irradiation must take place and the position in the nucleus that will be irradiated. The nucleus of the AB cell of 2-cell stage embryo was irradiated at the beginning of mitosis, at a specific stage of chromatin condensation (prophase).

The first aim was to maintain the embryos on the CPM irradiation line and to visualize directly the formation of DNA damages in the irradiated cell nucleus. For this purpose, the WS1433 (*opIs34 [hus-1::GFP]*) transgenic *C. elegans* strain carrying HUS-1::GFP fluorescent protein has been chosen. This protein is expressed in early stage embryo homogenously distributed in the cell nucleus. Following irradiation, it accumulates at the DNA damaged sites. In order to irradiate the embryos at the beginning of mitosis of the cell cycle, the GZ264 (*isIs17 [pGZ265:pie-1::GFP-pcn-1(W0D2.4)]*) transgenic *C. elegans* strains was used. The PCN-1::GFP protein allowed the visualization of the S-phase in early embryos and during nuclear cycles. A third *C. elegans* strains, MG152 (*xsIs3 [HisH2B::GFP; rol-6(su1006)]*), was chosen to study the impact of irradiations on chromatin dynamics during the embryo cell divisions. The MG152 strain expresses the histone H2B::GFP protein that enables highly sensitive chromatin detection in all phases of the mitosis.

The microbeam at the AIFIRA facility¹⁵ presents a Gaussian distribution with 1.5 μm full width at half maximum (FWHM) at the target position. The locally radiation-induced DNA damages in specific steps of the cell nucleus division were observed, *in situ*, and the radiation-induced consequences in the early stages of the embryo development were determined.

Such selective irradiations lead to a localized ED at the micron scale within the exposed cell while the surrounding area is not irradiated. Consequently, the commonly used macrodosimetric quantity such as the absorbed dose reaches its limits to describe the ED quantity. The descriptions of IR interactions at the micrometer scale using microdosimetric model are more valuable in such situations. At this scale, the concept of specific energy is preferred over the absorbed dose. It is defined as the ratio of the energy imparted to the mass of the volume of interest^{16, 17}. Several tools have been developed for microdosimetric calculations¹⁸. At this scale, most existing codes seek to evaluate the ED of particles in the main cell compartments (nucleus and cytoplasm) and to perform calculations in cellular models made of simple geometries, based on the combination of basic mathematical volumes (spheres, ellipsoids, cylinders...) ^{19, 20}.

However, these geometric models do not consider the variety of geometries encountered in a typical cell population (morphological variations, variations according to the cell cycle, chromatin condensation...). To overcome this limitation, several approaches have been proposed. Douglass *et al.* developed an algorithm producing cellular models spatial coordinates and random sizes. The position of the subcellular compartments within each cell (nucleus, nucleolus, endoplasmic reticulum) is also partially random²¹. However, this model remains based on simple ellipsoidal volumes. Incerti *et al.* modeled, using Geant4, the

irradiation of a realistic model of epithelial cell by an ion microbeam. This approach takes advantage of the possibility, in Geant4, of importing voxelized geometries (so-called parametrized volumes). This cellular model is based on fluorescence confocal imaging²². Miller *et al.* have also shown the interest of using confocal microscopy to model electron microbeam irradiation of a three-dimensional multicellular tissue²³. It allows more realistic calculations of energy and dose deposit, particularly in the case of irradiation with particles where the influence of the variations of cellular geometry has a significant impact on the ED. This tool also makes it possible to characterize the spatial distribution of the ED s. More recently, Barberet *et al.* extended this model to the irradiation of a cell monolayer by ion microbeam or by radioactive sources in order to highlight the influence of the morphological variability of the cells in a population on the calculation of the absorbed dose²⁴.

Based on this latest methodology, the aim of my contribution for this study was dedicated to:

- Develop microdosimetric models to simulate the spatial distribution of protons, and to calculate the ED and the specific energy, unmeasurable during the irradiation, in different compartment of 2-cell stage *C. elegans* embryo (chromatin, nuclear volume and embryo). These calculations were performed with the Geant4-DNA version of Geant4 for the modeling of the early biological damage-induced by IR at the DNA scale simulating each interaction in details²⁵. I used a realistic 3D geometry of the 2-cell stage embryo reconstructed from images acquired by confocal microscopy at the Bordeaux Imaging Center (BIC).
- Verify if the chromatin condensation at the moment of irradiation had an impact on the ED, since the early stage *C. elegans* embryos have a fast division cycle and the chromatin condensation can differ and affect the energy distribution. For this purpose, I modeled 40 cells of 2-cell stage embryos and calculated the energy distribution in the different compartments.

In parallel to this work, a second project named “ECHOS” (*Etude de la réponse au stress radio-induit CHrOnique ou ciblée chez le modèle biologique C. elegans*) was undertaken to study chronic induced stress response after exposure to IR. Several studies demonstrated that chronic exposure to IR impacts significantly the organism reproduction which is an essential biological function for maintaining populations^{26,27}. Buisset-Goussen *et al.* show that chronic exposure of *C. elegans* nematode at a dose of 50 mGy/h results in a decrease in the cumulative number of larvae produced per organism. This effect is comparable after 200h (from the embryo stage until the end of the reproduction period) and 65h (from the embryo to

the adult stage) of irradiation²⁸. This last result suggests that the effects induced by the irradiation could depend on the dose received by the organisms exclusively during the period of development of gonads and / or gametogenesis which is the L1 larva stage.

In this context, *C. elegans* L1 larvae, more precisely the two somatic gonad precursor cells present at this stage, have been chosen to be irradiated. These 2 cells give rise to the entire somatic gonad responsible of the production of gametes (called testes in male and ovaries in female). Knowing that these 2 cells, within a living organism that can move, have a small size of 3.32µm as diameter comparable to the beam size (1.5µm), the use of CPM to targeted individual cells could induce variation in the delivered dose between the larvae with a probability of not hitting inside the cell. This assumes a specific configuration to perform the irradiation using the AIFIRA CPM. The dose must be delivered homogeneously to the zone around the 2 cells without irradiating the whole larvae to determine the specific contribution of these cells in the stress response of IR.

- The aim of my contribution in this part is to model the *C. elegans* L1 larva irradiations with protons using the Geant4 toolkit to define a strategy to deliver homogeneously 3 selective and controlled doses of 0.3 Gy, 3 Gy and 30 Gy to the zone around the 2 cells using the CPM. These 3 irradiations have been carried out to be compared with whole larvae exposure for several days with the 3 different cumulative doses of gamma rays (0.3 Gy, 3 Gy and 30 Gy) at the MIRE platform in IRSN²⁹.

Methods

I. Micro-irradiation of a multicellular living organism: *C. elegans*

Passing from *in vitro* cell models to multicellular models *in vivo* was one of the challenges of microbeam irradiation. Protocols were developed to carry out a targeted micro-irradiation of early embryos of *C. elegans*. In addition, the CPM coupled to online fluorescence time-lapse microscopy was used to track first cell divisions and their evolution for several tens of minutes after irradiation. This section consists to resume the experimental procedures established in a previous thesis work within the group iRiBio in 2015¹⁴.

I.1. *C. elegans* transgenic strains

Well characterized transgenic strains of *C. elegans* are available at the Caenorhabditis Genetics Center (CGC, University of Minnesota, USA). These strains are designed to express one or more proteins of interest coupled to one or more fluorochromes. Here, the nucleus of one of the two cells from 2-cell stage *C. elegans* embryo was irradiated. The chosen strains express fluorescent proteins (coupled to GFP) present in the cell nucleus, related to chromatin visualization, damage recognition, and cell cycle. The three strains used in these works are WS1433, GZ264 and MG152.

- The WS1433 strain expresses the histone HUS-1::GFP fusion protein in early embryos and the adult germline homogeneously distributed and limited to the interphase nucleus. This protein is involved in DNA damage checkpoint acting as a DNA damage sensor and stopping cell cycle. It has been shown that this protein is accumulated at the damaged DNA sites³⁰. Thus, in this work, this strain was used to visualize the formation of DNA damage relocated in the irradiated embryo cell nucleus in distinct foci that overlap chromatin.
- The GZ264 strain expresses the GFP::PCN-1 (Proliferating Cell Nuclear Antigen1) fusion protein, which is involved in DNA replication and cell cycle regulation. In phase S, this protein is exclusively localized in the nucleus whereas it is more localized within the cytoplasm during the mitosis³¹. In addition, it has been shown that

this protein is a marker of cell cycle and especially of the S-phase³². For this work, the GZ264 strain was used to selectively irradiate the beginning of mitosis embryo cells.

- The MG152 strain expresses the histone H2B::GFP fusion protein which is involved in the formation of the necessary nucleosomes for chromatin condensation during the different phases of cell divisions (mitotic chromosomes and interphase chromatin). This strain was first used to visualize and to target selectively the embryo cell nuclei. In a second step, it was used to study the impact of irradiations in chromatin dynamics during embryo cell division.

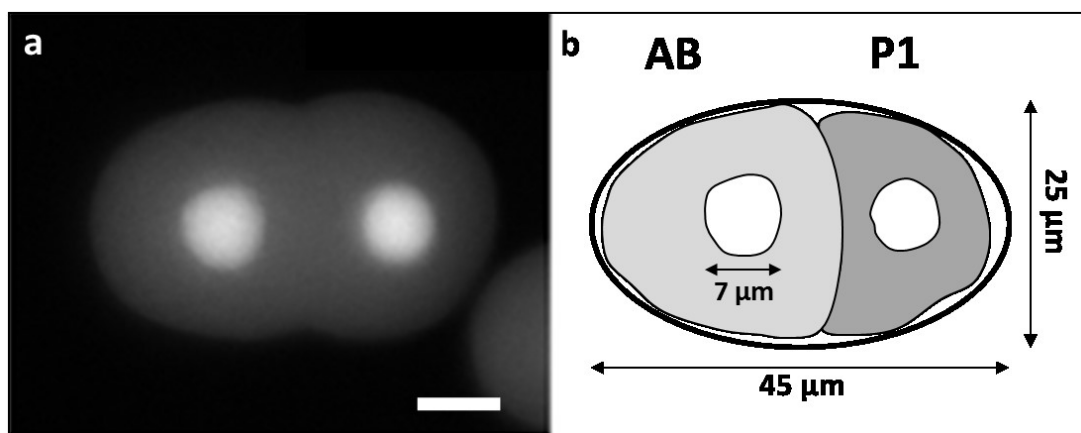


Fig. 29. **a.** Microscopic fluorescence image acquisition of a control 2-cell stage embryo of the *C. elegans* GZ264 strain with the expression of GFP::PCN-1 that marks the cell nucleus. **b.** Schematic representation of the 2-cell stage embryo showing the dimensions of the different compartments. The embryo represented by an ellipse of 45 μm x 25 μm as a major and a minor axis respectively with 2 cell nuclei of 7 μm diameter. Scale bar 10 μm .

1.2. Preparation of culture wells for irradiation

The 2-cell stage embryos having the particularity to be formed of 2 cells well distinct and easily identifiable in microscopy were chosen to be micro-irradiated. They are composed of an AB cell and a P1 cell oriented along an anteroposterior axis (Fig. 29). The preparation of the culture dish used for the irradiations is summarized in 3 steps as shown in Fig. 30. Embryos extracted and selected at early stage are deposited between two foils of polypropylene 4 microns thick in the presence of a thin layer of culture medium (M9 Buffer) to prevent dehydration. All these steps should be done in less than 20 min, which takes an average of 2-cell embryos to reach the 4-cell stage.

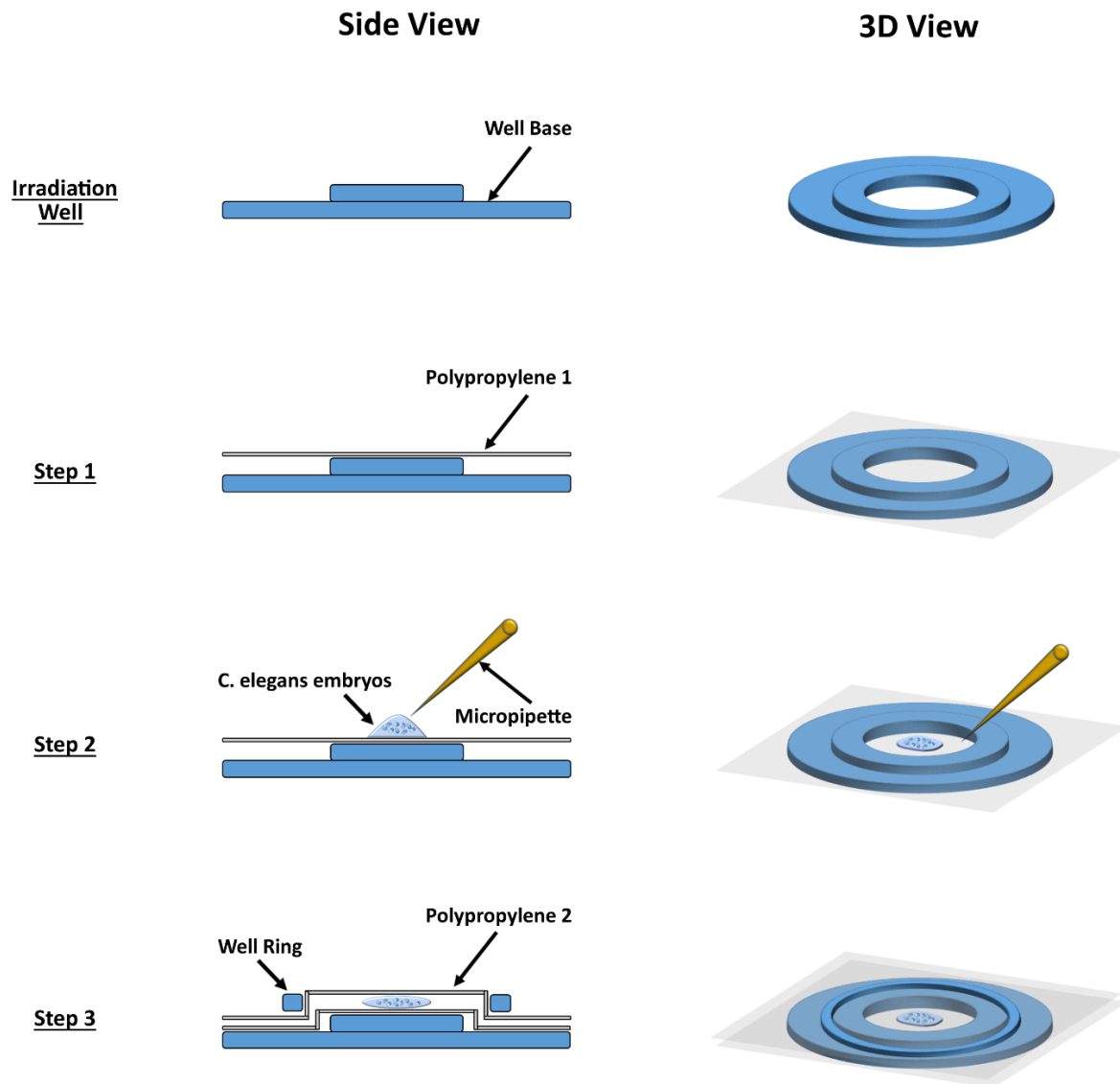


Fig. 30. Schematic representation of the montage of the irradiation well for of *C. elegans* embryos. The early stage embryos are selected from a population of embryos extracted by chemical treatment. **Step 1:** a 4 μm thick polypropylene foil is placed on the base of the irradiation well. **Step 2:** early embryos are deposited on the polypropylene with a micropipette. **Step 3:** a second foil of polypropylene is then placed on the embryos. The embryos are therefore maintained in culture medium, between the two sheets of polypropylene. These are stretched thanks to the ring which is finally placed on the base of the irradiation well.

I.3. Irradiation and video microscopy

The protocol used for the irradiation of *C. elegans* embryos can be described by 3 stages: visualization of embryos, the selection of embryos to be irradiated, and irradiation and video microscopy. The culture well containing embryos is placed vertically between the extraction window of the CPM and the objectives of the microscope (Fig. 31).

The difference in size between the two cells (AB and P1) is used to differentiate them easily. The AB cell nuclei were irradiated with 3 MeV protons. The path of these particles in liquid water of about 150 μm is indeed enough to irradiate embryos that have a thickness of about 30 μm and to count the particles downstream the sample as well. For this purpose, a silicon detector positioned on the microscope objective wheel was used.

The targeting of the embryos and the image acquisition were carried out with a 63x objective. In order to keep a good compromise between the duration of the video acquisition and the number of irradiated samples, images were acquired for a maximum duration of one hour. Thus, the embryo passes from the 2-cell stage to the 8-cell stage.

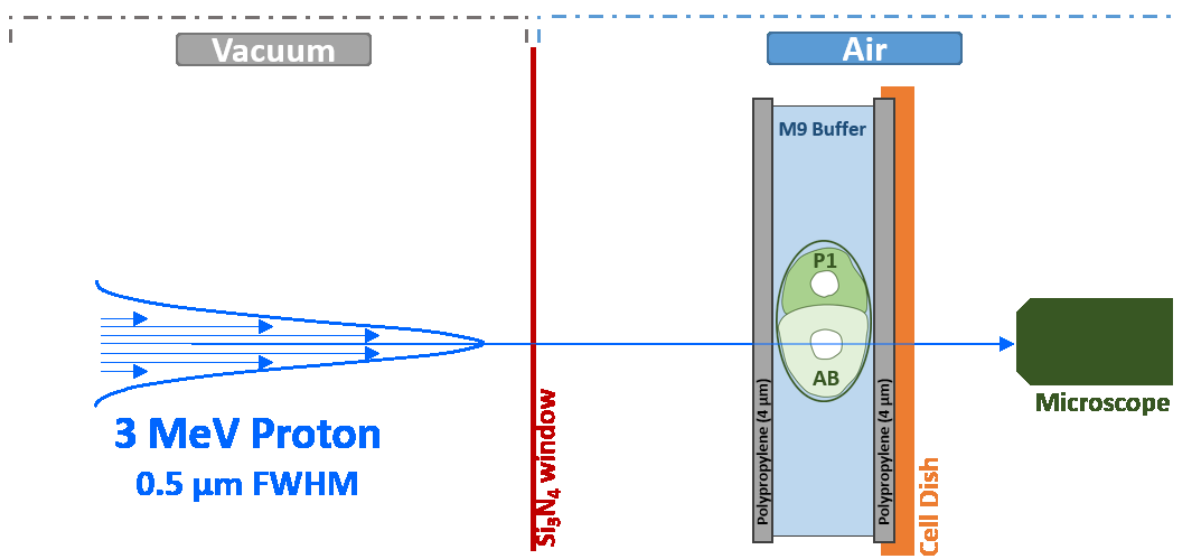


Fig. 31. Scheme of the irradiation end-station. The embryos are maintained between two thin polypropylene foils (4 μm thickness) and the AB nucleus is targeted using online fluorescence microscopy. The beam is positioned on the targeted cell by means of electrostatic deflection and an exact throw a Si₃N₄ window.

II. Micro-dosimetry of *C.elegans* embryo ion microbeam irradiations

In this section, I present a detailed overview of my contributions to develop a microdosimetric study to model the experimental irradiations by CPM of a realistic multicellular model, *C. elegans*.

The experimental approach using CPM is complementary to the well-established laser micro-irradiation (LMI). Both CPM irradiation and LMI allow the deposition of localized energy in a nuclear volume. The interest of using CPM is that it reproduces better the effects of IRs.

To understand the biological phenomena observed during micro-irradiations of *C. elegans* embryos, the ED and the specific energy in different compartment must be precisely characterized.

The dose received by specific compartments of *C. elegans* 2-cell stage embryos cannot be easily extrapolated from the data usually obtained for adherent mammalian cells. When targeting subcellular structures using a microbeam, the dose is delivered in micrometric areas. The usual dosimetry methods are not relevant in this configuration because the irradiation is very inhomogeneous spatially. This poses difficulties in defining the volume of interest and therefore the concept of absorbed dose is of limited use. For this, the ICRU introduced the concept of specific energy which is defined as the ratio of the energy transmitted and the mass of the volume concerned¹⁷. This ED by the charged-particles significantly depends on the geometry and composition of the target.

For this purpose, by using the Monte Carlo Geant4 modeling tool, the irradiations were modeled in realistic phantom of the *C. elegans* embryo based on voxelized geometry.

II.1. Modeling of the *C. elegans* embryo with a realistic phantom

When targeting a cellular or sub-cellular compartment of living biological specimens using a CPM, the physical interactions of the charged-particles inside the compartment cannot be measured directly, and the specific energy absorbed in specific compartments (chromatin, nucleus and cytoplasm) is usually estimated by calculations based on cell geometry modeled using simple mathematical volumes. Since in this study we focused on the radio-induced DNA effects, modeling the embryo and the nuclear volume of the embryo as homogeneous volumes is not enough. It doesn't give access to the calculation of the ED in specific compartment of the nucleus such as the chromatin.

For this purpose, I used realistic geometries of the 2 cell-stage embryos reconstructed from high resolution images acquired by confocal microscopy to provide the Monte Carlo simulations.

The originality of this method is that it allows microdosimetric calculations on a realistic three-dimensional cellular geometry of the *C. elegans* embryo. This geometry is simulated in form of a voxel arrangement determined from the confocal microscopy images. In the following, the realistic model of *C. elegans* 2-cell stage embryo is called "phantom", by analogy with the human phantoms used in the field of medical physics and dosimetry.

II.1.1. Preparation of embryo samples for confocal microscopy

The preparation of embryo samples for confocal microscopy is composed of 2 parts:

The first part is the extraction of *C. elegans* embryo populations. For this first part, embryos were isolated from synchronized populations of young gravid hermaphrodites using the bleaching method for which the worms are sensitive to bleach solution while the egg shell protects the embryos from it. Here are the different steps of the extraction protocol:

- Collect synchronized populations of well-fed young gravid hermaphrodites with M9 buffer (3 g/l KH_2PO_4 , 6 g/l Na_2HPO_4 , 5 g/l NaCl, 1 mM MgSO_4).
- Wash the collected populations three times with sterile water to remove bacteria.
- Pellet worms *via* centrifugation (2 min., 2000 rpms, room temperature).
- Add a freshly prepared alkaline hypochlorite solution (1.5 % (v/v) NaOCl, 1M NaOH) and swirl every 2 minutes with vortex-mixing (~6 min.).
- Pellet the released embryos *via* centrifugation at 2000 rpms for 2 minutes.
- Wash the embryos three times with M9 buffer followed by centrifugation at 2000 rpms for 2 min with discarding carefully the supernatant.

The second part is immunofluorescence staining of the embryos that can be described by the following steps:

- Fixe immediately the freshly extracted embryo populations in cold 4% (w/v) paraformaldehyde and their eggshells were freeze-cracked by placing at -20°C during 15 min.
- Pellet the embryos *via* centrifugation (2 min., 2000 rpms, RT) and replacing the paraformaldehyde by cold acetone for permeabilization (2 min, -20°C) and, finally washed twice in M9.
- Remove the M9 and replacing it by a freshly prepared solution of phalloidin (10:1000 (v/v), Molecular Probes) and Hoechst³³³⁴² (2:5000 (v/v), Molecular Probes).
- Incubate the embryos overnight at RT under gentle agitation.
- Wash the embryos the next day *via* two series of centrifugation (2min. 2000 rpms) with M9 with discarding the supernatant.
- Suspend the pelleted embryos in 2-3 drops of Prolong Gold Antifade reagent (Molecular Probes)
- Transfer the pelleted embryos by pipetting for mounting between glass slides using ProLong™ Antifade Gold Reagent (Invitrogen).

II.1.2. Confocal fluorescence microscopy

Confocal microscopy is a specialized form of standard fluorescence microscopy that uses particular optical components to generate high-resolution images of material stained with fluorescent probes. Instead of illuminating the whole sample at once, laser light is focused onto a defined spot at a specific depth within the sample. This leads to the emission of fluorescent light at exactly this point. A pinhole inside the optical pathway cuts off signals that are out of focus, thus allowing only the fluorescence signals from the illuminated spot to enter the light detector. By scanning the specimen in a raster pattern, images of one single optical plane are created. 3D objects can be visualized by scanning several optical planes and stacking them using suitable microscopy deconvolution software (z-stack). It is also possible to analyze multicolor immunofluorescence staining using state-of-the-art confocal microscopes that include several lasers and emission/excitation filters.

Three-dimensional images of 2-cell stage embryos were acquired with a Leica DM6 confocal microscope CFS TCS SP8 at the Bordeaux Imaging Center (BIC).

The acquisition of the images was done with a 40x oil immersion lens. The size of the images was 512 x 512 pixels with a pixel size in (x, y) of about 0.1 μm x 0.1 μm . The distance between 2 planes was 0.3 μm (z-size) with an average of 80 planes per embryo stack (Fig. 32.a & 32.b). We chose this z-step value to have a good resolution in an optimal acquisition time.

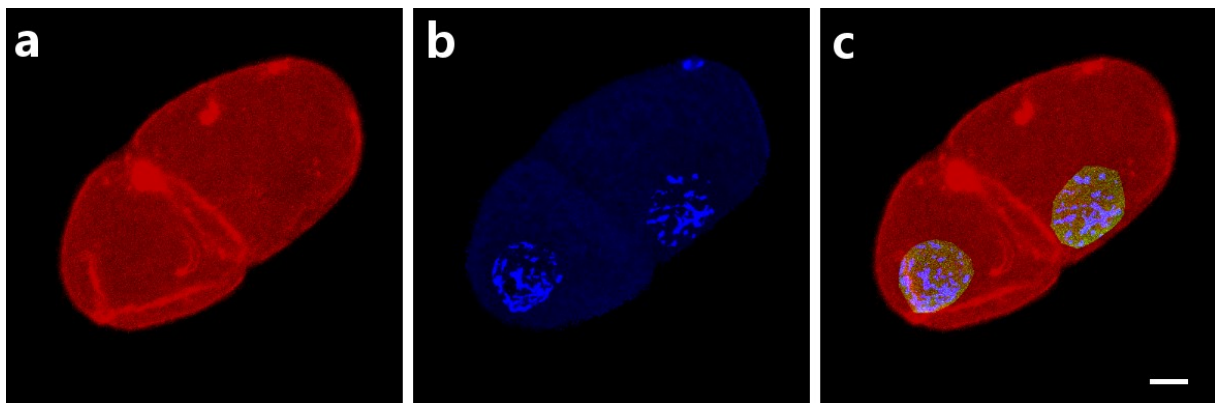


Fig. 32. a-b. Images of z-axis projection of a confocal microscopy stack acquisition of a *C. elegans* 2-cell stage embryo labeled with phalloidin (in red) and Hoechst³³³⁴² (in blue). **c.** The chromatin (in blue), the embryo (in red) and the nuclear volume (in green) are defined using these 2 staining by applying a threshold of intensity to separate them. Scale bar 5 μm .

In the table below, I summarize the parameters of the lasers and detectors used in the image acquisition sequences. We used 2 types of laser, Optically Pumped Semiconductor Laser (OPSL) and diode, and 2 detectors PhotoMultiplier Tubes (PMT) and Hybrid Detector (HyD).

Staining	Laser	λ_L (nm)	Intensity (%)	Detector	λ_d (nm)
Phalloïdin	OPSL	552	55	PMT	583 - 657
Hoechst ³³³⁴²	Diode	408	1	HyD	410 - 488

Table 1. Parameters of the lasers and the detectors used for confocal image acquisitions

II.1.3. Creation of the three-dimensional phantom using ImageJ

The methodology for converting confocal image data into a three-dimensional phantom has been previously described in Barberet *et al.* 2012²⁴.

Images acquired by confocal microscopy are transferred to ImageJ, which is public access software (<http://rsbweb.nih.gov/ij/>) for 3D phantom reconstruction. At first, the images were edited by adjusting the brightness and contrast to reduce background noise especially for Hoechst³³³⁴² marking. An intensity threshold was then applied for each color to separate the fluorescent objects (ex. chromatin) from the background in each slice of the stack. According to the 2 staining colors, 3 volumes were defined: the chromatin from the labeling in Hoechst³³³⁴² (in blue), the embryo volume from the phalloidin labeling (in red), and the nuclear volume (in green). In fact, the blue images were saturated and used to define manually the nuclear volume (in green) (Fig. 32.c).

An ImageJ macro was developed to transform the confocal images to a data file containing the phantom parameters. The macro makes it possible to create 3 parametrized volumes from each color R, G and B according to the order of priority indicated for the volumes of interest. The priority order defines in the case of overlapping volumes the voxels belong to which one. In our case the order of priority is B, G, R corresponding to the chromatin first, and then the nuclear volume and last the embryo. The macro scans the images a first time to count the number of voxels in each channel and a second time to store the value of each voxel of the phantom. By using this ImageJ macro, a text file called "phantom.dat" is created from these digital images in RGB format. This file contains the total number of voxels for each color channel (RGB), the size of the voxel according to the 3 dimensions (x, y, z), a positional shift

for (x, y, z) expressed in pixels to center the phantom with the other volumes defined in Geant4 (ex. the liquid water volume) at the irradiation source position, the density of the voxels for each color and the list of positions and compositions (belonging to which color) of each voxel (Fig.33).

3980678	3770877	195794	14007	←	Voxel numbers : Total Red Green Blue
0.103	0.103	0.3		←	Voxel size in μm : x y z
-256	-256	-30		←	Shift in pixels : x y z
1	1	1		←	Voxel densities : Red Green Blue
267	130	4	1		
268	130	4	1		
269	130	4	1		
270	130	4	1		
251	131	4	1		
253	131	4	1		
254	131	4	1		
264	131	4	1		
265	131	4	1		
268	131	4	1		
271	131	4	1		
250	132	4	1		
251	132	4	1		
252	132	4	1		
262	132	4	1		
263	132	4	1		
265	132	4	1		
266	132	4	1		

Voxel positions: x y z
Voxel channels: 1 = Red, 2 = Green, 3 = blue

Fig. 33. Example of a "phantom.dat" file showing its format that was read in the CellParameterization class in Geant4.

II.1.4. Implementation of the phantom in Geant4-DNA

The implementation of cellular phantoms in Geant4 is described by Incerti *et al.* 2009²². In this approach which is purely parameterized, the phantom consisted of multiple identical copies of a voxel having the size indicated in the file "phantom.dat". This file is read in the class CellParametrisation in Geant4 developed by Incerti *et al.* 2009. Each voxel contains information of its position within the phantom and its composition (belonging to which volume). The cellular phantom used in the *C. elegans* 2-cell stage embryo modeling is represented in Fig. 34 with a very low resolution (32x32 pixels) so that it can be showed in the Geant4 visualization interface.

The simulations of realistic *C. elegans* phantoms were performed with the Geant4-DNA extended version of the public version Geant4.10.2.p02 of Geant4. Geant4-DNA simulate explicitly all the physical interactions of ionizing particles in the irradiated medium and do not use any production cut-off³³. Protons and secondary electrons are tracked down to a lowest energy limit of 0 eV and about 10 eV respectively. In the MeV range, the dominant physical processes affecting protons are nuclear scattering, electronic excitation, ionization,

and charge exchange. Nuclear scattering was simulated using the G4DNAElastic class, electronic excitation was simulated using G4DNAExcitation class and ionization was simulated using the G4DNAIonisation class. Further details on these classes can be found in the Geant4 documentation (<http://geant4-dna.org/>)²². Calculation of EDs and doses in Geant4-DNA can only be done in liquid water. For this reason, the irradiations were done at the entrance of the water volume encompassing the embryo. The target AB cell was irradiated with microbeam modeled as a mono-energetic proton beam of 3 MeV having a Gaussian distribution with a FWHM of 1.5 μm (the size of the microbeam affected by all the material traversed) (Fig. 34).

During irradiation, the EDs above 0 in each voxel is calculated and then stored in a table declared in the RunAction class. At the end of the simulation, I had 3 output files containing the energy values in each of the red, green and blue color channels. All dosimetric data can then be calculated from these 3 files. For example, the specific energy deposit in the embryo can be calculated from the ratio between the total energy ED in the 3 color channels (the sum of the 3 output files) and the mass of the set of all parallelepiped voxels constituting the embryo (value marked in the header of the file "phantom.dat"). The calculations were done for 10^3 and 10^4 incident protons. Experimentally, the embryos were irradiated first with 10^4 protons corresponding to an energy ED high enough to see the irradiation effects and then the embryos were irradiated with a lower energy with 10^3 protons.

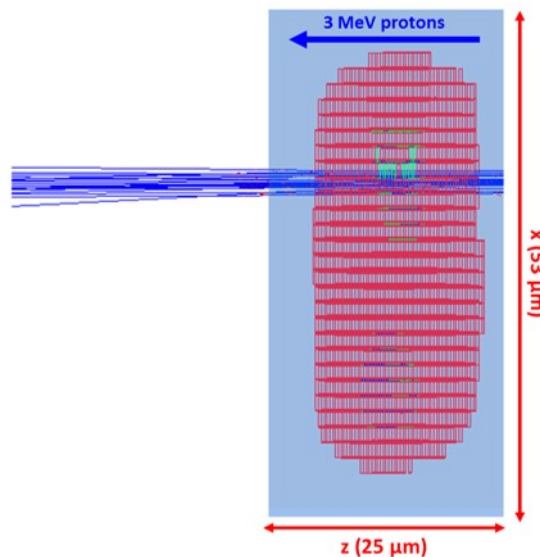


Fig. 34. Top view of low resolution voxelized phantom of the 2-cell stage embryo in Fig. 32 irradiated with 20 incident protons of 3 MeV. The embryo is illustrated as red voxels phantom, the nuclear volumes illustrated with green voxels, and the nuclei illustrated with blue voxels. The incident protons trajectories are represented by blue lines. The red lines show the trajectory of the secondary electrons generated in the air.

II.2. Modeling 40 embryo cells with different chromatin stages

In order to study the effects of IR in a multicellular organism, I have irradiated selectively 2-cell stage *C. elegans* embryos formed of the AB and P1 cells. The division of these cells are fast, it takes only 20 minutes to pass from the 2-cell stage to the 4-cell stage. The irradiated AB cells can be in different states depending on their cell cycle (with different chromatin densities) during the irradiation time. To verify if there is an impact of the biological conditions of the chromatin on the energy imparted to it at the time of our irradiations, I investigate various chromatin condensation states during embryos development.

The aim is to simulate the energy distribution in the nuclei of *C. elegans* embryos having different condensation levels of chromatin. For this purpose, 20 *C. elegans* embryos 2-cell stage were selected from the confocal microscopy images stained with phalloidin (in red) and Hoechst³³³⁴² (in blue), thus 40 nuclei with different chromatin condensation levels (Fig. 35).

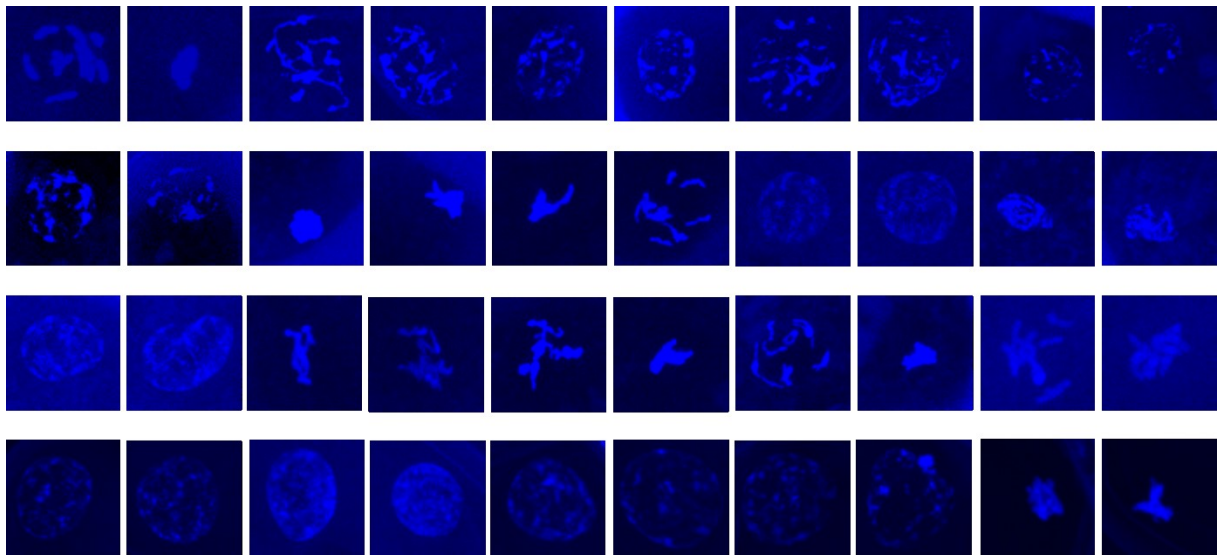


Fig. 35. Set of 40 nuclei of *C. elegans* 2-cell stage embryo with different chromatin shapes and densities. Each image corresponds to the z-projection of the stack slices of the blue channel.

Embryos were modeled and implanted in Geant4 using the same methodology explained in Part I.2. Each nucleus of the 40 cells was irradiated with 10^3 protons of 3 MeV focused on $1.5 \mu\text{m}$. The specific energy and the ED in the chromatin, nuclear volume and embryo volumes were calculated.

III. Micro-dosimetry of *C.elegans* L1 larvae

To study the chronic induced stress response after exposure to IRs, L1 *C. elegans* larvae, more precisely the 2 somatic gonad precursor cells, were selected to be irradiated with 3 MeV protons using CPM (Fig. 36). Since the 2 cells have a small size of about 3.32 μm as diameter comparable to our microbeam (AIFIRA) size at the sample position (1.5 μm) and they are included in a moving living organism, a targeted irradiation induced a heterogeneous dose distribution in these 2 cells with a probability not hitting the cell. Therefore, the dose had to be delivered homogeneously around the cells without irradiating the whole larva, as shown in the area corresponding to the red square in Fig. 36.a. The aim of the microdosimetric study is to find a way to deliver a homogeneous dose to the zone around the 2 cells using CPM.

Modeling *C. elegans* L1 larva with simple geometric shapes

In order to deliver the dose homogeneously using a CPM to the zone corresponding to the red square, I developed a simple geometric model describing the *C. elegans* L1 larva for testing different irradiation pattern dimensions (5x5; 6x6; 11x11) and different microbeam distributions (FWHM of 0.5, 4, 5 and 10 μm). The L1 larva was modeled as a cut torus containing two spherical cells, confined in a liquid water medium (equivalent of the M9 buffer medium) between two foils of polypropylene (Fig. 36.b). The dimensions of the larva and the cells were evaluated from fluorescence images taken by the microscope (Fig.36.a). I used a diameter of 11.7 μm for the torus and a diameter of 3.32 μm for the two spherical cells separated by a distance of 5.3 μm .

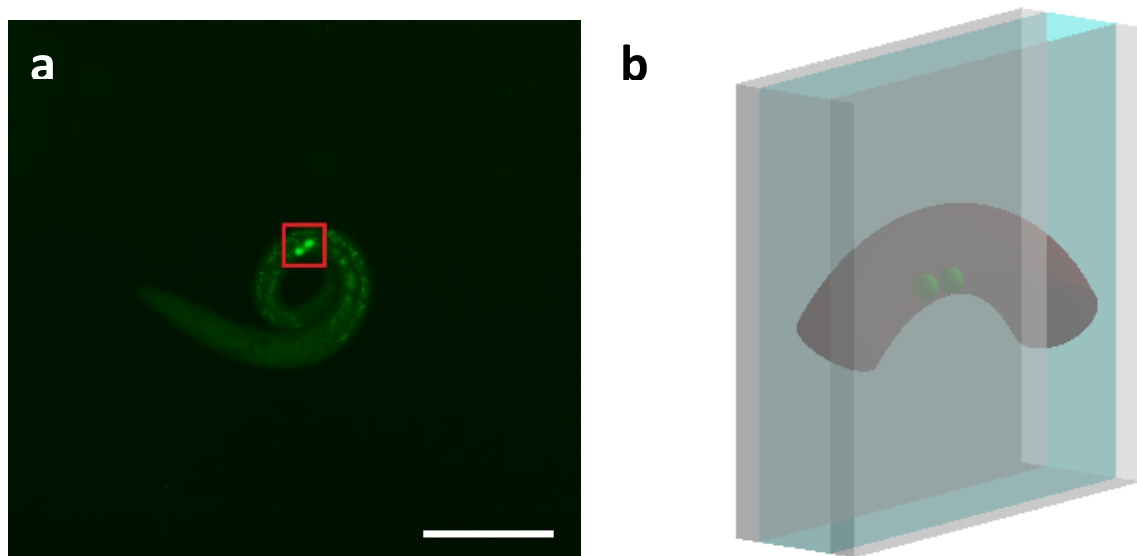


Fig. 36. a. Microscopic image of a L1 larva with the 2 somatic gonad precursor cells in green fluorescence. The red square corresponds to the irradiated area of the larva. **b.** Modeling with Geant4 of the *C.elegans* larva L1 (brown) with 2 somatic gonad precursor cells (green) confined in liquid water (blue) between 2 polypropylene foils (gray). Scale = 50 μm .

The irradiations with the microbeam were modeled as a mono-energetic proton beam of 3 MeV having different Gaussian distributions with FWHM of 0.5, 4, 5 and 10 μm . The specific energy and the ED in each cell and the whole larva were calculated for the different irradiation configuration (pattern dimension and microbeam distribution). The Geant4.10.2.p02 was used with a physics list based on the physical constructor "G4EmLivermorePhysics". During the irradiations the L1 larva are fixed but alive and can move. To take into account the position of the gonads in the larva, the calculations were done for 4 different positions of the gonads (top, bottom, front and back).

Once the pattern dimension and the beam distribution are chosen, doses are calculated as function of the particle LET and fluence to determine the number of protons to delivered per pattern dot to have a homogenous dose in the 2 cells of 0.3, 3 and 30 Gy in order to compare it to whole larva irradiation at the MIRE platform (IRSN).

Results

The first section of the following chapter gives a brief summary of the experimental results obtained from the irradiations of 3 different transgenic strains of *C. elegans* nematodes, which have been performed during a previous study¹⁴. In section II, I present in detail the modeling results of my microdosimetric study carried out by numerical calculations in order to characterize the ED and the specific energy in the different compartments of the embryo.

I. Experimental results

I.1. Visualization of the consequences of CPM irradiations

Micro-irradiation of MG152 embryos

In order to irradiate the embryos, it is necessary to define the optimal conditions for visualization of the early stages of cell division in an early *C. elegans* embryo. For this, embryos of the MG152 transgenic strain were used. These embryos express histone H2B fused to GFP, allowing to visualize the chromatin and its different stages of condensation during mitosis^{34, 35}. The cell divisions are followed directly online using time-lapse fluorescence microscopy. Well-established irradiation techniques based on the CPM, use previously developed for *in vitro* culture studies were adopted³⁶. To obtain high-quality time-lapse movies in healthy embryos, the acquisition rates should be fast enough to capture dynamic changes during the development process without illuminating too much the embryos to avoid photobleaching and phototoxicity. For this, images with 200 ms exposure time were taken with 10 seconds intervals allowing to follow both irradiated and sham-irradiated (control) embryos during up to 40 minutes.

An anomaly in the AB cell nucleus division was shown after irradiation with 10^4 protons of 3 MeV. At the beginning of the metaphase, the chromosomes align correctly on their division plane, but their separation does not take place correctly, and they seem to be linked by chromosomal bridge. This phenomenon persists in the next stages of division as a consequence of the irradiation of the nucleus AB before it enters division. Regarding the P1 nucleus, which has not been irradiated, no chromosomal abnormalities appeared during the division.

Micro-irradiation of WS1433 embryos

In order to directly observe the radiation-induced DNA damage, the transgenic strain WS1433, which expresses the HUS-1::GFP fusion protein in the nuclei of germ cells and early embryos was used. It has been shown that after the DNA-induced damage in adult worm germ cells, HUS-1::GFP protein accumulates at damaged DNA sites³⁰. This protein expresses homogeneously in a non-irradiated nucleus, and during cell division, and more particularly during metaphase, the nuclear membranes disintegrate, and the protein is then released in the cytoplasm of embryonic cells. During anaphase, and the reformation of nuclear membranes, the protein accumulates in the daughter nuclei, and is again visible homogeneously in the nuclei at the end of the mitosis. Swiftly after irradiation with 10^4 protons of 3 MeV, accumulation of the HUS-1::GFP protein appear within the irradiated AB nucleus sites in distinct foci that overlap chromatin. This accumulation persists during the division of the AB nucleus and remains present in the daughter nuclei. The accumulation of HUS-1::GFP protein indicates the presence of radio-induced DNA breaks in the irradiated nucleus. On the other hand, no abnormal accumulation of the HUS-1::GFP protein within the P1 nucleus or its daughter nuclei was detected.

Micro-irradiation of GZ264 embryos

To visualize the S-phase in early embryos and during subsequent cell or nuclear cycles, the GZ264 strain, which express the GFP::PCN-1 protein fusion within the nuclei of embryonic cells was used. The GFP::PCN-1 protein has previously been used as a marker of S-phase during embryonic cell division^{32, 37}. The GFP::PCN-1 protein is expressed within the cell nucleus, diffuses into the cytoplasm at the beginning of mitosis, and relocates to the nuclei at the end of the mitosis. This allowed to carry out targeted irradiation of early embryonic nuclei in prophase which is the first phase of the mitosis. Thus, AB cell nuclei of GZ264 embryos were irradiated with 10^3 or 10^4 protons of 3 MeV at the center of the cell, just before their division. After irradiation, the nuclei enter mitosis, which is visible by the disappearance of the signal GFP::PCN-1. During anaphase, the protein accumulates again within the newly formed nuclei. When the AB nucleus is irradiated with 10^4 protons, the ABa and ABp daughter nuclei have an abnormal morphology and appear to be connected with chromosomal bridge. This structure strongly resembles the chromosomal bridges radially induced previously described with the MG152 strain. This type of anomaly was not observed after irradiation of the AB nucleus with 10^3 protons.

These results are showed and discussed with more details in the article³⁸ joined to this manuscript here after.

II. Modelling results

II.1. *C. elegans* embryo modeling with voxelized realistic phantom

To calculate the EDs in different compartments of the *C. elegans* 2-cell stage embryo (the chromatin, the nuclear volume and the whole embryo), I used the 3D geometry reconstructed from confocal microscopy. This methodology provides the total amount of ED in the 3 compartments as well as its distribution in space. Fig. 37 shows the energy distribution in the chromatin (Fig. 37.a & 37.b) and in the whole embryo (Fig. 37.c & 37.d) after irradiation with 10^3 and 10^4 protons of 3 MeV. The data obtained using this approach are summarized in table 2. I calculated the corresponding specific energy as the ratio of the absorbed energy to the sum of the masses of voxels constituting the target (chromatin, nuclear volume or embryo). The mass of the different compartments has been extrapolated by multiplying the sum of voxels volume constituting each compartment by liquid water density.

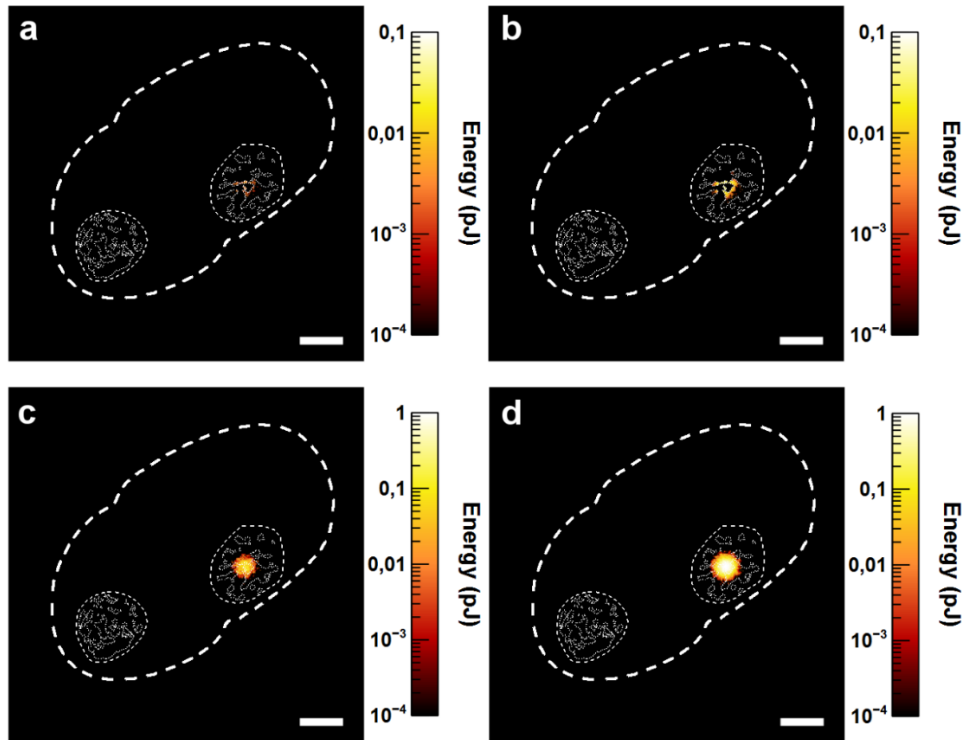


Fig. 37 a-b. Distribution of ED calculated using Geant4-DNA in the chromatin after irradiation with 10^3 protons (total ED of 0.4 pJ) and 10^4 protons (total ED of 3.8 pJ) of 3 MeV presented in 2D (x, y) as the sum of the ED along z-axis. **c-d.** Distribution of ED calculated using Geant4-DNA in the whole embryo after irradiation with 10^3 (total ED of 29.7 pJ) protons and 10^4 protons (total ED of 305.2 pJ) of 3 MeV presented in 2D (x, y) as the sum of the ED along the z-axis. The white dashed lines correspond to the outlines of the 3 volumes of interest extract from z-projection image of all the acquisition slices. It is noted that the energy is exclusively localized in

the irradiated nucleus AB. The non-irradiated nucleus P1 does not receive any ED. The energy scale is logarithmic and corresponds to the total ED by (x, y) position. Scale bar 5 μ m.

	<i>Energy deposit per proton (fJ)</i>	<i>Mass (Kg)</i>	<i>Specific energy for 10³ protons (Gy)</i>
<i>Chromatin</i>	0.4	2.2×10^{-14}	18.2
<i>Nuclear volume</i>	9.5	2.1×10^{-13}	45.2
<i>Whole embryo</i>	29.8	1.3×10^{-11}	2.3

Table 2. Summary of the calculated and simulated data on realistic 3D-rendering of a 2-cell stage *C. elegans* embryo.

The ED is localized in the irradiated nucleus of the cell AB and there is no ED in the non-irradiated nucleus of the cell P1.

Since the cell division in *C. elegans* embryos is a rather fast process (20 minutes to pass from 2-cell stage to 4-cell stage) and since the methodology used for Monte Carlo simulations is based on realistic geometries that can consider the variety of different chromatin condensation state, I investigated the impact of the DNA/chromatin condensation level on the energy imparted to the chromatin.

II.2. Effect of chromatin condensation on energy deposits in 40 embryo cells

For this part, 40 embryo cells having different chromatin condensation states were selected. For each cell nucleus, the EDs by all particles are calculated and recorded in the 3 volumes (chromatin, nuclear volume and all the embryo) after irradiation with 10^3 3 MeV protons. The volumes of the chromatin, the nucleus and the embryo were calculated as the sum of voxels constituting them. According to the chromatin condensation status throughout the cell cycle progression of the AB cell ($t=0$ to 4 min), 5 distinct chromatin distributions, representative of distinct mitosis progression states, could be discriminated from confocal imaging (Fig. 38).

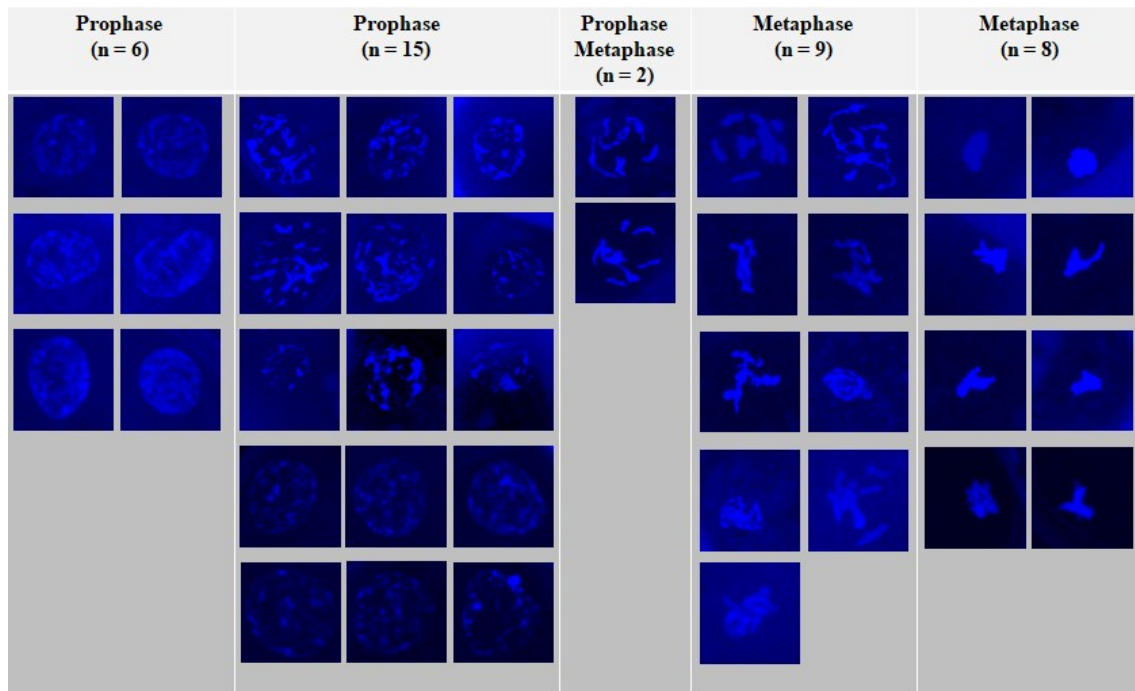


Fig. 38. Classification of the 40 embryo cell chromatin into 5 different chromatin condensation stages observed from confocal images using Hoechst³³³⁴² stain (blue).

The calculated mean ED value in the whole embryo is 34.1 ± 8.4 pJ (Fig. 39.a). The small difference of the mean ED in the embryos can be explain by the thickness (number of slices) of the stacks acquisition used to reconstruct the embryo volume (Fig. 39.a). The calculated ED in the chromatin is different depending on the chromatin distribution observed in the stage prophase or metaphase. The values obtained for the ED in the chromatin are coherent with the geometric shapes and volumes of the simulated chromatin. As illustrated in Fig. 39.c, even if some variation of the chromatin distribution is found in prophase, it does not affect the ED in the chromatin (0.5 ± 0.15 pJ). By contrast, in metaphase a significant different of the ED in the chromatin was found with respect to prophase stage.

Fig. 39.b shows that the total ED in the nuclear volume for 40 *C. elegans* embryo cells have a mean value of 10.5 ± 2.9 pJ.

Despite the similar mean ED in the nuclear volume, the distribution of the energy between the chromatin and the rest of the nuclear volume is different. Only 2% to 5% of the ED is localized in the chromatin when the cells are irradiated in prophase. This ratio increases from 25% to 60% in metaphase where the chromatin is more condensate and centered in the nucleus, i.e. on the particles track path.

Considering the video microscopy acquisition on the microbeam line, the first cell division of 2-cell stage embryos revealed that the chromatin condensation during irradiations

corresponding to prophase stage, which means at our irradiation time conditions, limited variations in terms of energy imparted to the chromatin is expected between samples

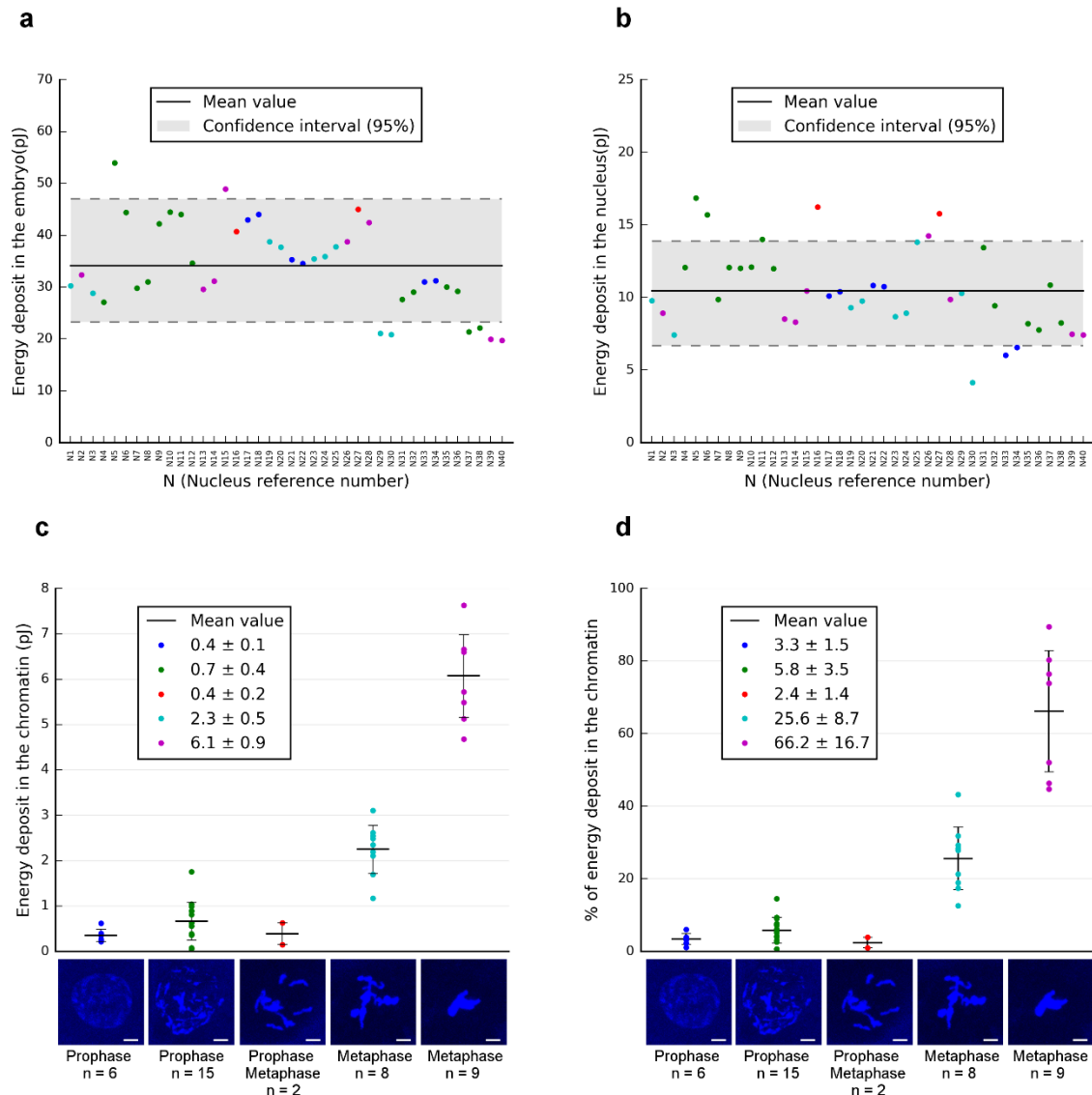


Fig. 39. Monte Carlo calculation of the ED in chromatin, the nuclear volume and the embryo of 40 *C. elegans* cell embryos in 2-cell stage having different chromatin condensations using the same methodology described above. **a.** The total ED in the whole embryo had a mean value of 34.1 ± 8.4 pJ after irradiation with 10^3 protons. **b.** The ED in the nuclear volume having a mean value of 10.5 ± 2.9 pJ after irradiation with 10^3 protons. **c.** The total ED (for 10^3 protons) for each chromatin according to its condensation stages along the mitosis. 2D-projections of 5 different chromatin distributions revealed by Hoechst³³³⁴² (blue) and recorded in 40 embryonic cells by confocal microscopy. Scale bar: 3 μ m. **d.** The energy proportion between chromatin and nuclear volume for the 5 condensation states of chromatin were calculated. It shows that for the same ED in the nuclear volume, only 2% to 5% of the ED is localized in the chromatin in prophase while this ratio increases from 25% to 60% in metaphase.

II.3. *C. elegans* L1 larva modeling and irradiation

After testing different pattern dimensions and proton microbeam distributions, the final irradiation was carried out with a Gaussian beam having FWHM of 4 μm delivered in a pattern of 16x16 μm formed of 5x5 points with a step of 4 μm between 2 points (Fig. 40).

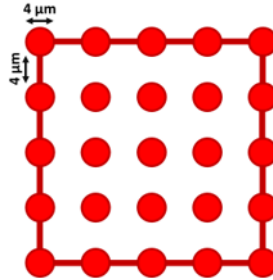


Fig. 40. Irradiation pattern of 16 x 16 μm dimension with a step of 4 μm

A beam size of 4 μm increase the probability to hit the cells of 3.2 μm diameter without irradiating the whole larva. Before reaching the sample, a 2 μm thick diamond detector is placed at the exit of the beam to count the particles passing through it. The distance between the sample and the detector was 350 μm . Fig. 41 shows the irradiation of the 2 somatic gonad precursor cells of L1 larva simulated in Geant4 according to the conditions mentioned above. At the exit of the detector, the 5 points of the irradiation pattern are visibly spaced, but after their passage through the air, the protons reach the larva in a dispersed manner, delivering a homogeneous distributed dose in the zone around the 2 cells and in the larva. After testing the 4 cell positions, I obtained mean specific energy values of 2.7 ± 0.2 Gy for the larva, 2.9 ± 0.4 Gy for the cell1 and 2.6 ± 0.2 Gy for the cell2, which means that the specific energy is distributed homogenously in the 3 compartments and is not impacted by the cell positions in case the larva move during the irradiation.

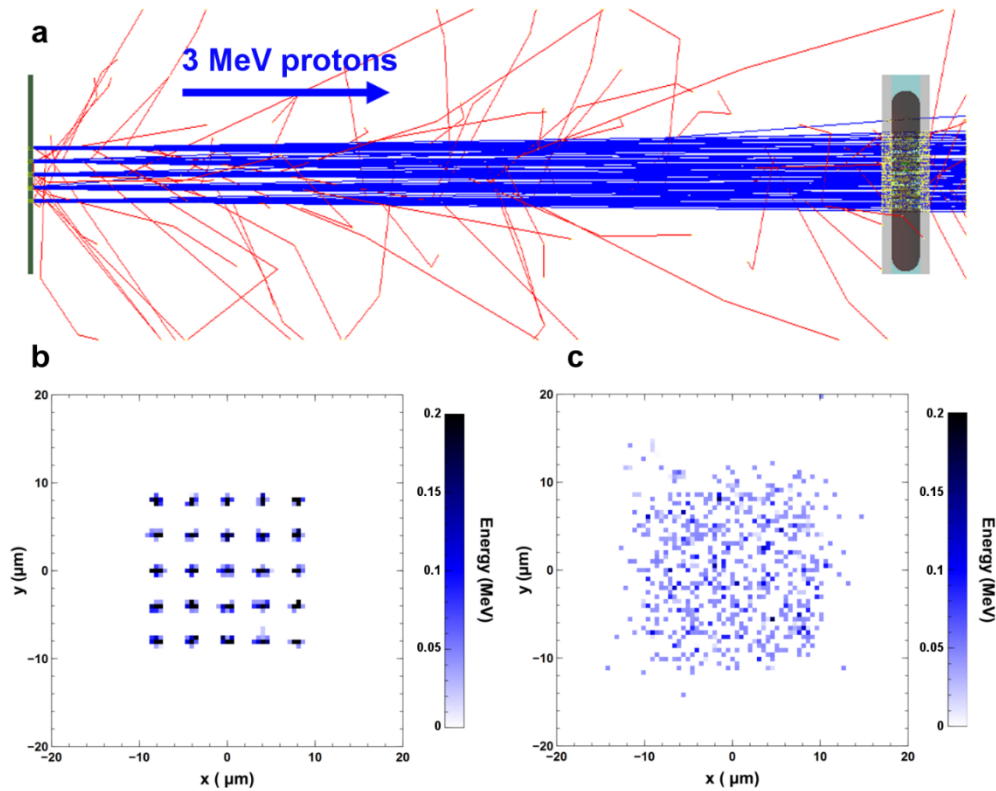


Fig. 41. **a.** Setup simulation of L1 larva irradiation in Geant4 irradiated with 3 MeV protons in the form of a 5 x 5 pattern with 5 protons/point. Their trajectories are represented by blue lines. The red lines show the trajectory of the secondary electrons generated. **b.** The energy distribution of protons at the entry of the first polypropylene foil when the sample is placed at 2 μm from the detector. The 5 x 5 points of the irradiation pattern are visibly spaced. **c.** The energy distribution of protons at the entry of the first polypropylene foil when the sample is placed at 350 μm from the detector. The protons reach the larva in a dispersed manner, delivering an almost homogeneous dose. The histograms binning is 0.5 μm.

To calculate the proton number per point for the different doses, I used an elementary area of 16 μm² (4 μm x 4 μm). The fluence, F , value, the number of protons per point and the total number of delivered protons calculated for each specific energy are summarized in the table 3.

<i>Specific energy (Gy)</i>	<i>F (p/μm²)</i>	<i>Number of p/point</i>	<i>Total number of p</i>
0.3	0.1589	16x $F = 2$	5 x 5x 2 = 50
3	1.589	16 x $F = 25$	5 x 5 x 25 = 625
30	15.89	16 x $F = 254$	6350

Table 3. Summary of the calculated data on simple geometric shapes of *C. elegans* L1 larva.

After choosing the optimum configuration (Fig. 40) to irradiate the zone around the 2 somatic gonad precursor cells with a homogeneous dose, we tested the irradiation with the 16 μm x 16 μm pattern on *C. elegans* GZ264 strain L1 larva (Fig.42). Even though the larvae were fixed during irradiation on agarose pads, movements especially in the tail were observed.

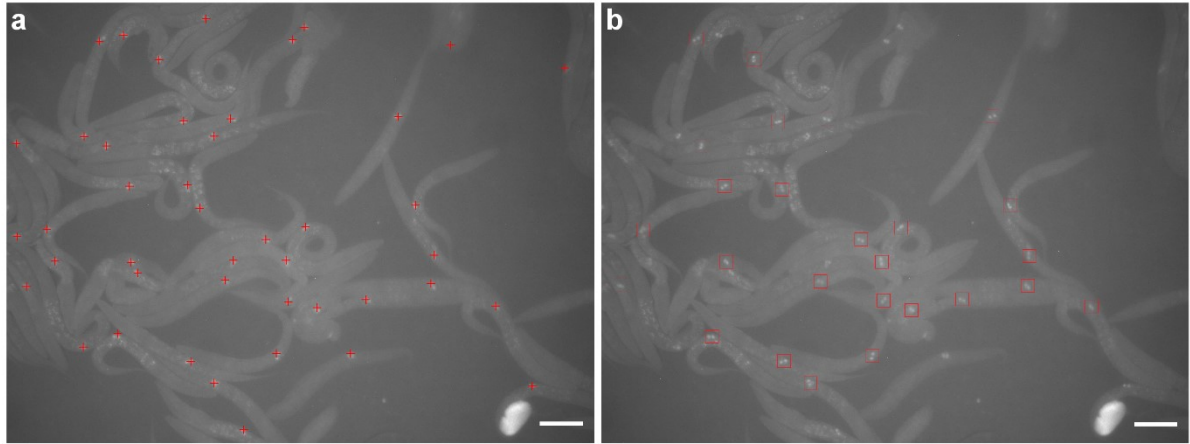


Fig. 42. Microscopic fluorescence image acquisition of *C. elegans* GZ264 strain L1 larva with the expression of GFP::PCN-1 that marks the 2 somatic gonad precursor cells. **a.** The red crosses correspond to the barycenter of the irradiation pattern. **b.** The red squares correspond to the irradiated zone around the 2 somatic gonad precursor cells. Scale bar = 50 μm .

Discussion

Laser micro-irradiation and CPM techniques have been widely used within the scope of radiobiological studies for their capability to induce localized damages in cellular or sub-cellular compartments³⁹. For over 40 years, laser microirradiation offers a powerful tool for targeted cellular damage with a range of wavelengths allowing the induction of specific damages such as SSBs, base lesions and DSBs. The advantage in performing such irradiations is that the same microscope equipped with suitable laser and optics can be used for the irradiation and the visualization of the cells⁴⁰. CPM irradiation is more complex to be performed since the observation of the cells and their irradiation cannot be done with the same equipment. However, their advantage relies on their ability to control both target irradiations and delivered dose in term of number of particles down to a single particle, which make their contributions very important in radiobiological study.

In this work, single cell nucleus in a developing multi-cellular organism, 2-cell stage *C. elegans* embryos were selectively irradiated and followed-up cell divisions by time-lapse imaging. DNA damages are visualized as radiation-induced foci with the HUS-1::GFP protein of the WS1433 strain in the irradiated nucleus. Chromosome instability were also observed, which results in chromosomal bridge during mitosis causing temporal and morphological disorganization of the irradiated embryo for the 2 strains MG152 (H2B::GFP) and GZ264(GFP::PCN-1). These effects were showed for the first cell division in *C. elegans* early stage embryos. Interestingly, these consequences are also observed in the daughter cells of the irradiated cell nucleus for the 3 strains, indicating a transmission of altered DNA through the division.

Based on the microdosimetric study developed during my PhD, the generation of DNA bridges and genomic instability observed experimentally require an ED in the chromatin of at least 4 pJ after irradiations with 10^4 protons. Micro-irradiations with lowest specific energy (10^3 protons), do not systematically produces the same visible damages. This could be due to the limited sensitivity of our fluorescent markers or the lack of specificity for the detection of the radiation-induced damage or the existence of a dose-threshold below it no sufficient radiation-induced effect would be produced on genomic DNA during the first cell division of AB. Based on the simulation in 3D phantoms of the ED in the embryo compartments (chromatin and nucleus), we clearly observed that, (i) no ED is found in the non-targeted nucleus and cell (P1); (ii) the biological effects appear at rather high specific energies, *i.e.* 180

Gy in the chromatin of the targeted nucleus (AB); (iii) the fraction of energy imparted to the chromatin shows large fluctuations considering the chromatin condensations in various phases of the division, going from only 4 % in prophase to about 60 % in metaphase, (iv) limited variations in terms of ED in the chromatin, depending on its condensation states, is expected between samples at the time of irradiation.

As a first step, high doses irradiations were performed to clearly observe direct effects. Nevertheless, this approach opens perspectives for selective irradiation at lower doses (down to one particle / cell) of specific cells in an organism in development.

Since only 4 % of the ED in the nuclear volume is imparted to the chromatin, the use of other *C. elegans* strains that mark other nuclear compartment is important to study the effect of IRs in these compartments. For instance, the SA250 strain expressing the histone H2B and the tubulin- γ associated to the red fluorescent protein mCherry marks the chromosomes, and the tubulin- β coupled to GFP marks the microtubules that form the mitotic spindle⁴¹.

In addition, using such *C. elegans* strain allows the Monte Carlo simulation in the realistic phantoms to be extended in more compartments in the embryo cells. To improve the calculation in such micro-cellular compartments, image acquisition with super-resolution microscopy such confocal STED (Stimulated emission depletion) microscopy can be used.

The calculation of the ED and the specific energy in the cell compartments can be extended to new geometries including the DNA structure and composition in the framework of the Geant4-DNA project⁴². This enhances the prediction of DNA damage including SSBs and DSBs induced by direct effect on the DNA molecules or indirect effects caused by free-radical species after radiolysis of water surrounding the cell DNA⁴³.

For the study of chronic induced stress response of *C. elegans* L1 larva, CPM irradiations in a regular pattern of 16x16 μm formed of 5x5 points with a Gaussian beam having FWHM of 4 μm allow delivering a homogeneous energy distribution into the zone around the 2 somatic gonad precursor cells. However, the irradiations were limited by the fixation problem of the larvae that moved during irradiation. Several techniques provide an efficient immobilization of the larvae such as the hydrogel for a gentle, rapid, inexpensive way to immobilize the *C. elegans* larva for continuous long-term experiments⁴⁴ and microfluidic tool for a fast and controlled microbeam irradiation of multiple samples in parallel¹¹.

References

1. Durante, M. & Friedl, A. A. New challenges in radiobiology research with microbeams. *Radiat. Environ. Biophys.* **50**, 335–338 (2011).
2. Griffith, L. G. & Swartz, M. A. Capturing complex 3D tissue physiology in vitro. *Nat. Rev. Mol. Cell Biol.* **7**, 211–224 (2006).
3. Barberet, P. & Seznec, H. Advances in microbeam technologies and applications to radiation biology. *Radiat. Prot. Dosimetry* **166**, 182–187 (2015).
4. Belyakov, O. V *et al.* Biological effects in unirradiated human tissue induced by radiation damage up to 1 mm away. *PNAS* **102**, 14203–14208 (2005).
5. Merz, F. *et al.* Tissue slice cultures from humans or rodents: a new tool to evaluate biological effects of heavy ions. *Radiat. Environ. Biophys.* **49**, 457–462 (2010).
6. Fukamoto, K. *et al.* Development of the Irradiation Method for the First Instar Silkworm Larvae Using Locally Targeted Heavy-ion Microbeam. *J. Radiat. Res* **48**, 247–253 (2007).
7. Choi, W. V. Y. *et al.* Adaptive Response in Zebrafish Embryos Induced Using Microbeam Protons as Priming Dose and X-ray Photons as Challenging Dose. *J. Radiat. Res* **51**, 657–664 (2010).
8. Choi, W. V. Y. *et al.* Triphasic Low-dose Response in Zebrafish Embryos Irradiated by Microbeam Protons. *J. Radiat. Res* **53**, 475–481 (2012).
9. Sugimoto, T. *et al.* Cell cycle arrest and apoptosis in *Caenorhabditis elegans* germline cells following heavy-ion microbeam irradiation. *Int. J. Radiat. Biol.* **82**, 31–38 (2006).
10. Bertucci, A., Pocock, R. D., Randers-Pehrson, G. & Brenner, D. J. Microbeam irradiation of the *C. elegans* nematode. *J. Radiat. Res.* **50**, A49–A54 (2009).
11. Buonanno, M. *et al.* Microbeam irradiation of *C. elegans* nematode in microfluidic channels. *Radiat. Environ. Biophys.* **52**, 531–537 (2013).
12. Takanami, T. *et al.* Efficient repair of DNA damage induced by heavy ion particles in meiotic prophase I nuclei of *Caenorhabditis elegans*. *J. Radiat. Res* **44**, 271–6 (2003).

13. Suzuki, M. *et al.* Region-specific irradiation system with heavy-ion microbeam for active individuals of *Caenorhabditis elegans*. *J. Radiat. Res.* **58**, 881–886 (2017).
14. Vianna, F. Micro-irradiation ciblée par faisceau d'ions pour la radiobiologie in vitro et in vivo. (Université de Bordeaux, 2015).
15. Barberet, P. *et al.* Development of a focused charged particle microbeam for the irradiation of individual cells. *Rev. Sci. Instrum.* **76**, (2005).
16. ICRU Report 60. *Fundamental Quantities and Units of Ionizing Radiation (International Commission on Radiation Units and Measurements, Bethesda, MD)*. (1998).
17. ICRU Microdosimetry Report 36. *Bethesda, MD: International Commission on Radiation Units and Measurements*. (1983).
18. Nikjoo, H., Uehara, S., Emfietzoglou, D. & Cucinotta, F. A. Track-structure codes in radiation research. *Radiat. Meas.* **41**, 1052–1074 (2006).
19. Beaton, L. A., Burn, T. A., Stocki, T. J., Chauhan, V. & Wilkins, R. C. Development and characterization of an in vitro alpha radiation exposure system. *Phys. Med. Biol.* **56**, 3645–3658 (2011).
20. Roeske, J. C. & Hoggarth, M. Alpha-particle Monte Carlo simulation for microdosimetric calculations using a commercial spreadsheet. *Phys. Med. Biol.* **52**, 1909–1922 (2007).
21. Douglass, M., Bezak, E. & Penfold, S. Development of a randomized 3D cell model for Monte Carlo microdosimetry simulations. *Med. Phys.* **39**, 3509–3519 (2012).
22. Incerti, S. *et al.* Monte Carlo dosimetry for targeted irradiation of individual cells using a microbeam facility. *Radiat. Prot. Dosimetry* **133**, 2–11 (2009).
23. Miller, J. H., Chrisler, W. B., Wang, X. & Sowa, M. B. Confocal microscopy for modeling electron microbeam irradiation of skin. *Radiat. Env. Biophys.* **50**, 365–369 (2011).
24. Barberet, P. *et al.* Monte-Carlo dosimetry on a realistic cell monolayer geometry exposed to alpha particles. *Phys. Med. Biol.* **57**, 2189–2207 (2012).
25. Incerti, S. *et al.* the Geant4-Dna Project. *Int. J. Model. Simulation, Sci. Comput.* **01**,

- 157–178 (2010).
26. Gilbin, R., Alonzo, F. & Garnier-Laplace, J. Effects of chronic external gamma irradiation on growth and reproductive success of *Daphnia magna*. *J. Environ. Radioact.* **99**, 134–145 (2008).
27. Adam-Guillermin C, Pereira S, Della-Vedova C, Hinton T, G.-L. J. in *Reviews of Environmental Contamination and Toxicology* 67–103 (Springer, New York, NY, 2012). doi:10.1007/978-1-4614-3414-6_3
28. Buisset-Goussen, A. *et al.* Effects of chronic gamma irradiation: A multigenerational study using *Caenorhabditis elegans*. *J. Environ. Radioact.* **137**, 190–197 (2014).
29. Lecomte-Pradines, C. *et al.* A dynamic energy-based model to analyze sublethal effects of chronic gamma irradiation in the nematode *Caenorhabditis elegans*. *J. Toxicol. Environ. Heal. - Part A Curr. Issues* **80**, 830–844 (2017).
30. Hofmann, E. R. *et al.* *Caenorhabditis elegans* HUS-1 is a DNA damage checkpoint protein required for genome stability and EGL-1-mediated apoptosis. *Curr. Biol.* **12**, 1908–1918 (2002).
31. Brauchle, M., Baumer, K. & Gonczy, P. Differential Activation of the DNA Replication Checkpoint Contributes to Asynchrony of Cell Division in *C. elegans* Embryos Michael. *Curr. Biol.* **28**, 819–827 (2003).
32. Kisielewska, J., Lu, P. & Whitaker, M. GFP-PCNA as an S-phase marker in embryos during the first and subsequent cell cycles. *Biol. Cell* **97**, 221–229 (2005).
33. Incerti, S., Douglass, M., Penfold, S., Guatelli, S. & Bezak, E. Review of Geant4-DNA applications for micro and nanoscale simulations. *Phys. Medica* **32**, 1187–1200 (2016).
34. Strome, S. *et al.* Spindle dynamics and the role of gamma-tubulin in early *Caenorhabditis elegans* embryos. *Mol. Biol. Cell* **12**, 1751–1764 (2001).
35. Susanne Kaitna*, Manuel Mendoza*, V. J.-P. and M. G. Incenp and an Aurora-like kinase form a complex essential for chromosome segregation and efficient completion of cytokinesis. *J. Biochem.* **10**, 1172–1181 (2000).
36. Walsh, D. W. M. *et al.* Live cell imaging of mitochondria following targeted irradiation in situ reveals rapid and highly localized loss of membrane potential. *Sci. Rep.* **7**, 46684

- (2017).
37. Sonnevile, R., Querenet, M., Craig, A., Gartner, A. & Julian Blow, J. The dynamics of replication licensing in live *Caenorhabditis elegans* embryos. *J. Cell Biol.* **196**, 233–246 (2012).
 38. Torfeh, E. *et al.* Monte-Carlo dosimetry and real-time imaging of targeted irradiation consequences in 2-cell stage *Caenorhabditis elegans* embryo. 1–12 (2019). doi:10.1038/s41598-019-47122-7
 39. Drexler, G. A. & Ruiz-Gómez, M. J. Microirradiation techniques in radiobiological research. *J. Biosci.* **40**, 629–643 (2015).
 40. Koury, E., Harrell, K. & Smolikove, S. Differential RPA-1 and RAD-51 recruitment in vivo throughout the *C. elegans* germline, as revealed by laser microirradiation. *Nucleic Acids Res.* **46**, 748–764 (2018).
 41. Toya, M., Iida, Y. & Sugimoto, A. Imaging of Mitotic Spindle Dynamics in *Caenorhabditis elegans* Embryos. *Methods Cell Biol.* **97**, 359–372 (2010).
 42. Lampe, N. *et al.* Mechanistic DNA damage simulations in Geant4-DNA part 1: A parameter study in a simplified geometry. *Phys. Medica* **48**, 135–145 (2018).
 43. Lampe, N. *et al.* Mechanistic DNA damage simulations in Geant4-DNA Part 2: Electron and proton damage in a bacterial cell. *Phys. Medica* **48**, 146–155 (2018).
 44. Burnett, K., Edsinger, E. & Albrecht, D. R. Rapid and gentle hydrogel encapsulation of living organisms enables long-term microscopy over multiple hours. *Commun. Biol.* **1**, (2018).

Publication

« Monte-Carlo dosimetry and real-time imaging of targeted irradiation consequences in 2-cell stage *Caenorhabditis elegans* embryo »

Torfeh, E. *et al.* Monte-Carlo dosimetry and real-time imaging of targeted irradiation consequences in 2-cell stage *Caenorhabditis elegans* embryo. *Sci. Rep.* **9**, 10568; doi: 10.1038/s41598-019-47122-7

SCIENTIFIC REPORTS

OPEN

Monte-Carlo dosimetry and real-time imaging of targeted irradiation consequences in 2-cell stage *Caenorhabditis elegans* embryo

Received: 21 March 2019
Accepted: 11 July 2019
Published online: 22 July 2019

Eva Torfeh^{1,2}, Marina Simon^{1,2}, Giovanna Muggiolu^{1,2}, Guillaume Devès^{1,2}, François Vianna^{1,2,3}, Stéphane Bourret^{1,2}, Sébastien Incerti^{1,2}, Philippe Barberet^{1,2} & Hervé Seznec^{1,2}

Charged-particle microbeams (CPMs) provide a unique opportunity to investigate the effects of ionizing radiation on living biological specimens with a precise control of the delivered dose, *i.e.* the number of particles per cell. We describe a methodology to manipulate and micro-irradiate early stage *C. elegans* embryos at a specific phase of the cell division and with a controlled dose using a CPM. To validate this approach, we observe the radiation-induced damage, such as reduced cell mobility, incomplete cell division and the appearance of chromatin bridges during embryo development, in different strains expressing GFP-tagged proteins *in situ* after irradiation. In addition, as the dosimetry of such experiments cannot be extrapolated from random irradiations of cell populations, realistic three-dimensional models of 2 cell-stage embryo were imported into the Geant4 Monte-Carlo simulation toolkit. Using this method, we investigate the energy deposit in various chromatin condensation states during the cell division phases. The experimental approach coupled to Monte-Carlo simulations provides a way to selectively irradiate a single cell in a rapidly dividing multicellular model with a reproducible dose. This method opens the way to dose-effect investigations following targeted irradiation.

Charged-particle microbeams (CPMs) present unique features for radiation biology studies: they allow the targeting of sub-cellular compartments with micrometre accuracy, to set a definite irradiation timing and a precise dose control at the single-cell scale^{1–3}. In the last decades, CPMs have been extensively used to study several biological endpoints in single cells such as DNA damage and repair mechanisms, cell communication (bystander effect), low-dose effects, and radiation sensitivity of cell compartments (nucleus, cytoplasm, and mitochondria)^{4–6}.

Although data from *in vitro/in cellulo* experiments on monolayer cell culture are very useful to dissect the molecular mechanisms induced by the exposure to ionizing radiation (IR), they are difficult to extrapolate to the *in vivo* response. For this reason, there is a growing interest in applying CPM irradiation techniques to *ex vivo* and *in vivo* biological models. CPMs have been gradually extended to the irradiation of three-dimensional tissue models and small multicellular *in vivo* systems to overcome these limitations^{6–10}. Well-characterized biological models, such as the zebrafish *Danio rerio* embryo^{11,12}, the *Bombyx mori* silkworm¹³, and the nematode *Caenorhabditis elegans* (*C. elegans*)^{14,15}, are also compatible with the limited range of the particles used by CPMs. Among these models, *C. elegans* presents numerous advantages for *in vivo* investigation of radiation effects: simple culture conditions and maintenance, a rapid life cycle, a transparent body, an adult organism with only 959 somatic cells and invariant cell lineage between different animals. Moreover, *C. elegans* provides a highly characterized whole organism model where changes in genes, cells and tissues, during development is precisely defined. A wide variety of fully characterized mutants and transgenic strains is available at the *C. elegans* Genome Center (CGC).

¹Université de Bordeaux, Centre d'Etudes Nucléaires Bordeaux Gradignan (CENBG), Chemin du Solarium, 33175, Gradignan, France. ²CNRS, UMR5797, Centre d'Etudes Nucléaires Bordeaux Gradignan (CENBG), Chemin du Solarium, 33175, Gradignan, France. ³Present address: François Vianna: Institut de Radioprotection et de Sécurité Nucléaire, Bat.159, BP3, 13115, St-Paul-Lez-Durance, Cedex, France. Correspondence and requests for materials should be addressed to P.B. (email: barberet@cenbg.in2p3.fr) or H.S. (email: herve.seznec@cenbg.in2p3.fr)

Several studies of radiation-induced responses have been carried out using X and γ -Rays irradiation of *C. elegans*. Deng *et al.* have established a relation between the ceramide biogenesis pathway and the radiation-induced apoptosis in the germ line of *C. elegans*¹⁶. Using X-rays, Sandoel *et al.* have found that HIF-1 can regulate p53-mediated apoptotic cell death in response to radiation-induced damage through the secretion of a neuronal tyrosinase¹⁷. *C. elegans* has also been used as a biological model for space flight research, including testing the biological effects of cosmic radiation¹⁸.

From a practical point of view, *C. elegans* is small enough to be compatible with microbeam irradiation since the adult body is 50 μm in diameter and 1 mm in length. Its transparent body allowing a direct visualization of specific tissues makes it a unique model for studying the production and transfer of intra- and inter-tissue damage signalling in the whole organism. A few studies have described the use of *C. elegans* at CPM end-stations^{14,15,19}. Guo *et al.* have reported that irradiation of the somatic pharynx results in a significant induction of bystander germ cell apoptosis²⁰. Li Q *et al.* have performed local irradiation of either the posterior pharynx or the vulva of *C. elegans* as a comparison of the intra- and inter-system bystander effects, and investigated the spatial function of the oxidative DNA damage response by tissue-specific RNA interference²¹.

We report here the selective irradiation of 2-cell stage *C. elegans* embryos using the CPM at the AIFIRA facility (Applications Interdisciplinaires de Faisceaux d'Ions en Région Aquitaine)²². The aim of this study was to develop a methodology to micro-irradiate in a reproducible way the 2-cell stage *C. elegans* embryos with protons. Such a micro-irradiation of a dynamic 3D biological model with a fast cell division and rapidly evolving target volumes raises experimental challenges. The validation of this procedure includes an experimental validation of our ability to reproducibly induce radiation damage in embryos. Besides, Monte Carlo simulation on realistic 2-cell stage *C. elegans* phantoms was performed to characterize the specific energy absorbed in different biological compartments (chromatin, nucleus, cytoplasm and whole embryo), while considering different condensation states of chromatin throughout the cell division.

Results

Embryo phantom generation for monte carlo dosimetry simulation. When targeting sub-cellular structures with a microbeam, the radiation dose is delivered in micrometric areas. Standard dosimetry methods, based on the calculation of the absorbed dose at the macroscopic scale, are not fully relevant in this configuration. The spatial inhomogeneity of the irradiation leads to difficulties in defining the volume of interest, and the concept of absorbed dose is of limited use. In such situations, ICRU (International Commission on Radiation Units and Measurements) has introduced the concept of specific energy, defined as the ratio of the energy imparted to the mass of the volume of interest²³. As the energy deposited by charged-particles depends significantly on the geometry of the target, we developed a three-dimensional realistic voxelized model of a 2-cell stage embryo. The energy deposits in 3 compartments were determined in our dosimetric study: (i) the chromatin, (ii) the nuclear volume, and (iii) the whole embryo. The geometries of these compartments were built from confocal microscopy acquisition of paraformaldehyde-fixed embryos. Phalloidin staining reveals the actin cytoskeleton of the 2-cell stage embryo in red (Fig. 1a) and Hoechst³³³⁴² staining revealed the chromatin in blue (Fig. 1b). As Phalloidin stains the actin-cytoskeleton which is absent in the nucleus, the nuclear volume is indirectly outlined by manual selection based on contrast rendering and cropping the area outside the region of interest (ROI). This ROI was then set as the green channel and the outside region was masked and left out from further processing (Fig. 1c). The resulting numeric phantom of a 2-cell stage was then implanted in Geant4 as a parametrized volume as shown in Fig. 1d. The microbeam spot size was set to 1.5 μm at the target (AB cell nucleus) position.

The methodology described previously by Barberet *et al.*²⁴ was used to determine the energy imparted in each compartment as well as its distribution in space (Fig. 1e). The data obtained using this approach are summarized in Table 1. We calculated the corresponding specific energy as the ratio of the total energy deposit to the sum of the masses of voxels constituting the target (chromatin, nucleus or embryo). The mass of the different compartments was extrapolated by multiplying the sum of voxel volume constituting each compartment by liquid water density. We noted that the energy is deposited exclusively in the irradiated nucleus AB. The non-irradiated nucleus P1 does not receive any energy deposit (Fig. 1e). The statistical uncertainties related to the Monte-Carlo simulation are below 2%.

Since cell division is a rather fast process in *C. elegans* embryos as illustrated in Fig. 2a, we investigated the impact of the DNA/chromatin condensation level on the energy imparted to the chromatin (Fig. 2a). For this purpose, 40 single cells within 2-cell stage embryos were simulated after irradiations with 10^3 3 MeV protons. Based on the chromatin condensation status throughout the cell cycle progression of the AB cell ($t = 0$ to 4 min), 5 distinct chromatin distributions could be discriminated from confocal imaging (Fig. 2b). They are representative of distinct mitosis progression states. The calculated energy imparted to the chromatin is different depending on the chromatin distribution observed in prophase or metaphase (Fig. 2b).

Nevertheless, as illustrated by these results, even if some variation of the chromatin distribution is found in prophase, it does not affect drastically the energy deposit in the chromatin at the irradiation time (0.5 ± 0.15 pJ). This point is crucial in the context of the dose-response assessment of biological radiation-induced effect. In addition, as illustrated in Fig. 2c, the calculated energy deposit in the 40 embryonic cell nuclei is around 10.5 ± 2.8 pJ per nucleus (± 3.8 as 95% Confidence Interval (IC)). This 25% fluctuation is related to the variation of the nuclear volume from one embryo to the next. Indeed, the mean nuclear thickness traversed by the incoming protons was evaluated to 6 μm with a variation of 1.5 μm . Despite the additional uncertainties due to the manual segmentation of the nuclear volume, this is confirmed by the 2D fluorescence images of the GZ264 strain. We observed that the nucleus diameter can vary from 6.5 to 8.5 μm depending on the cell cycle stage. Assuming a spherical shape, this corresponds to a 25% variation of the nucleus thickness. Note that if we consider the total energy imparted to the nuclear volume, only 4% of this energy is absorbed by the chromatin in prophase (Table 1). This ratio can increase up to 60% in metaphase.

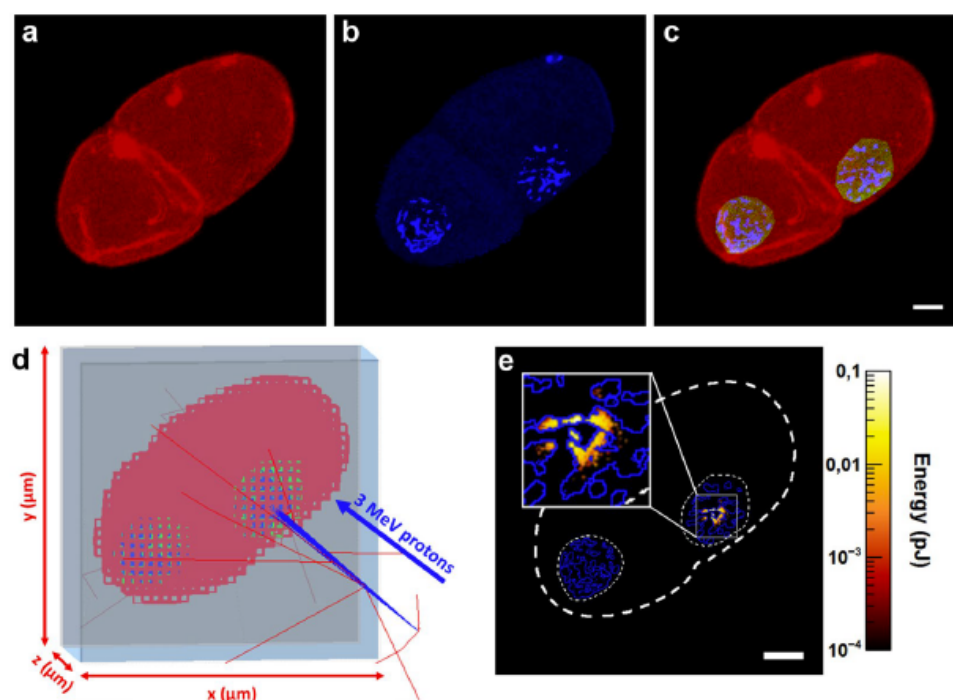


Figure 1. Monte-Carlo dosimetry and calculation of the energy deposit in 2-cell stage *C. elegans* embryo. (a,b) Confocal images of a 2-cell stage embryo stained with phalloidin (red) and Hoechst²³³⁴² (blue). (c) The chromatin (blue) and the embryo (red) are identified by applying an intensity threshold to separate fluorescent objects (chromatin) from the background. The nuclear volume (green) is outlined manually. (d) Voxelized geometry in Geant4 (low resolution) irradiated with 3 MeV protons. The incident protons are represented by blue lines, the red lines illustrate the trajectory of secondary electrons generated in air. (e) Z-projection of the energy deposit calculated using Geant4-DNA after irradiation with 10^3 protons. The dashed outline corresponds to the contouring projection of the 3 volumes (chromatin in blue, nucleus and whole embryo in white). Scale bar: 5 μm .

	Energy deposit per proton (fJ)	Mass (kg)	Specific energy per proton (mGy)
Chromatin	0.38 ± 0.01	2.2×10^{-14}	18.2
Nuclear volume	9.47 ± 0.08	2.1×10^{-13}	45.2
Whole embryo	29.77 ± 0.22	1.3×10^{-11}	2.3

Table 1. Summary of the calculated and simulated data on realistic 3D-rendering of a 2-cell stage *C. elegans* embryo. The data shown in the table are obtained from calculations in the *C. elegans* embryo in Fig. 1. The reported energy deposits are mean values \pm standard deviations. These statistical uncertainties are related to the Monte Carlo calculations and they are below 2%.

Selective and targeted irradiation reveals HUS-1::GFP nuclear foci. We adapted well-established CPM irradiation techniques previously developed for *in vitro* culture studies²⁴. Embryos, prepared as described in Fig. 3a, were kept in M9 medium between two stretched polypropylene foils. The chosen foils are thin enough (4 μm) to allow the charged-particles to traverse through the sample and be detected downstream (Fig. 3b). This procedure resulted in the reproducible placement of the embryos in the focal plane of the objective lens. Under such conditions, we found that the slight compression of the polypropylene foils has no significant effect on the first cellular divisions. *C. elegans* embryos undergo fast, cleavage-type divisions in which the cell volume decreases after every cell division. The cell cycle in the early embryo stages is only composed of consecutive rounds of DNA synthesis (S phase) and cell division during mitosis (M phase), with no gap phase until the 28-cell stage^{25,26}. The 2-cell stage embryos are formed of a larger anterior blastomere, AB, and a smaller posterior blastomere, P1, which have different fates and cell division timings; AB is divided 2 min before P1²¹. AB and P1 are oriented along the anteroposterior axis (Fig. 3c). In our experimental conditions, the first cellular divisions were found to be similar to the ones observed in conventional experimental conditions with *C. elegans* zygote exhibiting rotational holoblastic cleavage. We chose to irradiate selectively and specifically the nucleus of the AB cell. This corresponds to time 0 of our time lapse recording ($t = 0 \text{ min}$).

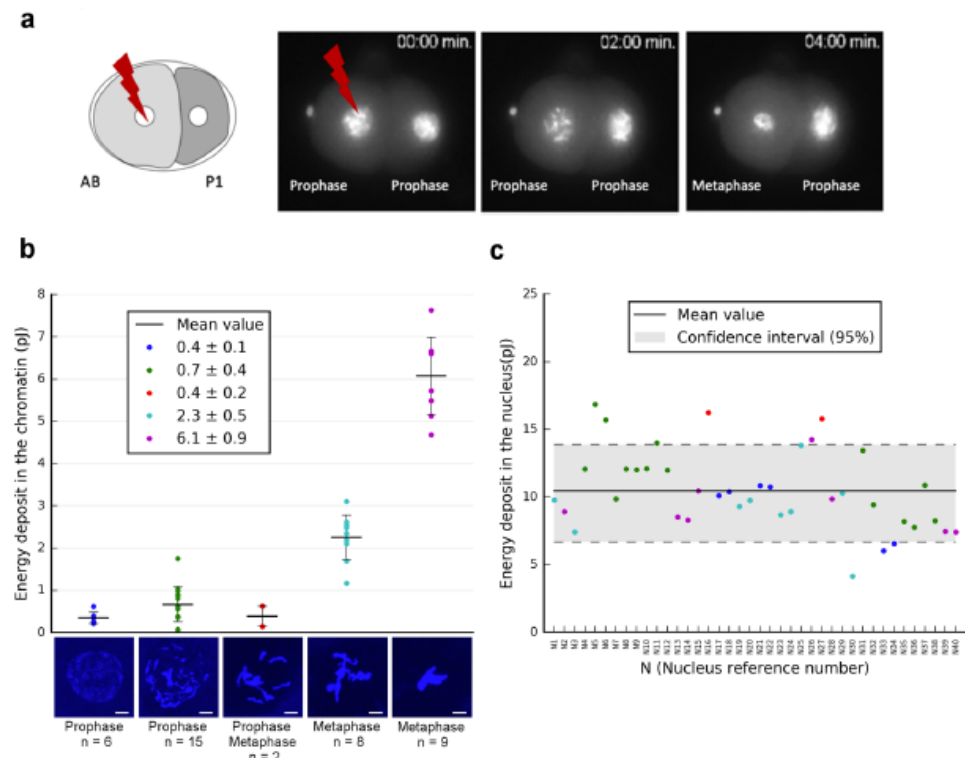


Figure 2. Monte-Carlo dosimetry and calculation of the energy deposit in the chromatin and nucleus. (a) First cell division of 2-cell stage embryos using strains expressing the histone H2B::GFP that revealed the chromatin condensation state at irradiation time. (b) Calculation of the total energy deposit (for 10^3 protons) in the chromatin depending on its condensation status during the mitosis. 2D-projections of 5 different chromatin distributions revealed by Hoechst³³³⁴² (blue) and recorded in 40 embryonic cells by confocal microscopy. Scale bar: 3 μ m. (c) Total energy deposit in the nucleus calculated using the same methodology described above for 40 embryonic cells (with 10^3 protons). The scatter-plot point colours represent the corresponding chromatin condensation state colours from (b).

In order to obtain a direct visualization of the radiation-induced DNA damage in the *C. elegans* embryo, we used the WS1433 (*opIs34[hus-1::GFP]*) strain. In *C. elegans*, HUS-1 is a conserved nuclear protein that is expressed in early embryos and the adult germline. In proliferating embryo nuclei, HUS-1::GFP expression is low, homogeneously distributed and limited to the nucleus as shown in Fig. 4 (Control). HUS-1 is part of the 9:1:1 complex belonging to DNA damage checkpoint protein acting as a DNA damage sensor. Thus, it is required for DNA damage-induced cell cycle arrest and apoptosis²⁷ and is essential for genome stability, as demonstrated by an increased frequency of spontaneous mutations, chromosome non-disjunction, and telomere shortening²⁸. When DNA damage occurs, HUS-1 is relocated into the nucleus in distinct foci that overlap chromatin. These foci are likely sites of double-strand breaks (DSBs). Following targeted micro-irradiation with 10^4 protons, HUS-1::GFP relocated swiftly and formed a distinct and bright focus at the site of irradiation (Fig. 4, Supplementary Videos S1 and S2). However, we observed some variability between the nuclei in terms of diameter and number of foci per nucleus. HUS-1::GFP foci were maintained during the mitotic division and found in the daughter cell nuclei ABa and ABp. HUS-1::GFP foci were only detected for the highest irradiation specific energy (180 Gy/chromatin) in 8/9 embryos (additional data are shown in Fig. S2) harbouring nuclear HUS-1::GFP foci (total of 9 irradiated embryos).

By contrast, we never observed the occurrence of HUS-1::GFP foci in non-irradiated nuclei and their vicinity (P1 and related daughter cells), as well as in control embryos and in irradiated embryos with the lowest specific energy. In addition, no HUS-1::GFP foci were detected when the embryos were irradiated with 10^3 protons (data not shown).

Consequences of the micro-irradiation on chromosomes in 2-cell stage embryo. The cellular consequences of targeted irradiation were followed using a strain (MG152) expressing the histone H2B::GFP fusion protein. This protein allows the imaging of both mitotic chromosomes and interphase chromatin in intact, living embryos. Embryos expressing H2B::GFP were observed using time-lapse imaging to determine the pattern of chromatin staining in interphase and mitosis after irradiation of the AB nucleus. As observed in control embryos, H2B::GFP enables highly sensitive chromatin detection in all phases of the mitosis. Figure 5a shows control embryos with chromosome condensation, the formation of a regular metaphase plate, a sudden and

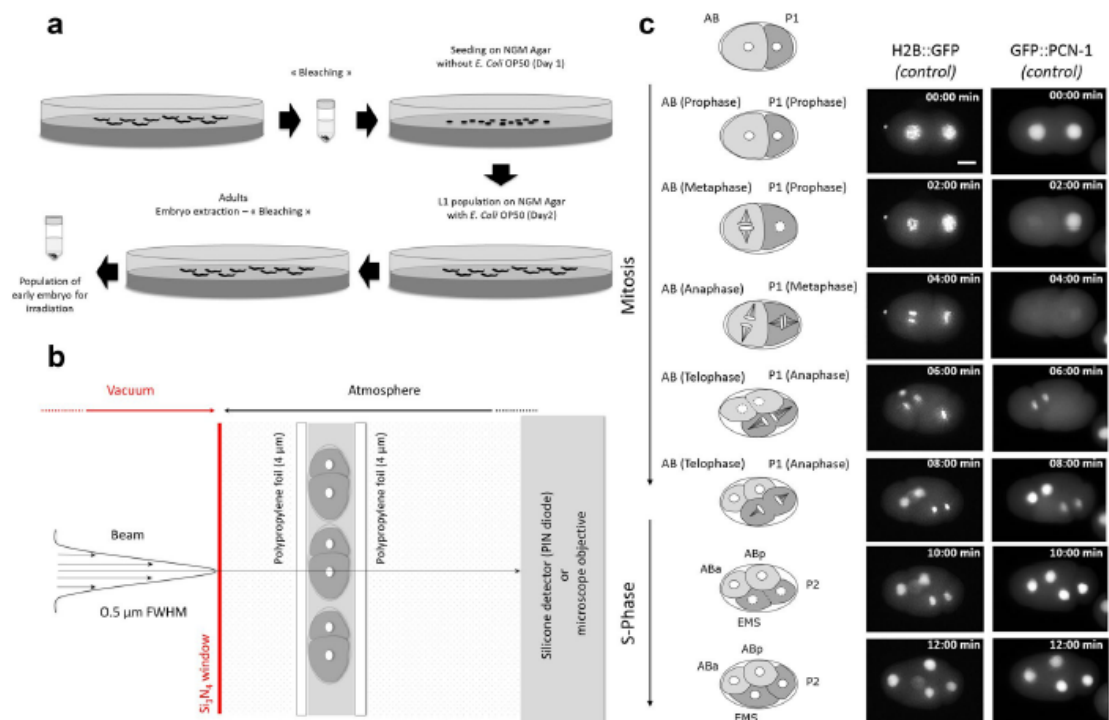


Figure 3. Schematic representation of the different steps needed for micro-irradiation of early *C. elegans* embryos in development. (a) Preparation of large populations of early *C. elegans* embryos by bleaching. (b) Scheme of the experimental end-station. The embryos are maintained between two thin polypropylene foils (4 μm in thickness) and the AB nucleus is targeted using online fluorescence microscopy. The beam is positioned on the targeted cell by means of electrostatic deflection and an exact number of protons is delivered and counted downstream the sample using a silicon detector. (c) Timing of cell division in early *C. elegans* embryo of MG152 (H2B::GFP) and GZ264 (GFP::PCN-1) strains. The nucleus is marked as a white circle in the middle of the cell. Asymmetric division of the P0 cell generates a larger, anterior AB cell and smaller, posterior P1 cell. Mitosis entry is indicated by nuclear breakdown (illustrated with dashed circle) and is accompanied by spindle rotation. Before cytokinesis of AB is completed, the posterior P1 cell enters mitosis (dashed circle). Cell divisions result in a four-cell embryo, with the daughter cells ABa and ABp derived from AB, and EMS and P2 derived from P1. Scale bar: 10 μm.

complete separation of anaphase chromosomes without the presence of chromatin bridges between daughter cells (ABa, ABp, EMS, and P2).

In contrast, in the irradiated embryos, abnormalities in chromosomal morphology became apparent during the first mitotic division of the AB cells, with chromosomes more poorly condensed than in non-irradiated embryos during anaphase (Fig. 5a, irradiation). In addition, H2B::GFP provided a remarkable level of sensitivity which allowed the detection of chromatin bridges. These are lagging strands of DNA between chromosomes that are separating during the mitotic phase and became obvious between the two daughter cells upon reaching the end of anaphase. These chromatin bridges remained until cytokinesis occurred, when the cell division broke them to produce a “cut” phenotype, resulting in the uneven distribution of genomic DNA to daughter cells. Chromatin bridges were clearly observed in all the embryos irradiated at the highest specific energy (5/5, additional data are shown in Fig. S3). The P1 blastomeric division, which occurs 2–3 minutes later, was normal; the chromosomes appeared well condensed in both controls and in irradiated embryos. No chromatin bridges were identified between the P1 daughter cells, and their nuclear morphology under epifluorescence was normal (Fig. 5, Supplementary Videos S3–S6).

Epifluorescence images of H2B::GFP embryos show the presence of one polar body at the anterior part of the embryo. Polar bodies are visible as small membrane-bound oval structures between the eggshell and the embryo, and are clearly visible with histone H2B::GFP in living embryos. The first polar body is 2N, born during eggshell secretion, and trapped between eggshell layers. The second polar body 1N is born after eggshell formation and is in contact with the embryo. At the 2-cell stage, the second polar body is on the surface of the anterior AB cell. During AB cell division, the second polar body is drawn between cells by the ingression furrow. At the 4-cell stage, the second polar body is inside a membrane within one of the AB daughter cells. In irradiated embryos, the presence of the chromatin bridges between the two daughter cells ABa and ABp affected and stopped the migration of one of the polar bodies until the cytokinesis occurred (Fig. 5a). Despite risking aneuploidy, *C. elegans* embryonic cells internalize the polar body and degrade polar body chromosomes inside a phagolysosome²⁹. Here, we showed that the fate of the polar bodies seems to be modified in presence of the DNA bridges.

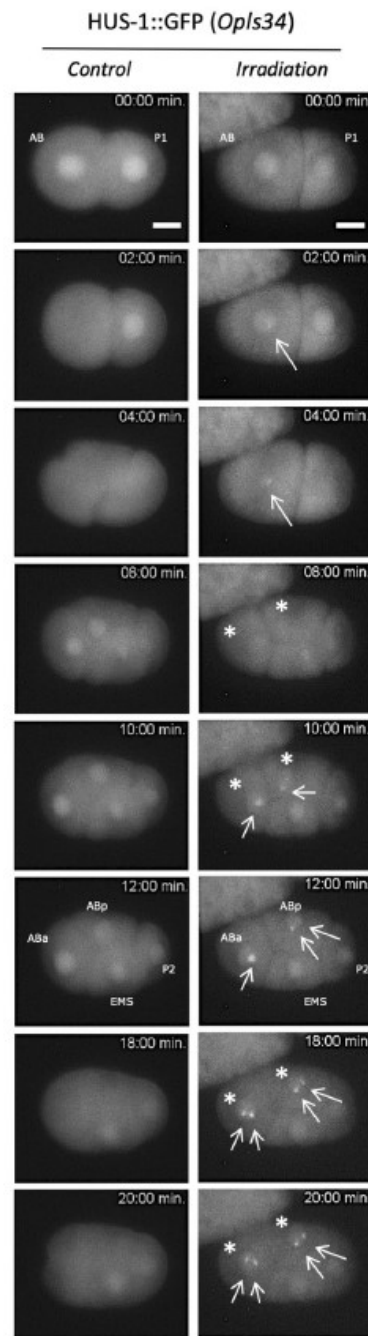


Figure 4. Real-time analysis of micro-irradiated AB nucleus revealed the subcellular relocalization of HUS-1::GFP (foci). First cell divisions of 2-cell stage embryos are observed using a strain expressing HUS-1::GFP (*opls34*). Before irradiation HUS-1::GFP is homogenously distributed in nuclei ($t = 0$ min). The AB cell nucleus is targeted with protons at $t = 0$ min. In micro-irradiated AB nucleus of HUS-1::GFP embryo, a focus, indicated with white arrow (→), appears just before the first cell division of AB ($t = 2$ min.) and reappears in the daughter cells ABa and ABp indicated with stars (*, right). We never observed foci in both non-irradiated embryo (control) and neighbouring non-irradiated nuclei (P1, EMS, and P2). Irradiated embryos (*opls34* = 10^4 protons) were observed in real time following irradiation. Scale bar: 10 μ m.

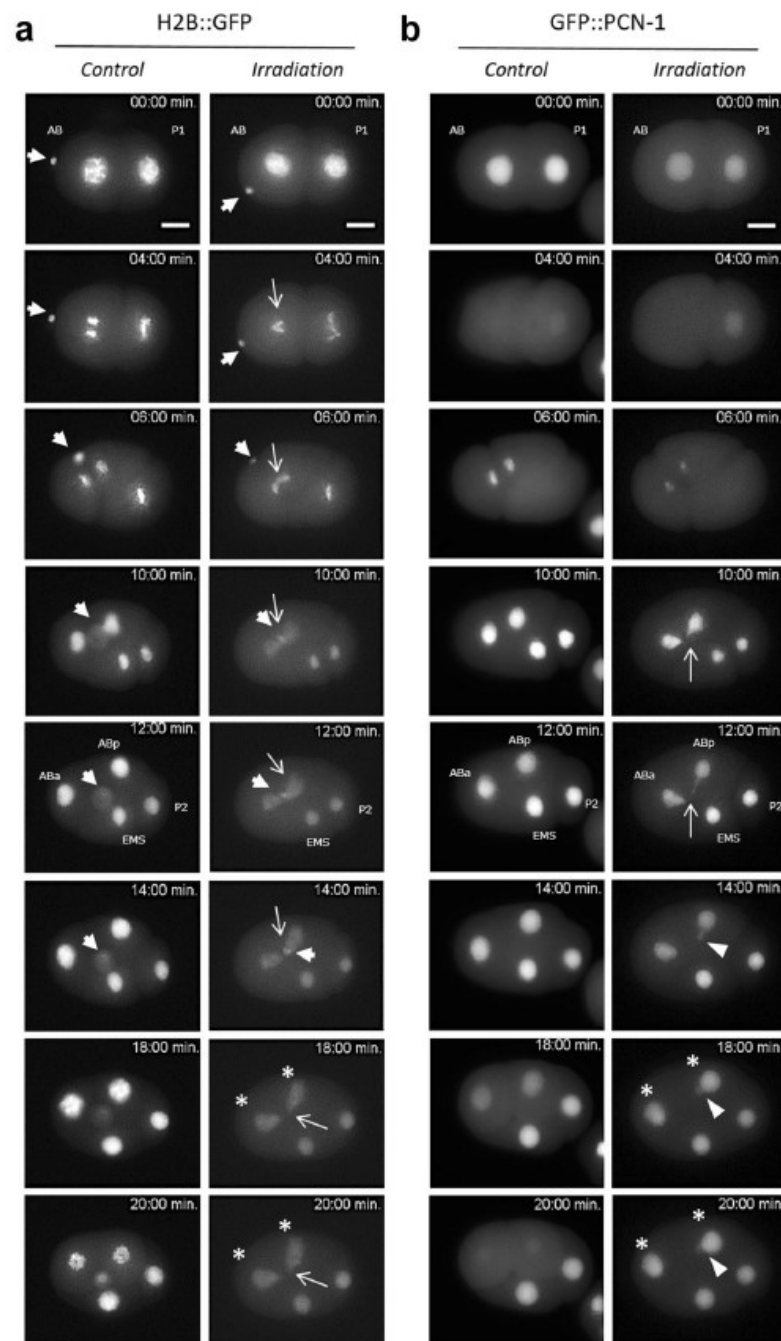


Figure 5. Time-lapse imaging of micro-irradiated AB nucleus revealed chromatin bridges and synchronization disruption of cell divisions within the 4-cell stage *C. elegans* embryos. First cell division of 2-cell stage embryos is observed using integrated strains expressing the histone H2B::GFP and GFP::PCN-1. Images are obtained at the same magnification. Scale bar 10 μ m. The nucleus of the AB cell is targeted with 10^4 protons at $t = 0$ sec (Irradiation). (a) H2B::GFP is bright and reveals the chromatin condensation during the different mitotic steps (Control). Note the presence of the polar bodies at the anterior part of the embryo (extranuclear H2B::GFP labelling, \rightarrow). In micro-irradiated nucleus, H2B::GFP allows for the visualization of *in situ* and real time formation of DNA bridges (\rightarrow) between the two dividing daughter cells ABa and ABp. Polar bodies are indicated with white arrows (\rightarrow) (b) In GZ264 embryos, the nuclear GFP::PCN-1 signals the S-phase and its loss suggests the nuclear membrane breakdown (mitosis). In the irradiated nucleus of GFP::PCN-1 embryo, the formation of DNA bridges during the first division can be clearly seen during the mitosis until their breakdown and the formation of extra-nuclear DNA (\blacktriangleright). Disruption of the cell division synchronization within the 4-cell

stage *C. elegans* embryo is also seen (*). The PCN-1::GFP signal helps to distinguish a clear shift of cellular division between irradiated and non-irradiated embryos (*). The formation of DNA bridges was never observed in non-irradiated nuclei (P1, EMS, P2) and/or non-irradiated embryos.

Real-time analysis of micro-irradiated nuclei reveals synchronization disruption of cell divisions within the 4-cell stage *C. elegans* embryos. The dynamics of DNA replication in the *C. elegans* 2-cell stage embryo were estimated with a transgenic strain expressing PCN-1, the *C. elegans* orthologue of PCNA (proliferating cell nuclear antigen)³⁰, fused to GFP. PCN-1 acts as a processivity factor for DNA replication and is one of the last components incorporated into the replisome upon replication initiation³¹. We used the GFP::PCN-1 chimera to visualize S-phase in early embryos and during subsequent cell or nuclear cycles. In other organisms, its accumulation in nuclear foci has been previously demonstrated to report on the active sites of DNA replication^{32,33}. In time-lapse epifluorescence images of developing 2-cell stage embryos, GFP::PCN-1 is bright and reveals the AB and P1 nuclei. It is restricted to the nucleus when an entire nuclear membrane is formed. Nuclear membrane breakdown releases the GFP::PCN-1 in the cytoplasm (Fig. 5b, Supplementary Videos S5 and S6). The nucleus of AB cell was targeted with 10^4 3 MeV protons ($t = 0$ min). We did not observe GFP::PCN-1 foci but, similarly to what was observed in H2B::GFP strain, we noted the formation of chromatin bridges during the first division (Fig. 5b, $t = 10$ min., additional data are shown in Fig. S4). The formation of such chromosomal abnormalities was never observed in non-irradiated nuclei (Fig. 5b, EMS and P2 cells, $n = 9$) or in non-irradiated embryos (Fig. 5b, control, $n = 5$). The cytokinesis induced the chromosomal bridge breakage and the formation of an extra nuclear DNA fragment (suggesting micronucleus formation) excluded from the nucleus. The formation of nuclei around mis-segregated chromosomes and chromosomal fragments apparently contributes to the formation of micronuclei, some of which with very little DNA (Fig. 5b).

The disruption of the cell division synchronization within the 4-cell stage *C. elegans* embryo is shown in Fig. 5b and Supplementary Fig. S1 ($t = 30$ min). In control embryos, the loss of the nuclear localization of GFP::PCN-1 is observed in ABa and ABp cells at $t = 20$ min. In irradiated embryos, the GFP::PCN-1 signal is still present at this time stamp and restricted to the nucleus in these cells. This is also underlined by comparing the time of division between ABa, ABp and EMS, P2. EMS, P2 entered mitosis before ABa and ABp in irradiated embryos. This is never observed in controls. By extending the time-lapse imaging until the 8-cell stage, we could observe that chromosomal bridges appear during the mitotic division of ABa and ABp as well, suggesting the maintenance of a genetic instability (Supplementary Fig. S1).

Discussion

The aim of targeted irradiation is to induce damage localized in specific cellular compartments. Laser micro irradiation is the most commonly used method to achieve this goal mainly because one can use the same microscope to perform irradiation and observation. In addition, the easy access to different wavelengths for irradiation allows the induction of specific cellular damage like SSB, DSB or base lesions with a varying range of doses³⁴. On the contrary, targeted irradiation using a CPM requires the use of distinct equipment for observation and irradiation, thus increasing the number of key parameters to control such as alignment of irradiation beam with the microscope, specific sample preparation, time-lapse imaging and irradiation synchronization. Despite this complexity, CPM offers a unique capability of irradiation dose control, down to a single particle^{22,35}. In addition, with direct access to charged particle beams instead of photons, CPM plays a major role in the study of ionizing radiation in biology. In the present study, we report the possibility to extend this approach to specific cells in a developing multi-cellular organism.

Single cell nuclei can be targeted with a controlled number of charged-particles in living 2-cell stage *C. elegans* embryos and followed-up by time-lapse imaging. We could visualize radiation-induced DNA damage, and undoubtedly DSBs, a few minutes after irradiation in live and intact early *C. elegans* embryos with 10^4 protons (equivalent to 180 Gy in the chromatin). Likewise, HUS-1::GFP radiation-induced foci were also observed in the daughter cells, indicating a persistence of altered DNA through the division cycle in agreement with the absence of active cell cycle checkpoints during DNA damage response in the early *C. elegans* embryo³⁶. The production and maintenance of DNA bridges through the successive cell divisions have been shown in several *C. elegans* strains. We also observed that these DNA bridges alter the cell division timing, inducing a cell cycle asynchrony and modifying the movement of the cells within the irradiated embryos (Fig. 5b and supplementary Fig. S1). Our experimental approach is complementary to the well-established laser micro-irradiation^{34,37} and can complement it by producing more representative damage of ionizing radiation effects. CPM irradiation, commonly used on adherent mammalian cells, can be adapted to target specific cells in a developing multi-cellular organism to address the question of the *in vivo* radiation-induced consequence on a specific cell lineage, the cell-to-cell communication, and the low-dose effect. Data from the voxelized model indicate that the generation of DNA bridges and genomic instability observed experimentally require an energy deposit in the chromatin above 4 pJ (corresponding to a specific energy of about 180 Gy). This could be due to the limited sensitivity of our fluorescent markers or to the lack of specificity for the detection of the radiation-induced damage. But it could also suggest the existence of a dose-threshold below which no sufficient radiation-induced effect would be produced on genomic DNA during the first cell division of AB.

The simulation and mapping of the energy deposited in three dimensional phantoms allows us to correlate the energy deposited in each compartment (chromatin and nucleus) to the radiation-induced damage. First, we clearly observed that no energy deposit is found in the non-targeted nucleus and cell (P1). Second, Monte-Carlo simulations indicate that the biological effects described here (DNA damage foci, DNA bridges and cell cycle delay) appear at rather high specific energies, i.e. 180 Gy in the chromatin of the targeted nucleus (AB). Third,

the energy deposits at various stages of the cell division show a variation of 25% correlated to the variation of the nuclear volume. Fourth, the fraction of energy imparted to the chromatin shows large fluctuations considering various phases of the division, ranging from only 4% in prophase to about 60% in metaphase. Fifth, as the specific energy imparted to the chromatin depends mainly on its condensation state, we verified that only limited variations in terms of energy imparted to the chromatin are expected between samples at the time of irradiation. Indeed, even if the precision in time at which a cell nucleus can be targeted is limited by the visual recognition of specific cell division patterns, a delay in irradiation timing below 2 minutes (chromatin in prophase, Fig. 2b) has no significant influence on the specific energy deposited in the chromatin.

The ability to assess energy deposits and specific energy in various cell compartments relies on the possibility to handle parametrized volumes obtained from fluorescence microscopy in the Geant4 simulation toolkit at the sub-micrometre scale. We believe that new geometrical models developed in the frame of the Geant4-DNA extension, will strengthen biological damage prediction at the DNA molecule scale in cell-based phantoms³⁸, particularly by including the production of DNA single and double strand breaks induced by the direct and indirect effects of oxidative radical species on the cell DNA content³⁹.

Materials and Methods

Worm strains and culture. *C. elegans* worm strains were maintained on nematode growth medium (NGM) agar plates and fed *ad libitum* with *Escherichia coli* strain OP50 at 20 °C, according to standard protocols (Brenner, 1974). We used the following transgenic *C. elegans* strains carrying appropriate fluorescent markers: MG152 (*xisIs3[HisH2B::GFP; rol-6(su1006)]*), WS1433 (*opIs34[hus-1::GFP]*), GZ264 (*isIs17[pGZ265:pie-1::GFP-pcn-1(W0D2.4)]*), SA250 (*tjIs54 [pie-1p::GFP::tbb-2 + pie-1p::2xmCherry::tbg-1 + unc-119(+)]*), *tjIs57 [pie-1p::mCherry::his-48 + unc-119(+)]*. The Caenorhabditis Genetics Centre (CGC, University of Minnesota) provided these *C. elegans* strains and the *E. coli* OP50.

Preparation of large population *C. elegans* embryos. Embryos were isolated from synchronized populations of young gravid hermaphrodites, treated with hypochlorite solution ("bleaching") (Fig. 3a). The bleaching technique was used for synchronizing *C. elegans* cultures at the first larval stage (L1). The principle of the method lies in the fact that worms are sensitive to bleach while the egg shell protects the embryos from it. After treatment with an alkaline hypochlorite solution and rinsing, embryos were maintained on NGM agar plates without food, which allows hatching but prevents further development. Once hatched, the L1 larvae were transferred onto NGM agar plates seeded with OP50 *E. coli* as a food source until the worms reached the adult stage. A second and final bleaching step just before irradiation was performed. These synchronized populations of young gravid hermaphrodites from standard, well-fed culture stocks were collected with M9 buffer (3 g/l KH₂PO₄, 6 g/l Na₂HPO₄, 5 g/l NaCl, 1 mM MgSO₄) and washed three times with sterile water to remove bacteria. Then, worms pelleted *via* centrifugation (2 min., 2000 rpms, room temperature) were treated with a freshly prepared alkaline hypochlorite solution (1.5% (v/v) NaOCl, 1 M NaOH). The suspension was swirled every 2 minutes with vortex-mixing (~6 min.). The released embryos were pelleted *via* centrifugation at 2000 rpms for 2 minutes. Supernatant was carefully discarded and embryos washed three times with M9 buffer followed by centrifugation at 2000 rpms for 2 min. The pelleted embryos were suspended in 50 µL of fresh M9 and an aliquot ~2 µL was directly positioned and used in experimental conditions for micro-irradiation and live imaging using a custom-made support dish described previously by Muggiolu *et al.*³⁵. This sample holder provides a stable long-term environment for microscopic analysis and micro-irradiation experiments. The elapse time between "bleaching" and irradiation was shortened in order to favour the presence of both one-cell and 2-cell stages embryos.

Micro-irradiation. 3 MeV protons (H⁺, LET = 12 keV.µm⁻¹ in liquid water) were accelerated by a 3.5 MV electrostatic accelerator (Singletron, High Voltage Engineering Europa, The Netherlands) present in the AIFIRA facility⁴⁰. In order to target a single cell of a 2-cell stage embryo, the beam was strongly collimated to reduce the particle flux to a few thousand ions per second on target and focused using a triplet of magnetic quadrupoles to achieve a sub-micron resolution under vacuum. After extraction in air, the beam spot size is 1.5 µm. The delivered dose was controlled by counting the particles with a PIN diode installed downstream the sample on the microscope objective wheel. Embryos were irradiated with two doses: 10³ and 10⁴ protons per AB cell nucleus.

Imaging. Embryos were positioned for micro-irradiation and live imaging using a custom-made support dish described by Muggiolu *et al.*³⁵. A drop of 3-µL of M9 medium containing a suspension of freshly extracted embryos was deposited and maintained between two 4-µm thick polypropylene foils (Goodfellow) stretched on a rigid frame made in PEEK (Polyether ether ketone) by means of a clip, thus avoiding the use of any glue. These two foils were slightly stretched to close the dish and maintained the *C. elegans* embryos within a thin layer of M9 which still allowed the traversal of the incoming protons. The M9 medium was kept at +19 °C and the mounted sample kept at 20 °C (+/- 2 °C). All along the experiments, the temperature was monitored and recorded using a thermal probe (PicoLog TC-08). AB nuclei were targeted in their centre based on fluorescence of either GFP tagged HUS-1, histone H2B, or PCN-1. The AB cell was identified due to its larger volume than P1 cell. Embryos were imaged using an inverted fluorescence microscope (AxioObserver Z1, Carl Zeiss Micro-Imaging GmbH) and an x63 objective (LD Plan-Neofluar 63x/0.75) positioned horizontally at the end of the beamline. Images were captured at 10 sec periods using an AxioCamTM CCD camera and directly transferred to a personal computer through a Firewire 400 connection. The irradiation was triggered when the nucleus reached a central position in the AB cell. Time series of micro-irradiated embryos were created using *Image J* software (<http://rsbweb.nih.gov/ij/>). A minimum of five embryos were analysed for each experimental group.

Immunofluorescence staining. Freshly extracted embryo populations were immediately fixed in cold 4% (w/v) paraformaldehyde and their eggshells were freeze-cracked by placing at -20°C during 15 min. Then, embryos were pelleted *via* centrifugation (2 min., 2000 rpm, RT) and paraformaldehyde replaced by cold acetone for permeabilization (2 min., -20°C) and, finally twice washed in M9. After fixation and washing, M9 was removed and replaced by a freshly prepared solution of phalloidin-AF594 (10:1000 (v/v), Molecular Probes) and Hoechst33342 (2:5000 (v/v), Molecular Probes). Embryos were incubated overnight at RT under gentle agitation and then washed *via* two series of centrifugation (2 min. 2000 rpm) with M9. The supernatant was discarded and the pelleted embryos suspended in 2–3 drops of Prolong Gold Antifade reagent (Molecular Probes) and transferred by pipetting for mounting between glass slides using ProLong™ Antifade Gold Reagent (Invitrogen). Three-dimensional images were acquired with a Leica DMRE TCS SP2 AOBS confocal microscope (oil-immersion objective $\times 63$, 1.4 NA), assembled, and reconstructed using *Image J* software.

Monte Carlo simulation. Geant4-DNA^{41–44}, the open source very low energy extension of the Geant4 Monte Carlo simulation toolkit^{45–47}, was used for this work (release Geant4.10.3.p01). We used a physics list based on the recommended “G4EmDNAPhysics_option4” constructor⁴⁴. The Geant4-DNA processes are all step by step processes; as such, they simulate explicitly all the physical interactions of ionizing particles in the irradiated medium and do not use any production cut-off. In the MeV range, the dominant physical processes affecting protons are nuclear scattering, electronic excitation, ionization, and charge exchange. Further details on the physical process classes can be found in the Geant4 documentation (<http://geant4-dna.org/>)⁴⁸.

The primary beam was modelled as mono-energetic 3 MeV proton beam having a $1.5\mu\text{m}$ FWHM Gaussian distribution. The 2-cell stage embryo of *C. elegans* was modelled as a parametrized geometry designated as “phantom” in the following. The phantom was simulated in the form of a voxel arrangement determined from images acquired with a confocal microscope. The methodology for converting confocal image data into a 3D phantom has been described previously in Barberet *et al.*²². The set of images of the 2-cell stage embryos acquired from the confocal microscope was transferred into the public domain ImageJ software (<http://rsbweb.nih.gov/ij/>) for 3D reconstruction (Fig. 1a,b). An intensity threshold was then applied for each colour channel to separate fluorescent objects from the background in each slice of the stack. The nuclear volume was defined as the green channel by manually selecting a ROI around the chromatin on the red channel based on contrast selection, and cropping the region outside the ROI (Fig. 1c). The chromatin, nuclear volume and embryo volume could be extracted into an individual text file containing: (i) the total number of voxels for the 3 channels (Red, Green and Blue), (ii) the voxel size along the 3 dimensions, (iii) a position shift in order to centre the embryo in the simulated irradiation dish, (iv) the list of each voxel's position and material composition, as well as the intensity fluorescence content of the voxel.

The phantom could then be imported directly into the Geant4 simulation using the method described by Incerti *et al.*¹¹. The implemented phantom was formed of multiple identical parallelepiped voxels having the same size, indicated in the form of the confocal images.

The simulations were performed for 10^3 and 10^4 incoming protons to reproduce the experimental conditions.

References

1. Prise, K. M. & Schettino, G. Microbeams in radiation biology: Review and critical comparison. *Radiat. Prot. Dosimetry* **143**, 335–339 (2011).
2. Barberet, P. & Seznec, H. Advances in microbeam technologies and applications to radiation biology. *Radiat. Prot. Dosimetry* **166**, 182–187 (2015).
3. Durante, M. & Friedl, A. A. New challenges in radiobiology research with microbeams. *Radiat. Environ. Biophys.* **50**, 335–338 (2011).
4. Tobias, F. *et al.* Spatiotemporal Dynamics of Early DNA Damage Response Proteins on Complex DNA Lesions. *PLoS One* **8**, e57953 (2013).
5. Walsh, D. W. M. *et al.* Live cell imaging of mitochondria following targeted irradiation *in situ* reveals rapid and highly localized loss of membrane potential. *Sci. Rep.* **7**, 46684 (2017).
6. Sedelnikova, O. A. *et al.* DNA Double-Strand Breaks Form in Bystander Cells after Microbeam Irradiation of Three-dimensional Human Tissue Models. *Cancer Res.* **67**, 4295–4303 (2007).
7. Belyakov, O. V. *et al.* Biological effects in unirradiated human tissue induced by radiation damage up to 1 mm away. *PNAS* **102**, 14203–14208 (2005).
8. Zlobinskaya, O., Girst, S., Greubel, C. & Hable, V. Reduced side effects by proton microchannel radiotherapy: study in a human skin model. Reduced side effects by proton microchannel radiotherapy: study in a human skin model. *Radiat. Environ. Biophys.* **52**, 123–133 (2013).
9. Miller, J. H., Chrisler, W. B., Wang, X. & Sowa, M. B. Confocal microscopy for modeling electron microbeam irradiation of skin. *Radiat. Environ. Biophys.* **50**, 365–369 (2011).
10. Merz, F. *et al.* Tissue slice cultures from humans or rodents: a new tool to evaluate biological effects of heavy ions. *Radiat. Environ. Biophys.* **49**, 457–462 (2010).
11. Choi, W. V. Y. *et al.* Adaptive Response in Zebrafish Embryos Induced Using Microbeam Protons as Priming Dose and X-ray Photons as Challenging Dose. *J. Radiat. Res.* **51**, 657–664 (2010).
12. Choi, W. V. Y. *et al.* Triphasic Low-dose Response in Zebrafish Embryos Irradiated by Microbeam Protons. *J. Radiat. Res.* **53**, 475–481 (2012).
13. Fukamoto, K. *et al.* Development of the Irradiation Method for the First Instar Silkworm Larvae Using Locally Targeted Heavy-ion Microbeam. *J. Radiat. Res.* **48**, 247–253 (2007).
14. Sugimoto, T. *et al.* Cell cycle arrest and apoptosis in *Caenorhabditis elegans* germline cells following heavy-ion microbeam irradiation. *Int. J. Radiat. Biol.* **82**, 31–38 (2006).
15. Bertucci, A., Pocock, R. D., Randers-Pehrson, G. & Brenner, D. J. Microbeam irradiation of the *C. elegans* nematode. *J. Radiat. Res.* **50**, A49–A54 (2009).
16. Deng, X. *et al.* Ceramide biogenesis is required for radiation-induced apoptosis in the germ line of *C. elegans*. *Science* (80-.). **322**, 110–115 (2008).
17. Sendoel, A., Kohler, I., Fellmann, C., Lowe, S. W. & Hengartner, M. O. HIF-1 antagonizes p53-mediated apoptosis through a secreted neuronal tyrosinase. *Nature* **465**, 577–583 (2010).

18. Adenle, A. A., Johnsen, B. & Szewczyk, N. J. Review of the results from the International C. elegans first experiment (ICE-FIRST). *Adv. Sp. Res.* **44**, 210–216 (2009).
19. Buonanno, M. et al. Microbeam irradiation of C. elegans nematode in microfluidic channels. *Radiat. Environ. Biophys.* **52**, 531–537 (2013).
20. Guo, X. et al. Radiation-Induced Bystander Signaling from Somatic Cells to Germ Cells in *Caenorhabditis elegans*. *Radiat. Res.* **180**, 268–275 (2013).
21. Li, Q. et al. Spatial function of the oxidative DNA damage response in radiation induced bystander effects in intra- and inter-system of *Caenorhabditis elegans*. *Oncotarget* **8**, 51253–51263 (2017).
22. Barberet, P. et al. Cell micro-irradiation with MeV protons counted by an ultra-thin diamond membrane. *Appl. Phys. Lett.* **111**, 243701 (2017).
23. ICRU Report 60. *Fundamental Quantities and Units of Ionizing Radiation (International Commission on Radiation Units and Measurements, Bethesda, MD)*. (1998).
24. Barberet, P. et al. Monte-Carlo dosimetry on a realistic cell monolayer geometry exposed to alpha particles. *Phys. Med. Biol.* **57**, 2189–2207 (2012).
25. Edgar, L. G. & McGhee, J. D. DNA synthesis and the control of embryonic gene expression in *C. elegans*. *Cell Press* **53**, 589–599 (1988).
26. Begasse, M. L. & Hyman, A. A. The First Cell Cycle of the *Caenorhabditis elegans* Embryo: Spatial and Temporal Control of an Asymmetric Cell Division. *Cell Cycle Dev. Results Probl. Cell Differ.* **53**, 109–133 (2011).
27. Gartner, A. et al. A Conserved Checkpoint Pathway Mediates DNA Damage – Induced Apoptosis and Cell Cycle Arrest in *C. elegans* State University of New York at Stony Brook. *Mol. Cell* **5**, 435–443 (2000).
28. Hofmann, E. R. et al. *Caenorhabditis elegans* HUS-1 is a DNA damage checkpoint protein required for genome stability and EGL-1-mediated apoptosis. *Curr. Biol.* **12**, 1908–1918 (2002).
29. Fazell, G., Stetter, M., Lisack, J. N. & Wehman, A. M. C. elegans Blastomeres Clear the Corpse of the Second Polar Body by LC3-Associated Phagocytosis. *Cell Press* **23**, 2070–2082 (2018).
30. Brauchle, M., Baumer, K. & Gonczy, P. Differential Activation of the DNA Replication Checkpoint Contributes to Asynchrony of Cell Division in *C. elegans* Embryos Michael. *Curr. Biol.* **28**, 819–827 (2003).
31. Waga, S. & Stillman, B. The DNA Replication Fork in Eukaryotic Cells. *Annu. Rev. Biochem.* **67**, 721–751 (1998).
32. Essers, M. A. G. et al. Functional interaction between β -catenin and FOXO in oxidative stress signaling. *Science* (80-). **308**, 1181–1184 (2005).
33. Meister, P., Taddet, A., Ponti, A., Baldacci, G. & Gasser, S. M. Replication foci dynamics: Replication patterns are modulated by S-phase checkpoint kinases in fission yeast. *EMBO J.* **26**, 1315–1326 (2007).
34. Koury, E., Harrell, K. & Smolkova, S. Differential RPA-1 and RAD-51 recruitment *in vivo* throughout the *C. elegans* germline, as revealed by laser microirradiation. *Nucleic Acids Res.* **46**, 748–764 (2018).
35. Mugglolu, G. et al. Single α -particle irradiation permits real-time visualization of RNF8 accumulation at DNA damaged sites. *Sci. Rep.* **7**, 41764 (2017).
36. Holway, A. H., Kim, S. H., La Volpe, A. & Michael, W. M. Checkpoint silencing during the DNA damage response in *Caenorhabditis elegans* embryos. *J. Cell Biol.* **172**, 999–1008 (2006).
37. Sulston, J. E. & White, J. G. Regulation and cell autonomy during postembryonic development of *Caenorhabditis elegans*. *Dev. Biol.* **78**, 577–597 (1980).
38. Lampe, N. et al. Mechanistic DNA damage simulations in Geant4-DNA part 1: A parameter study in a simplified geometry. *Phys. Medica* **48**, 135–145 (2018).
39. Lampe, N. et al. Mechanistic DNA damage simulations in Geant4-DNA Part 2: Electron and proton damage in a bacterial cell. *Phys. Medica* **48**, 146–155 (2018).
40. Sorieul, S., Alfaut, P., Daudin, L., Serani, L. & Moretto, P. Aifira: An ion beam facility for multidisciplinary research. *Nucl. Instruments Methods Phys. Res. B* **332**, 68–73 (2014).
41. Incerti, S. et al. The Geant4-Dna Project. *Int. J. Model. Simulation, Sci. Comput.* **1**, 157–178 (2010).
42. Incerti, S. et al. Comparison of GEANT4 very low energy cross section models with experimental data in water. *Med. Phys.* **37**, 4692–4708 (2010).
43. Bernal, M. A. et al. Track structure modelling in liquid water: A review of the Geant4-DNA very low energy extension of the Geant4 Monte Carlo simulation toolkit. *Phys. Med.* **31**, 861–74 (2015).
44. Incerti, S. et al. Geant4-DNA example applications for track structure simulations in liquid water: A report from the Geant4-DNA Project. *Med. Phys.* **45**, e722–e739 (2018).
45. Agostinelli, S. et al. GEANT4 - A simulation toolkit. *Nucl. Instruments Methods Phys. Res. Sect. A Accel. Spectrometers, Detect. Assoc. Equip.* **506**, 250–303 (2003).
46. Allison, J. et al. Geant4 Developments and Applications. *IEEE Trans. Nucl. Sci.* **53**, 270–278 (2006).
47. Allison, J. et al. Recent developments in GEANT4. *Nucl. Instruments Methods Phys. Res. Sect. A Accel. Spectrometers, Detect. Assoc. Equip.* **835**, 186–225 (2016).
48. Incerti, S. et al. Monte Carlo dosimetry for targeted irradiation of individual cells using a microbeam facility. *Radiat. Prot. Dosimetry* **133**, 2–11 (2009).

Acknowledgements

The AIFIRA facility is financially supported by the CNRS, the university of Bordeaux and the Région Nouvelle Aquitaine. We thank the technical staff members of the AIFIRA facility P. Alfaut and S. Sorieul. MS was supported by the Region Aquitaine (POPRA). This work has been partly supported by the European Community as an Integrating Activity “Support of Public and Industrial Research Using Ion Beam Technology” (SPIRIT) under the EC contract no. 227012. GM was supported by the European Community as an “Integrating Activity Supporting Postgraduate Research with Internships in Industry and Training Excellence” (SPRITE) under EC contract no. 317169. The project was supported by the French national Centre for Scientific Research (CNRS, Mission Interdisciplinaire NEEDS). *C. elegans* strains were provided by the *Caenorhabditis* Genetics Center (CGC), which is funded by NIH Office of Research Infrastructure Programs (P40 OD010440). The authors would like to thank Denis Dupuy for the constructive criticism and comments of the manuscript, and Jean-Jacques Bernaulte for the careful proofreading of the manuscript.

Author Contributions

P.B., M.S., G.M., G.D., F.V., S.B. and H.S. designed and performed the radiation biology experiments; E.T., P.B. and S.I. performed Monte Carlo simulations; H.S. conceived and supervised this project; E.T., P.B. and H.S. contributed to the data analysis and interpreted the results; E.T., P.B. and H.S. wrote the paper; all authors reviewed the manuscript.

Additional Information

Supplementary information accompanies this paper at <https://doi.org/10.1038/s41598-019-47122-7>.

Competing Interests: The authors declare no competing interests.

Publisher's note: Springer Nature remains neutral with regard to jurisdictional claims in published maps and institutional affiliations.



Open Access This article is licensed under a Creative Commons Attribution 4.0 International License, which permits use, sharing, adaptation, distribution and reproduction in any medium or format, as long as you give appropriate credit to the original author(s) and the source, provide a link to the Creative Commons license, and indicate if changes were made. The images or other third party material in this article are included in the article's Creative Commons license, unless indicated otherwise in a credit line to the material. If material is not included in the article's Creative Commons license and your intended use is not permitted by statutory regulation or exceeds the permitted use, you will need to obtain permission directly from the copyright holder. To view a copy of this license, visit <http://creativecommons.org/licenses/by/4.0/>.

© The Author(s) 2019

Conclusions And Perspectives

The work presented here is focused on charged-particle micro-irradiations of biological samples and more specifically on microdosimetry questions related to this experimental approach. Charged-particles in the MeV energy range have high LETs and induce highly complex molecular lesions when depositing their energy in living matter. They are present in natural radiation background (from telluric or cosmic origins) and more and more used in radiation therapy. From the experimental point of view, charged-particles present unique features to generate localized molecular lesions in living cells and study molecular and biological consequences of clustered lesions. When propagating in matter, charged-particles deposit their energy along almost linear tracks that can be modeled in great details by Monte Carlo track structure codes. This constitute one of the main strengths of their use compared to more common micro-irradiation techniques based on lasers or UV microspots.

By designing dedicated beam lines (CPM), charged-particles can be easily focused to micrometer spots and steered precisely to target specific cell compartments and study online the early cell response.

Prior to my PhD, the iRiBio group at CENBG developed experimental techniques and methodologies to micro-irradiate reproducibly biological cells with counted protons and α -particles using the CPM at the AIFIRA facility. These developments have started to be applied in the last years to the experimental measurement of biological effects from cellular to multicellular organisms.

My thesis work aimed at developing microdosimetric models of the micro-irradiations performed at AIFIRA. This was achieved by measuring physical characteristics of the CPM using novel high-resolution track detectors and by simulating the interaction of protons and α -particles in micro-focused spots from the initial EDs to the prediction of DNA damage using the open source track structure toolkit Geant4-DNA.

The first part of this work focused on the development of a methodology to use FNTDs for quality control of the CPM at the AIFIRA facility. Compared to the commonly used CR39 nuclear track detector, FNTDs do not require chemical treatment for the read-out and offer interesting features such as a high spatial resolution, wide dynamic range of ED measurements and three-dimensional track information. Single tracks of MeV protons and α -particles are unambiguously detected, and the size of the fluorescent spot is below one micrometer. When irradiating with several traversals in a micrometric beam spot, the fluorescence intensity increases linearly with the dose before saturating above about 20 particles/spot. Unfortunately, the single-track diameter could not be correlated to the LET of

the particles used in this work. Nevertheless, FNTDs will be used in routine in the future to insure quality check in single particle irradiation experiments.

Then, the AIFIRA microbeam was used to investigate repair processes activated by micro-irradiating cells with increasing numbers of protons ($\text{LET} = 12 \text{ keV} \cdot \mu\text{m}^{-1}$) or α -particles ($\text{LET} = 148 \text{ keV} \cdot \mu\text{m}^{-1}$). The kinetics of accumulation at damaged sites of the GFP-RNF8 and GFP-XRCC1 proteins were measured. The early response of these proteins (seconds to minutes) provide interesting insights in the relation between the initial physical lesions and the DNA repair pathways. I contributed to the microdosimetric calculations of the EDs and the induced direct DNA damage. The calculated DNA damage types and complexity dependency with particle LETs show a good agreement with other studies. The results indicate a coherence between the protein function, the EDs distribution and its clustering into different types of DNA damage. However, the full interpretation of the biological results will require to overcome a few limitations related to the microdosimetric calculations. It is in particular the case for the clustering of the DNA lesions. The clustering at nanometer scale was calculated only for direct effects in a homogeneous water cube. This could be improved by considering the DNA geometries in human cells to allow the calculation of DNA damage from direct and indirect effects. A Geant4-DNA example allowing these calculations should be available soon. From the experimental point of view, the link between the protein kinetics and the amount of induced DNA lesions could as well be described by theoretical modeling of the protein behavior after charged-particle micro-irradiations and its diffusion to damage sites. These damaged sites can be modeled as protein trapping sites with a fixation probability depending on the amount of DNA lesions assessed by Monte Carlo simulations.

Finally, a methodology to reproducibly micro-irradiate a living organism, *C. elegans*, at a specific stage and to observe in real time the radiation-induced effects at the AIFIRA facility was validated before the beginning of the present work. This simple stage of *C. elegans* life cycle with 2 cells allowed following more easily the irradiated cell in the first cell divisions after irradiation. This approach opens perspectives for selective irradiation at lower doses (down to one particle / cell) of specific cells in an organism in development. Nevertheless, studying dose-effect relationship with such irradiation raises the question of the dose. Indeed, this type of sample has a geometry significantly different from adherent cells and its rapid development involves variation of the cell's geometry and chromatin condensation within times scales comparable to the time required for irradiation. Monte Carlo simulation in 3D realistic phantoms of *C.elegans* was required in the case of the 2-cell stage embryos to characterize the EDs. In the future, this methodology can be extended to other stages of

development and much lower doses opening a complete radiobiology framework including a precise and reproducible radiation targeting, advanced Monte Carlo based and open source microdosimetry methods and an appropriate model to study the biological response from the early response to trans-generational effects.

Micro-dosimétrie d'irradiations par microfaisceau d'ions par méthodes Monte-Carlo

L'interaction des particules chargées avec la matière conduit à un dépôt d'énergie très localisé dans des traces de dimensions sub-micrométriques. Cette propriété unique rend ce type de rayonnement ionisant particulièrement intéressant pour disséquer les mécanismes moléculaires radio-induits suite à l'échelle de la cellule. L'utilisation de microfaisceaux de particules chargées offre en outre la capacité d'irradier sélectivement à l'échelle du micromètre avec une dose contrôlée jusqu'à la particule unique. Mon travail a porté sur des irradiations réalisées avec le microfaisceau de particules chargées de la plateforme AIFIRA (Applications Interdisciplinaires des Faisceaux d'Ions en Région Aquitaine) du CENBG. Ce microfaisceau délivre des protons et particules α et est dédié aux irradiations ciblées *in vitro* (cellules humaines) et *in vivo* (*C. elegans*).

En complément de l'intérêt qu'elles présentent pour des études expérimentales, les dépôts d'énergie et les interactions des particules chargées avec la matière peuvent être modélisés précisément tout au long de leur trajectoire en utilisant des codes de structures de traces basés sur des méthodes Monte-Carlo. Ces outils de simulation permettent une caractérisation précise de la micro-dosimétrie des irradiations allant de la description détaillée des interactions physiques à l'échelle nanométrique jusqu'à la prédiction du nombre de dommages à l'ADN et leurs distributions dans l'espace.

Au cours de ma thèse, j'ai développée des modèles micro-dosimétriques basés sur l'outil de modélisation Geant4-DNA dans deux cas. Le premier concerne la simulation de la distribution d'énergie déposée dans un noyau cellulaire et le calcul du nombre des différents types de dommages ADN (simple et double brin) aux échelles nanométrique et micrométrique, pour différents types et nombres de particules délivrées. Ces résultats sont confrontés à la mesure expérimentale de la cinétique de protéines de réparation de l'ADN marquées par GFP (Green Fluorescent Protein) dans des cellules humaines. Le second concerne la dosimétrie de l'irradiation d'un organisme multicellulaire dans le cadre d'études de l'instabilité génétique dans un organisme vivant au cours du développement (*C. elegans*). J'ai simulé la distribution de l'énergie déposée dans différents compartiments d'un modèle réaliste en 3D d'un embryon de *C. elegans* suite à des irradiations par protons. Enfin, et en parallèle de ces deux études, j'ai développé un protocole pour caractériser le microfaisceau d'AIFIRA à l'aide de détecteurs de traces fluorescent (FNTD) pour des irradiations par protons et par particules α . Ce type de détecteur permet en effet de visualiser les trajectoires des particules incidentes avec une résolution de l'ordre de 200 nm et d'examiner la qualité des irradiations cellulaires réalisées par le microfaisceau.

Mots-clés : Microfaisceau d'ions, micro-irradiation ciblée, Monte-Carlo, Geant4-DNA, microdosimétrie, radiobiologie.

Monte Carlo microdosimetry of charged-particle microbeam irradiations

The interaction of charged-particles with matter leads to a localized energy deposits in sub-micrometric tracks. This unique property makes this type of ionizing radiation particularly interesting for deciphering the radiation-induced molecular mechanisms at the cell scale. Charged-particle microbeams (CPMs) provide the ability to target a given cell compartment at the micrometer scale with a controlled dose down to single particle. My work focused on irradiations carried out with the CPM at the AIFIRA facility in the CENBG (*Applications Interdisciplinaires des Faisceaux d'Ions en Région Aquitaine*). This microbeam delivers protons and α -particles and is dedicated to targeted irradiation *in vitro* (human cells) and *in vivo* (*C. elegans*).

In addition to their interest for experimental studies, the energy deposits and the interactions of charged-particles with matter can be modeled precisely along their trajectory using track structure codes based on Monte Carlo methods. These simulation tools allow a precise characterization of the micro-dosimetry of the irradiations from the detailed description of the physical interactions at the nanoscale to the prediction of the number of DNA damage, their complexity and their distribution in space.

During my thesis, I developed micro-dosimetry models based on the Geant4-DNA modeling toolkit in two cases. The first concerns the simulation of the energy distribution deposited in a cell nucleus and the calculation of the number of different types of DNA damage (single and double strand breaks) at the nanometric and micrometric scales, for different types and numbers of delivered particles. These simulations are compared with experimental measurements of the kinetics of GFP-labeled (Green Fluorescent Protein) DNA repair proteins in human cells. The second is the dosimetry of irradiation of a multicellular organism to study the genetic instability in a living organism during development (*C. elegans*). I simulated the distribution of the energy deposited in different compartments of a realistic 3D model of a *C. elegans* embryo following proton irradiations. Finally, and in parallel with these two studies, I developed a protocol to characterize the AIFIRA microbeam using fluorescent nuclear track detector (FNTD) for proton and α -particle irradiations. This type of detector makes it possible to visualize in 3D the incident particle tracks with a resolution of about 200 nm and to examine the quality of the cellular irradiations carried out by the CPM.

Keywords: Charged-particle microbeam, targeted irradiation, Monte Carlo, Geant4-DNA, microdosimetry, radiobiology.

Centre d'Etudes Nucléaires de Bordeaux-Gradignan
UMR 5797, 19 Rue du Solarium, 33170 Gradignan